LBL-34171
UC-400, UC-406

Lawrence Berkeley Laboratory
UNIVERSITY OF CALIFORNIA

Materials Sciences Division

Infrared Detection with High-T_c Bolometers and Response of Nb Tunnel Junctions to Picosecond Voltage Pulses

S. Verghese
(Ph.D. Thesis)

May 1993

Prepared for the U.S. Department of Energy under Contract Number DE-AC03-76SF00098

DISCLAIMER

LBL-34171

Infrared Detection with High-T_c Bolometers and Response of Nb Tunnel Junctions to Picosecond Voltage Pulses

by

Simon Verghese

B.S. (North Carolina State University) 1986
M.S. (North Carolina State University) 1987
M.A. (University of California at Berkeley) 1992

A dissertation submitted in partial satisfaction of the

requirements for the degree of

Doctor of Philosopy

in

Physics

in the

GRADUATE DIVISION

of the

UNIVERSITY of CALIFORNIA at BERKELEY

Committee in charge:

Professor P. L. Richards, Chair
Professor J. Clarke
Professor T. Van Duzer

This work was supported in part by the Director, Office of Energy Research, Office of Basic Energy Sciences, Materials Sciences Division, of the U. S. Department of Energy under Contract No. DE-AC03-76SF00098.

May 1993

Infrared Detection with High-T_c Bolometers and
Response of Nb Tunnel Junctions to Picosecond Voltage Pulses

Abstract

Infrared Detection with High-T_c Bolometers and
Response of Nb Tunnel Junctions to Picosecond Voltage Pulses

by

Simon Verghese

Doctor of Philosophy in Physics

University of California at Berkeley

Professor P. L. Richards, Chair

Oxide superconductors with high critical temperature T_c make sensitive thermometers for several types of infrared bolometers. We built composite bolometers with $YBa_2Cu_3O_{7-\delta}$ thermometers on sapphire substrates which have higher sensitivity than competing thermal detectors which operate at temperatures above 77 K. A 1×1 mm bolometer with gold black serving as the radiation absorber has useful sensitivity for wavelengths $20 - 100\,\mu$m. A 3×3 mm bolometer with a bismuth film as the absorber operates from $20 - 100\,\mu$m. High-T_c bolometers which are fabricated with micromachining techniques on membranes of Si or Si_3N_4 have potential application to large-format arrays which are used for infrared imaging. Thermal isolation is achieved by suspending the membrane on two thin legs of the membrane material. A nonisothermal high-T_c bolometer can be fabricated on a membrane of yttria-stabilized zirconia (YSZ) which is in thermal contact with the heat sink along the perimeter of the membrane. A thermal analysis indicates that the YSZ membrane bolometer can have improved sensitivity compared to the sapphire bolometer for spectrometer applications.

The quasiparticle tunneling current in a superconductor-insulator-superconductor (SIS) junction is highly nonlinear in the applied voltage. If an SIS junction is excited with photons of energy $\hbar\omega$, where $\hbar\omega/e$ is larger than the width of the nonlinearity in the I-V curve, the response of the quasiparticle current is retarded and depends strongly on ω. We have made the first measurement of the linear response of the quasiparticle current in a $Nb/AlO_x/Nb$ junction over a broad bandwidth from $75 - 200$ GHz. We used picosecond pulses of millimeter wave radiation which were generated by illuminating a photoconductive switch with a mode-locked laser. The data are in agreement with the theory of linear photon-assisted tunneling. Nonlinear measurements made with these pulses may provide information about the quasiparticle lifetime. Preliminary data from such measurements are presented.

Paul L. Richards

Contents

List of Figures

List of Tables

Acknowledgements

Thirty-one people deserve special mention for making it possible for me to write this dissertation. First, I would like to thank my parents for conceiving it all from the start. They have always been, and continue to be, my role models. My advisor, Professor Paul Richards, taught me by example how to be a professional member of the research community. I hope he has not aged far beyond the six years he was stuck providing me with that example. Also, I owe thanks to Professor Joseph Orenstein for teaching me nonlinear optics and swing mechanics.

An honorable mention goes to the condensed-matter side of the Richards group. Tom Kenny ultimately recruited me to the group to play for the Polyps. Carl Mears always seemed to be around when I had a new idea. Much of the physics I learned at Berkeley came from discussions with Carl and Qing Hu. Mike Nahum taught me how to play the stock market, and everyday I could count on John Birmingham to eat Thai food for lunch. David Miller pointed out that life is what happens while you plan for the future. More importantly, Warren Holmes gave me his helium transfer tube for life.

Thanks to nineteen members of the U. C. Berkeley Men's Ultimate Frisbee Team for taking me to Nationals in 1992—"Maybe to improve our luck, we should try to be a duck." And thirty-first, I thank Lise Lindquist for sharing her life with me and for being my dear. I write these words on the third in a long series of future anniversaries of our first date on Mt. Shasta.

Chapter 1

Theory of Superconducting Bolometers

1.1 Introduction

Bolometers are transducers that respond to heating produced by absorbing radiation. Bolometric detectors have three essential parts: a radiation absorbing surface, a thermometer, and a weak thermal link to a heat sink. Bolometers with a wide range of sensitivities are used from visible light wavelengths to microwaves for sensitive direct detection and for absolute power measurements. Variations on the liquid helium cooled germanium bolometer developed by Low[1] have been the most widely used broadband detectors for slowly varying signals at infrared wavelengths where well developed photoconductors are not available. Other bolometric detectors are used to detect phonons, and X-rays, and to search for unknown particles that are candidates for the dark matter in the universe.

Superconducting bolometers have long been considered for applications to sensitive infrared detection. Here, the thermometer exploits the sharp change in the resistance of a superconducting thin film at its critical temperature T_c. Although excellent performance has been achieved[2] with conventional superconductors, these bolometers are more complicated than bolometers with comparable performance which use doped semiconductor thermometers[1, 3]. Consequently, they have rarely been used in practical applications.

The discovery of high-T_c superconductors raised the question of whether there are practical applications for superconducting bolometers operating in the $\sim$ 100 K tempera-

ture range. For wavelengths $\lambda < 20\,\mu$m, liquid nitrogen (LN) cooled photovoltaic detectors such as HgCdTe are widely used. For longer wavelengths, however, there is no satisfactory cooled detector technology above liquid helium (LHe) temperatures. Room temperature thermal detectors such as the thermopile, the pyroelectric detector, or the Golay cell are used in applications where a LN-cooled high-T_c bolometer could be conveniently used. The high-T_c bolometer offers higher sensitivity under these conditions, primarily because of the sensitivity with which small changes in the temperature of the bolometer can be detected. Applications for composite high-T_c bolometers exist in far infrared laboratory spectroscopy[4] and space observations of bright sources such as planets[5] using radiatively cooled systems. Applications as large format infrared imagers may also exist[6].

1.2 Response to an optical signal

The response of a bolometer to an optical signal is best understood by example. Figure 1.1 is a schematic diagram of an infrared bolometer coupled to an imaging optical system. An f/3 lens couples the infrared light to the radiation absorber on the bolometer. The on-axis rays couple to the center of the absorber with a solid angle $\Omega = 0.09\,$sr. The area of the main lobe of the diffraction pattern associated with the lens is approximately λ^2/Ω, where λ is the wavelength. For a bolometer with area $A > \lambda^2/\Omega$, off-axis rays can be absorbed in another diffraction spot. The number of spatial modes of light coupling to the bolometer is $N = A\Omega/\lambda^2$. The electromagnetic fields in these modes are spatially incoherent with each other and cannot interfere. In the Rayleigh-Jeans limit, the maximum power from a blackbody source of temperature T_b that can be absorbed by the bolometer is $P = 2NkT_bB_1$, where k is Boltzman's constant and B_1 is the spectral bandwidth. Consequently, bolometers designed for submillimeter wavelengths must have larger areas than infrared bolometers to retain the same signal strength from a blackbody source.

Consider the bolometer of Fig. 1.1 with heat capacity C at temperature T connected to a heat sink via a thermal conductance G. The thermal time constant is $\tau = C/G$. The radiation absorber absorbs a fraction $\epsilon \leq 1$ of the incident signal power P, and the resulting increase in temperature is detected by a thermometer with a temperature-dependent resistance $R(T)$ which is attached to the substrate. The thermometer is biased with a constant current I that generates a voltage V across it. If the signal power is chopped at a frequency $\omega/2\pi$, a component of the voltage V oscillates at $\omega/2\pi$ with an amplitude

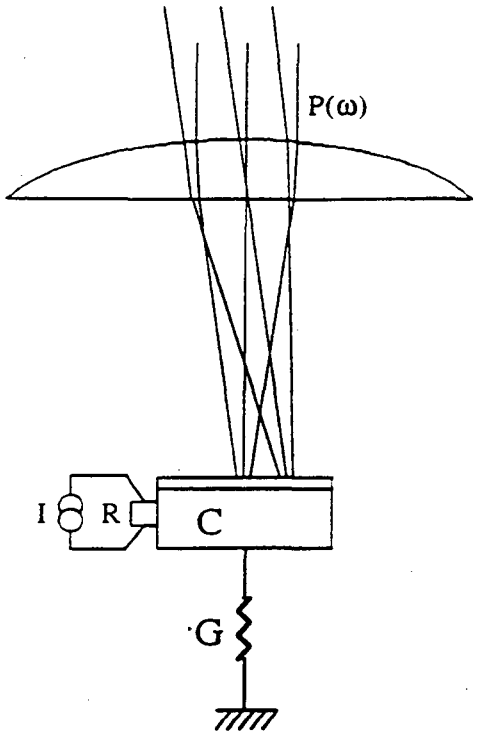

Figure 1.1: Schematic diagram of an infrared bolometer.

proportional to P. The responsivity $S(\omega)$ is given by[7]

$$S(\omega) = \epsilon I \frac{dR(T)}{dT} |G_{eff} + i\omega C|^{-1} \ , \tag{1.1}$$

where the effective thermal conductance is $G_{eff} = G - I^2 dR(T)/dT$. To avoid thermal instability of the bolometer, we require $G_{eff} > 0$. For superconductor thermistors with $dR(T)/dT > 0$, the bias current must satisfy the condition $I^2 dR(T)/dT = aG$, where $a < 1$.

Generally, the responsivity need only be large enough such that the electrical signal generated across the thermometer can be read out with an adequate ratio of signal to noise by the preamplifier. A complete characterization of an infrared detector requires both values of responsivity and of noise equivalent power.

1.3 Noise Equivalent Power

The electrical noise equivalent power (NEP) is the power which must be dissipated in a bolometer to produce a signal equal to the rms noise in a 1 Hz noise bandwidth. The

optical NEP—the optical power incident on the bolometer area required to produce a signal equal to the rms noise—is given by the electrical NEP divided by the optical efficiency factor ϵ. The electrical NEP (per unit post-detection bandwidth) can be written as the sum of squares of statistically uncorrelated terms which arise from a number of sources[7]

$$\mathrm{NEP} = \left(4kT_c^2 G + \frac{4kT_c R}{|S|^2} + \frac{e_n^2 + (i_n R)^2}{|S|^2} + \frac{S_v(\omega)}{|S|^2} + \mathrm{NEP}^2{}_{\mathrm{photon}} \right)^{1/2} . \qquad (1.2)$$

The first term arises from the random exchange of energy between the bolometer and the heat sink via the thermal conductance. It is approximated from the conventional expressions from equilibrium thermodynamics[8]. The second term is the contribution of Johnson noise in the thermometer. The third term is the contribution of the preamplifier noise where e_n and i_n are the equivalent voltage noise and current noise sources referred to the input of the preamplifier. The fourth term is the contribution from excess noise in the thermometer where $S_v(\omega)$ is the spectral density of voltage fluctuations. This noise is extremely sensistive to the microscopic details of the thermometer material and is usually measured experimentally. The last term is the contribution from power fluctuations on the incident optical signal. These fluctuations depend on the source of the light and its spectral bandwidth (pre-detection bandwidth) and on the time over which the signal at the output of the bolometer is integrated (the post-detection time). The next section discusses this term.

Figure 1.2 shows fundamental limits to the NEP of an ideal bolometer operating at 87 K with a 77 K heat sink calculated from (1.2). We assume an ideal bolometer has negligible heat capacity and a noiseless thermometer and electronic readout. The thermal conductance G is only large enough to prevent infrared loading from the signal from heating the bolometer above 87 K. The detector is assumed to view 300 K background radiation with a throughput $A\Omega = 10^{-2}\,\mathrm{sr\,cm^2}$ and perfect optical efficiency.

We can optimize the NEP of a bolometer with a resistive thermometer by neglecting the photon noise—which, for a high-T_c bolometer, is always smaller than the thermal fluctuation noise—and also by neglecting the excess thermometer noise $S_v(\omega)$. The optimal operating point can then be found by equating the phonon noise and Johnson noise terms in (1.2). We find $\omega^2\tau^2 = aR^{-1}(dR/dT)T - 1$, a result involving neither G nor R that fixes $\omega\tau$ for given values of a, $R^{-1}dR/dT$, and T.

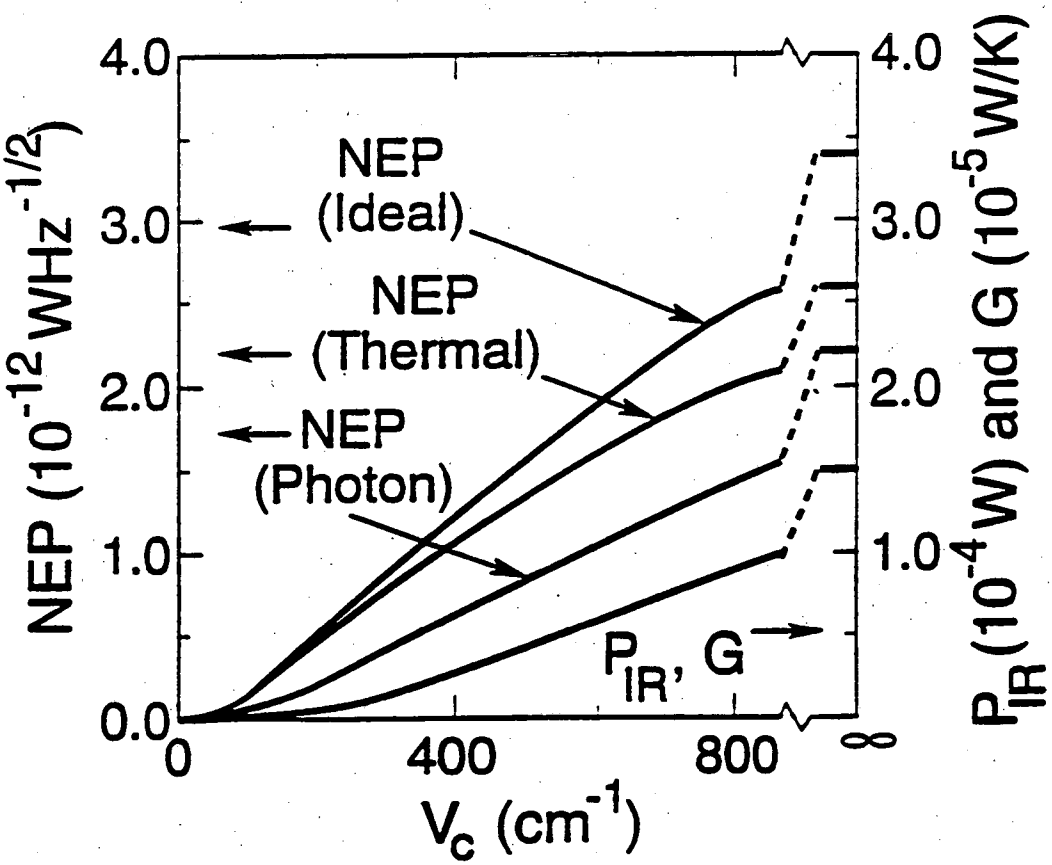

Figure 1.2: Infrared power loading P_{IR} and thermal conductance G for an ideal thermal infrared detector plotted as a function of the cutoff frequency ν_c of the cold low-pass filter. The detector is assumed to view 300 K background radiation with a throughput $A\Omega = 10^{-2}\,\mathrm{sr\,cm^2}$ and perfect optical efficiency and to operate 10 K above the heat sink temperature. The NEP of the ideal detector is shown along with the separate contributions from thermal fluctuation noise and photon noise.

1.4 Photon noise

The photon noise contribution to the NEP can be important for low-background bolometers operating at LHe temperatures. Semi-classical treatments of the theory of photon fluctuation noise have routinely been used in calculating ultimate sensitivity limits of LHe-cooled bolometeric receivers viewing blackbody radiation sources. The semi-classical treatment is only valid when used to calculate the rms fluctuations on the incident photon flux in a single spatial mode and at a single frequency. Many workers have erroneously extended this treatment to multimode, broad bandwidth receivers. This section discusses the relationship between photon fluctuations and $\mathrm{NEP}_{\mathrm{photon}}$ and gives a closed-form expression for calculating $\mathrm{NEP}_{\mathrm{photon}}$ in the limit of many spatial modes and broad spectral bandwidth. The Dicke radiometer and the contribution of detector noise to the measurement of photon noise are also discussed.

1.4.1 Single spatial mode, single frequency

Consider a cavity at an equilibrium temperature T_b with low emissivity walls which are much thinner than a wavelength $\lambda = c/\nu$. The interior surface of the cavity is then painted with a black absorber which is in thermal contact with the cavity wall. Assume the cavity volume is much greater than λ^3 and that a small hole of area $A = \lambda^2/\pi$ is bored in the cavity wall and covered with a polarizer. A bolometer with unity absorption efficiency would measure the power escaping through the hole for a unit bandwidth as

$$P = \overline{n} h\nu \,, \tag{1.3}$$

where $\overline{n} \equiv \langle n \rangle_b = [\exp(h\nu/kT_b) - 1]^{-1}$ is the mean number of photons per second per hertz escaping through the hole [10]. The rms fluctuations in n are

$$\langle \Delta n^2 \rangle_b = \langle n^2 \rangle_b - \langle n \rangle_b^2 = \overline{n}^2 + \overline{n} \,. \tag{1.4}$$

Since the audio bandwidth associated with a 1 sec unweighted average of the bolometer output is 1/2 Hz, the mean square noise power in a unit post-detection bandwidth and in a unit spectral bandwidth is

$$\mathrm{NEP}^2_{\mathrm{photon}} = 2(\overline{n}^2 + \overline{n})(h\nu)^2 \,. \tag{1.5}$$

The two terms in (1.5) associated with $\overline{n}^2$ and $\overline{n}$ are often called the classical wave noise and the photon shot noise respectively.

1.4.2 Multiple spatial modes, multiple frequencies

Now consider the same cavity with an enlarged hole $A = N\lambda^2/\pi$, $N > 1$, no polarizer, and many frequencies. Equation (1.3) can be generalized for unpolarized light with a number of spatial modes $N = A\Omega/\lambda^2$, $\Omega = \pi$ as follows

$$P = 2\int_0^\infty N\overline{n}h\nu d\nu\,. \tag{1.6}$$

The assumption is that the mean powers in different spatial modes and different frequencies are uncorrelated with each other. This assumption separates the semiclassical theory from the quantum theory. Equation (1.6) can be calculated from the partition function of an equilibrium system of bosons assuming no correlations between states. However, such a method cannot be used to calculate the general form of (1.5). The fluctuations Δn^2 in different states *are* correlated so a density matrix calculation must be used to calculate $\mathrm{NEP}^2_{\mathrm{photon}}$. The off-diagonal terms in the density matrix describe correlations between states. Such calculations were made by Jakeman and Pike[11] to explain quantum optics experiments such as photon counting. Hanbury Brown and Twiss also used a model containing the correlation effects to explain their data in a related experiment[12]. These calculations are numerical and depend on the details of the light source and on the detector's spatial and temporal characteristics.

A limiting form for $\mathrm{NEP}^2_{\mathrm{photon}}$ can be calculated from the work of Kastler[14]. For bosons occupying g cells of phase space where g is large

$$\langle\Delta n^2\rangle_b = \overline{n}^2/g + \overline{n}\,. \tag{1.7}$$

For our example, $g = 2N(B_1\tau_2)$ where the factor 2 arises from two polarizations, N is the number of spatially uncorrelated modes, B_1 is the spectral bandwidth, and $\tau_2 \geq 2C/G$, the minimum post-detection integration time imposed by the thermal response time of the bolometer. Here, $B_1\tau_2$ is the number of statistically independent samples of the output of a bolometer which detects the photons escaping through the hole. In the limit where (1.7) is valid,

$$\mathrm{NEP}^2_{\mathrm{photon}} = 4\int_0^\infty N(\overline{n}^2/g + \overline{n})(h\nu)^2 d\nu\,. \tag{1.8}$$

A physical understanding of the factor g comes from the central limit theorem.We consider only a single spatial mode and concentrate on the factor $B_1\tau_2$ for clarity. Photons emitted from a thermal distribution in a single spatial mode travel in bunches and are

correlated on a time scale $\sim 1/B_1$. If the photon stream is sampled and averaged for bin times $\tau_{\rm bin} \ll 1/B_1$, the distribution of sample means has a sample variance $\langle \Delta n^2 \rangle_b = \overline{n}^2 + \overline{n}$. This is the case calculated in most statistical mechanics texts. The noise on the signal (i.e. the sample mean) is larger than shot noise because the distribution is sampled on a time scale shorter than the correlation time. This corresponds to less than one statistically independent sample of the distribution per bin. If the photon stream is sampled and averaged for bin times $\tau \gg 1/B_1$, there are many statistically independent samples per bin. The central limit theorem[15] states that the distribution of sample means of any distribution with finite true mean μ and variance σ will tend to the normal distribution as the number r of statistically independent samples per bin gets large. Furthermore, the sample variance of the distribution of sample means will decrease as σ/r. In the limit of a large mean, the Poisson distribution also tends to the normal distribution. Since a large bin size implies a large mean, we see that the distribution of sample means tends to the Poisson distribution with variance $\langle \Delta n^2 \rangle_b = \overline{n}$ even when $\overline{n}$ is large.

Jakeman and Pike's numerical calculations show the smooth transition from $\mathrm{NEP}_{\rm photon}$ dominated by wave statistics to $\mathrm{NEP}_{\rm photon}$ dominated by shot noise, solely by increasing the integration time τ_2. The factor of two for polarizations and factor N for spatial modes in g represent additional sources of statistically independent samples which average out the correlations of the wave statistics.

1.4.3 Dicke's radiometer revisited

In 1946, Dicke wrote a well known paper discussing the precision with which a radiometer could measure the power from a blackbody source in the Rayleigh-Jeans limit. The central result of the paper written in our notation is

$$\frac{\Delta P}{P} = \frac{\Delta T_b}{T_b} = \left(\frac{h\nu}{kT_b}\right)^{1/2} (B_1\tau_2)^{-1/2} \ , \tag{1.9}$$

where $B_1 \ll \nu$. Dicke made an analogy to a penny-flipping experiment where the mean number of heads is calculated from a large number of trials r. By analogy, he then argued that the uncertainty in measuring the mean temperature of a blackbody decreases in proportion to $r^{-1/2}$, where $r = B_1\tau_2$ is the number of trials. In the penny-flipping experiment, all trials are statistically independent and the distribution of sample means is Poissonian. This analogy is valid for blackbody radiation when $B_1\tau_2 \gg 1$ and the trials are independent. For $B_1\tau_2 \ll 1$, the trials are no longer independent and the limiting form of Dicke's

equation can be calculated from (1.8) assuming $h\nu \ll kT$ and $B_1 \ll \nu$.

$$\frac{\Delta T_B}{T_B} = (B_1 \tau_2)^{-1}. \tag{1.10}$$

In this regime, the uncertainty in measuring the mean temperature decreases in proportion to τ^{-1}. In other words, the noise integrates away faster than the square root of the integration time.

In a typical submillimeter wave measurement of blackbody power, $B_1\tau_2 \gg 1$ and (1.9) applies. There have been no experiments using a blackbody source which can verify (1.10). However, Jakeman and Pike used a laser beam directed through a rotating ground glass disk which imposed fluctuations $\langle \Delta n^2 \rangle = \overline{n}^2 + \overline{n}$ on the photon distribution. They then varied the integration time τ_2 on a fast photomultiplier tube and verified the predicted photon count distributions for which (1.9) and (1.10) are valid.

In the Wien tail of blackbody radiation where $\overline{n} \ll 1$, we can differentiate (1.3) and use (1.8) to rewrite Dicke's result (1.9).

$$\frac{\Delta P}{P} = \frac{h\nu}{kT_b}\frac{\Delta T_b}{T_b} = \overline{n}^{-1/2}(B_1\tau_2)^{-1/2}. \tag{1.11}$$

In this regime, the precision with which the average power can be measured is limited by shot noise from the incoming photons.

1.4.4 Detector contributions to photon noise

The above expressions for photon noise are valid for all square-law detectors including bolometers, SIS direct detectors, mixers in which the IF signal is rectified, and photodiodes. Although these expressions are not adequate to calculate the effects of the measurement on the radiation field, we will quote some useful results from quantum measurement theory[16, 17].

Coherent detectors which measure both the amplitude and phase of an incoming signal add noise during the detection process to obey the uncertainty principle between amplitude and phase. This result is often referred to as the quantum limit and is due to zero-point fluctuations of the internal degrees of freedom of the coherent detector. Examples of such detectors are a linear voltage amplifier or a mixer where the IF signal is homodyne detected.

Square-law detectors need not contribute additional noise to a photon number measurement since they discard the phase information. Many square-law detectors do

contribute additional noise because of the details of the detection process. For example, a photomultiplier tube with unity quantum efficiency produces A_n charge carriers per photon absorbed. These carriers provide effective photon number gain but also add shot noise. The normalized variance of the output photon number fluctuations referred to the input is approximately[18]

$$\langle \Delta n^2 \rangle = \langle \Delta n^2 \rangle_{\text{photon}} + \langle n \rangle / A_n \,. \tag{1.12}$$

where $\langle \Delta n^2 \rangle_{\text{photon}}$ is the number fluctuations on the incoming photon stream. In the limit of large A_n, however, the shot noise contribution from carriers becomes negligible and the photomultiplier tube approaches an ideal photon counter. Such a detector can, for example, detect amplitude squeezed states $\langle \Delta n^2 \rangle_B < \langle n \rangle$ such as the radiation emitted by an atom in a cavity which is resonantly pumped with a laser[19]. Other detectors with photon number gain which may be able to approach ideal photon counting include avalanche diodes[20], mixers with conversion gain < 0 dB and with the IF signal rectified, and photoconductors with large photoconductive gain.

It has been tacitly assumed that bolometers used to detect high energy photons such as X-rays are indeed ideal photon counters. The energy $h\nu$ deposited by a single X-ray photon can be measured with high resolution by a LHe-cooled bolometer. For millimeter wave photons, however, the intrinsic noise in a LHe-cooled bolometer from thermal fluctuations prevents the bolometer from counting individual photons. The crossover from counting high energy photons to detecting millimeter waves has not been treated in the bolometer literature. We conjecture that the sensitivity of a bolometer in this regime can be understood by rewriting the NEP in terms of the uncertainty in the photon counting rate. By analogy with the photomultiplier tube, we then show that a bolometer can have a large effective photon number gain which leads to ideal photon counting.

Consider a signal power $P = 2N\overline{n}h\nu B_1$ with spectral bandwidth $B_1 \ll \nu$ coupled with unity optical efficiency to a bolometer operating at a temperature T_c connected to a heat sink with temperature $T_s = 0$ via a thermal link G. The minimum value $G = P/T_c$ allows the bolometer temperature to rise to T_c from heating by the signal power. The thermal fluctuation noise in the first term of (1.2) can then be written as $\text{NEP}^2_{\text{thermal}} = 8kT_c\overline{n}h\nu B_1$. We can refer the thermal fluctuation noise in the bolometer to photon fluctuation noise contributed to the signal using (1.8) and write

$$\langle \Delta n^2 \rangle = \langle \Delta n^2 \rangle_{\text{photon}} + \frac{\text{NEP}^2_{\text{thermal}}}{4(\text{h}\nu)^2\text{B}_1} = \langle \Delta n^2 \rangle_{\text{photon}} + \frac{2kT_c}{h\nu}\overline{n} \,. \tag{1.13}$$

Equation (1.13) is equivalent to (1.12) if we identify

$$A_n = \frac{h\nu}{2kT_c} \tag{1.14}$$

as the effective photon number gain of the bolometer. Physically, the effective photon number gain A_n in a low temperature bolometer arises from the many excitations of energy $\sim kT_c$ that are excited when a photon of energy $h\nu \gg kT_c$ is absorbed. An extreme example is a LHe-cooled bolometer used to detect X-rays. The absorption of a single X-ray photon can excite $\sim 10^7 - 10^9$ thermal phonons. Given a suitable readout amplifier, such a bolometer can be thought of as an ideal photon counter.

Chapter 2

High-T_c Bolometers on Sapphire Substrates

Soon after the discovery of high-T_c superconductors, many groups independently recognized that materials such as YBCO could provide a suitable thermometer for a LN-cooled composite bolometer. The performance of the first primitive devices[21]-[23], however, was often orders of magnitude worse than that of room temperature pyroelectric detectors. These devices were limited by materials problems. This chapter discusses the development of two types of composite bolometer on sapphire substrates, both of which have superior sensitivity to commercially available pyroelectric detectors.

2.1 Substrate requirements

The materials requirements for high-T_c bolometers are severe. To achieve sufficient responsivity that Johnson noise and amplifier noise are small, it is necessary to have a superconducting film with a sharp resistive transition $R^{-1}dR/dT$. Also, current-biased YBCO films have $1/f$-like voltage noise which arises from resistance fluctuations. Only the highest quality c-axis epitaxial films have both a sharp resistive transition and low voltage noise. Such films can only be produced on very specific crystalline substrates—or on crystalline substrates coated with thin epitaxial buffer layers.

The substrate contribution to the total heat capacity of a high-T_c bolometer is much larger than for LHe-cooled bolometers. At temperatures $\sim$ 90 K the excitation of thermal phonons dominates the heat capacity of suitable substrates. Table 2.1 is a compila-

Material	κ (W/cm K)	c_p (cal/g K)	Density (g/cm^3)	c_p (J/cm^3 K)
Al_2O_3	1.5	2.3×10^{-2}	4.0	0.39
BN	~ 0.2	4.5×10^{-2}	2.2	0.41
MgO	3.4	3.5×10^{-2}	3.6	0.53
Si_3N_4(amorphous)	0.056	2.6×10^{-2}	2.8	0.31
SiO_2 (fused)	0.0062	5.4×10^{-2}	2.6	0.56
$SrTiO_3$	0.18	5.2×10^{-2}	4.8	1.04
ZrO_2 (fused)	0.015	3.1×10^{-2}	5.6	0.72
Si	5.5	5.5×10^{-2}	2.3	0.53
Diamond	30.0	4.0×10^{-3}	3.5	0.059

Table 2.1: Thermal conductivity κ, specific heat c_p, and density of selected materials at 90 K which were considered for high-T_c bolometer substrates[24, 25]. All materials are crystalline unless indicated.

tion of the thermal properties of such substrates at 90K. Except for diamond, most suitable substrates have similar volume specific heat at 90K. Consequently, when a value of G appropriate for 300K background loading is selected, as in Fig. 1.2, the thermal time constant tends to be long. Therefore, one requirement for a substrate material is strength, so that it can be made thin. Some substrates which are favorable for YBCO film growth, such as $SrTiO_3$ and MgO, are too weak to survive polishing to $\sim 20\,\mu$m thick layers of millimeter dimensions. We chose to use sapphire substrates because of sapphire's mechanical strength and relatively low specific heat.

Diamond has not been used successfully despite its favorable heat capacity and mechanical strength, partly because of the cost of crystalline substrates and partly because carbon degrades YBCO films. Materials such as Si, Si_3N_4, BN, and ZrO_2 can be made into membranes of thickness $\sim 1\,\mu$m which would make superior bolometer substrates if high quality YBCO can be deposited on them. The feasibility of membrane bolometers is discussed in the next chapter.

2.2 Sensitivity limits of high-T_c bolometers

A short calculation shows that thermal fluctuations rather than photon fluctuations limit the best achievable NEP of any high-T_c bolometer for far infrared wavelengths. We consider radiation from a blackbody at temperature T_b which is coupled with unity

optical efficiency to a bolometer via a cold bandpass filter of center frequency ν and bandwidth B_1. The minimum value $G = P_o/(T_c - T_s)$ allows the bolometer temperature to rise from the heat sink temperature $T_s = 77$K to $T_c = 90$K. The thermal fluctuation noise can then be written as

$$\mathrm{NEP}^2_{\mathrm{thermal}} = 4kT_c^2 P_o/(T_c - T_s)\,. \tag{2.1}$$

A bolometer limited by photon fluctuation noise must satisfy the condition $\mathrm{NEP}^2_{\mathrm{photon}} > \mathrm{NEP}^2_{\mathrm{thermal}}$ which can be reduced to $(n+1)h\nu > 4kT_c^2/(T_c - T_s)$ by using (1.6) and (1.8) where we have assumed $B_1\tau_2 = 1$. A high-T_c bolometer viewing a 300K source with unity optical efficiency will be limited by thermal fluctuation noise for $\nu < 6600\,\mathrm{cm}^{-1}$ which corresponds to $\lambda > 1.5\,\mu$m.

2.3 YBCO film noise

In practice, the NEP's of many of our high-T_c bolometers are limited by excess noise in the thermometers. The excess noise depends sensitively on the bias current I, the sharpness of the transition $R^{-1}dR/dT$, the film volume, and frequency. We characterize excess noise in the thermometer by the noise equivalent temperature (NET), which is the smallest detectable temperature change in a 1 Hz noise bandwidth. The NET is defined as

$$\mathrm{NET} = S_v^{1/2}(\omega)\,(IdR/dT)^{-1}\,, \tag{2.2}$$

where $S_v(\omega)$ is the spectral density of voltage fluctuations in the high-T_c film measured at current I and frequency $\omega/2\pi$.

The resulting contribution to the NEP is

$$\mathrm{NEP}_{\mathrm{NET}} = |G + i\omega C| \cdot \mathrm{NET}\,. \tag{2.3}$$

A high-T_c bolometer with a $1\times1\times0.02$ mm sapphire substrate with $\omega\tau = 1$ when $\omega/2\pi = 10$ Hz and $\mathrm{NET} = 10^{-8}\,\mathrm{K/Hz^{1/2}}$ could have an $\mathrm{NEP} \approx 10^{-11}\,\mathrm{W/Hz^{1/2}}$. For comparison, a 1×1 mm pyroelectric detector[9] that is optimized for operation at 10 Hz has $\mathrm{NEP} \approx 1 - 5 \times 10^{-10}\,\mathrm{W/Hz^{1/2}}$.

2.3.1 YBCO on r-plane sapphire

We made our first high-T_c bolometers using YBCO films which were deposited by laser-ablation directly on r-plane $\{\bar{1}012\}$ sapphire. X-ray diffraction measurements, such as

$\theta - 2\theta$ rocking curves, showed these films were highly oriented with the c-axis perpendicular to the substrate surface. Phi ϕ scans of the in-plane epitaxy, however, showed large shoulders on the [103] peak of YBCO indicating poor alignment of the a- and b-axes between grains. Still, typical T_c's were between 85 K and 88 K with transition widths between 0.5 K and 3 K [26].

We measured the voltage noise with an ac-coupled, room temperature transformer and an FET amplifier. The samples were mounted on a temperature-controlled stage in a cryostat and current-biased at values typical for bolometer operation. Figure 2.1a shows the voltage noise for a 300 nm thick YBCO film deposited directly on sapphire. The experiment was done by integrating the noise in a 2 Hz bandwidth for 15 minutes at each temperature point. The noise at the steepest part of the resistive transition is $S_v^{1/2}(f) \approx 2\,\mathrm{nV\,Hz^{-1/2}}$. The slope of the resistive transition is $dR/dT \approx 4\,\Omega/\mathrm{K}$ and the current bias is 3 mA. Using (2.2), the computed NET is $1.7 \times 10^{-7}\,\mathrm{K\,Hz^{-1/2}}$.

The next films we used were 300 nm thick YBCO on a 50 nm thick $SrTiO_3$ buffer layer on r-plane sapphire deposited *in situ* by laser-ablation. These films had similar quality X-ray rocking curves to the YBCO films deposited directly on sapphire. However, the ϕ-scan showed much narrower [103] peaks without the shoulders seen in the film deposited directly on sapphire[30]. This indicates that the $SrTiO_3$ buffer layer is important to obtain in-plane alignment between the c-axis oriented grains. In-plane alignment of the a- and b-axes produces low-angle grain boundaries which result in higher critical current and lower film noise. Figure 2.1b shows the voltage noise and resistance as a function of temperature for such a YBCO film. The slope of the resistive transition is $dR/dT \approx 4\,\Omega/\mathrm{K}$ and the voltage noise on the transition is $S_v^{1/2}(\omega) \approx 0.57\,\mathrm{nV\,Hz^{-1/2}}$. The computed NET is $3 \times 10^{-8}\,\mathrm{K\,Hz^{-1/2}}$. For the measured value of dR/dT, this value of NET is only a factor 2.5 greater than the limit imposed by Johnson noise in the thermometer. This sample was as quiet as the best YBCO films that we have measured to date on any substrate.

2.3.2 Magnetic field dependence of the noise

One contribution to the noise in high-T_c films is switching noise from magnetic flux lines which hop between two pinning sites. The ambient magnetic field in the laboratory is an ample source of such flux lines. Voltage fluctuations with spectral density $S_v(\omega)$ arise from flux motion perpendicular to the direction of current flow[68]. The frequency

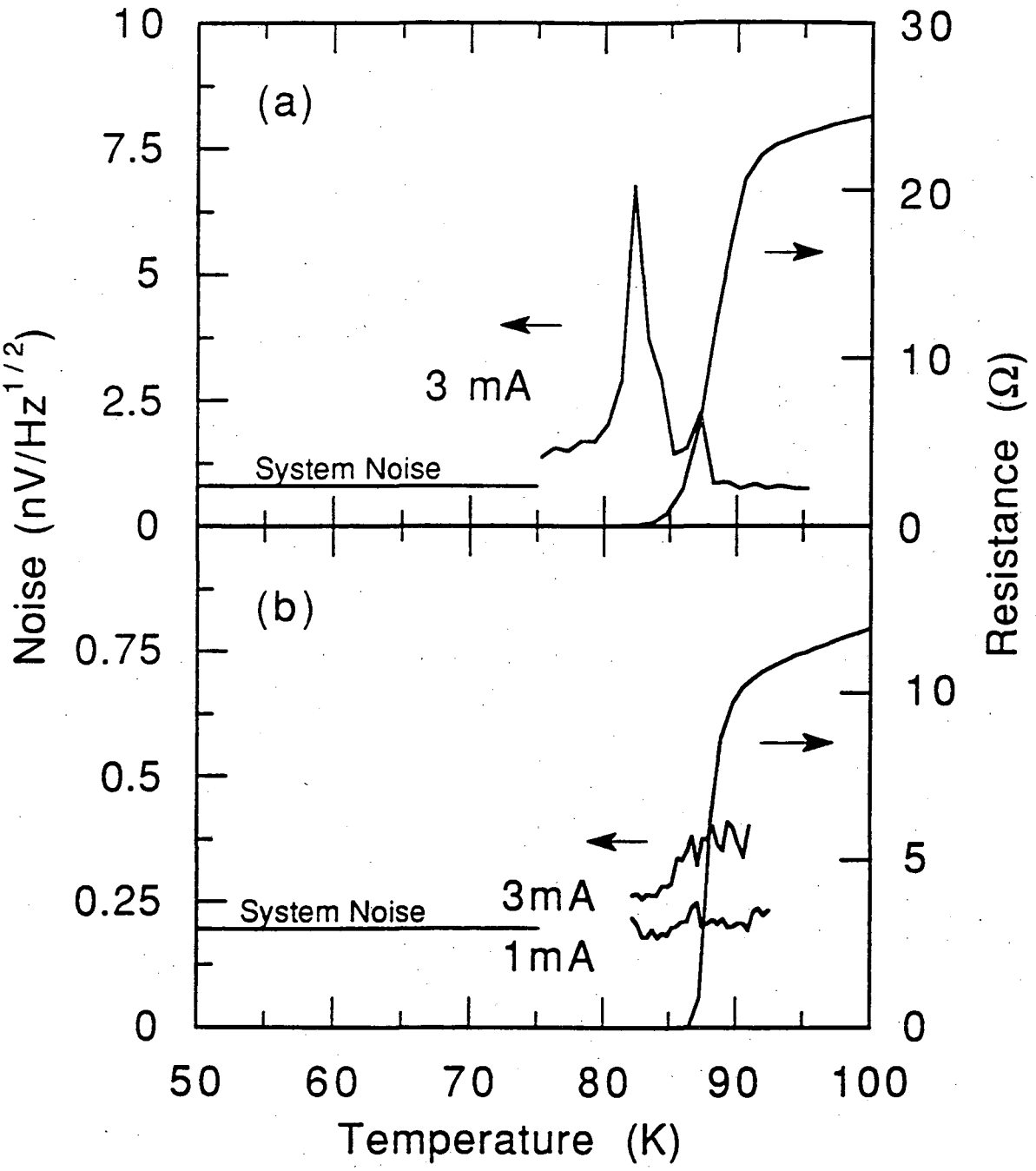

Figure 2.1: Resistance and voltage noise at 10 Hz in current-biased YBCO films as a function of temperature. (a) 300 nm YBCO on r-plane sapphire deposited by laser-ablation. (b) 300 nm YBCO on 50 nm $SrTiO_3$ deposited by laser-ablation.

dependence of $S_v(\omega)$ is determined by the distribution of pinning energies for the trapped flux[28, 29] and the amplitude of $S_v(\omega)$ depends on the number of such processes.

There is a large spike in the noise voltage in Fig. 2.1a slightly below the resistive transition. The spike may arise from trapped magnetic flux lines which de-pin at temperatures near T_c where the pinning energies become weak and thermally activated flux motion occurs. To test this hypothesis, we measured the effect of an external magnetic field on the spike in the noise voltage for a sample[31] which is similar to that shown in Fig. 2.1. Although the resistive transition is broader for this sample, the noise voltage exhibits a similar peak below T_c to Fig. 2.1. This sample was mounted on a variable-temperature stage inserted into the bore of a superconducting magnet. The sample was cooled in the Earth's magnetic field and the field strength was monotonically increased for all the data to avoid any hysteresis arising from trapped flux in the film. Figure 2.2 shows the voltage noise as a function of temperature for different values of applied field. Note the significant increase in the voltage noise and resistance below T_c as the magnetic field is increased. Evidence that thermally activated flux motion dominates the electrical behavior of the film below T_c is shown in Fig. 2.3. Figure 2.3 shows the resistance versus temperature on axes such that a thermally activated process $R(T) \propto \exp(U/kT)$ appears as a straight line. Such a form fits the data below T_c with the various values of the activation energy U indicated for each curve. This phenomenological form uses a homogeneous model to describe an intrinsically inhomogeneous sample and the values of U are a weighted average over temperature and over the film volume of the actual barrier energies for flux pinning.

The number of flux lines per area in a homogeneous film is $N_\Phi \approx B/\Phi_o$ where $\Phi_o = 2.07 \times 10^{-15}\,\mathrm{Wb}$. If individual flux lines move independently of each other, their voltage fluctuations add in quadrature such that $S_v \propto N_\Phi$. The voltage noise at 70 K as a function of monotonically increasing magnetic field is shown in Fig. 2.4. For $B < 0.2\,\mathrm{kG}$, the voltage noise power is $S_v \propto B^\gamma$, where $0.8 \leq \gamma \leq 1$, indicating that the flux lines move independently. In a homogeneous film, the average distance between flux lines is $d \approx N_\Phi^{-1/2}$. At $B = 0.2\,\mathrm{kG}$, $d \approx 0.3\,\mu\mathrm{m}$. At higher B-field strengths ($d < 0.3\,\mu\mathrm{m}$), the data in Fig. 2.4 have $\gamma \approx 2$ and $S_v \propto N_\Phi^2$. In this regime, the flux lines interact and large bundles of flux lines move together such that the associated voltage fluctuations add coherently.

We made similar noise measurements in a magnetic field on high-quality YBCO samples on MgO substrates with in-plane epitaxy. These samples showed no peak in the voltage noise below T_c and the magnetic field had almost no effect on the noise. We

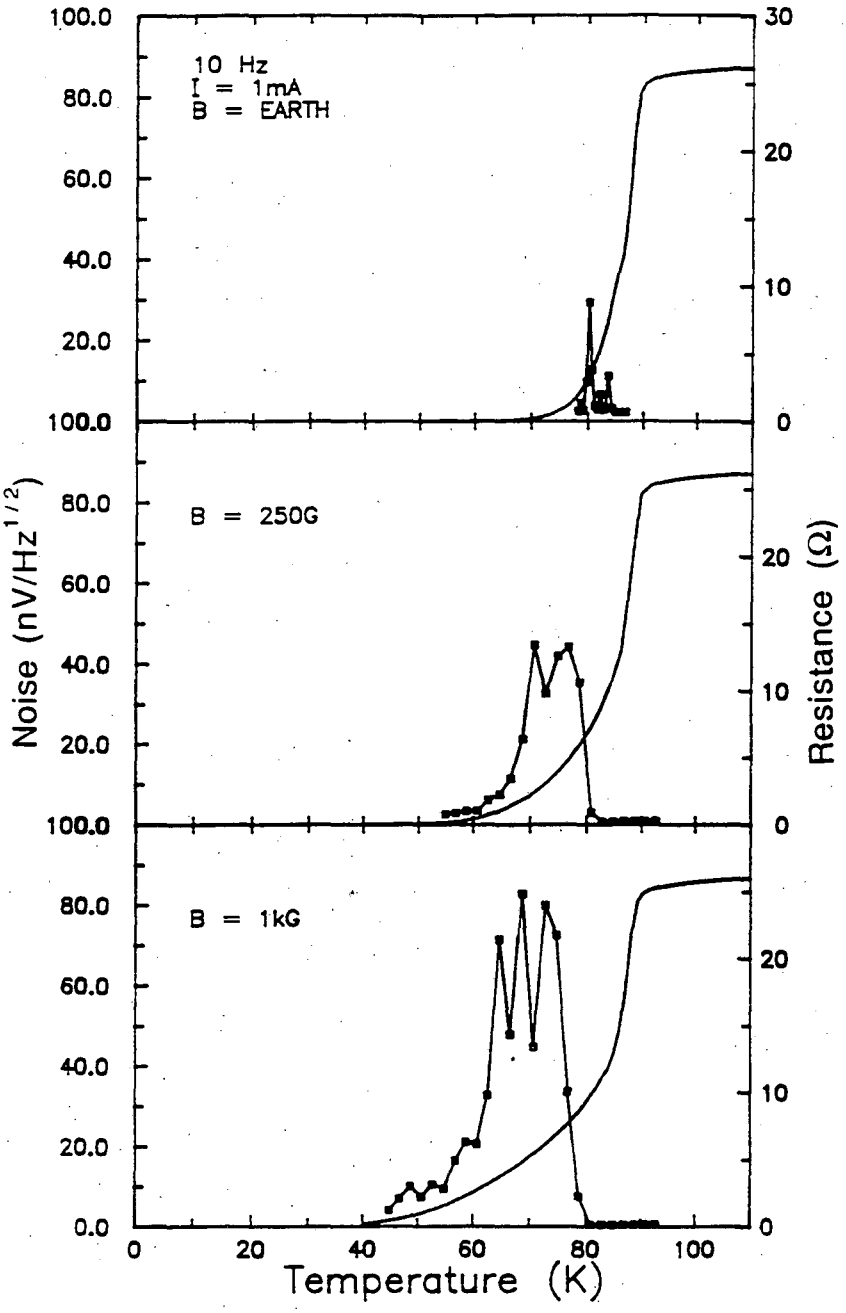

Figure 2.2: Resistance and voltage noise at 10 Hz in current-biased YBCO films on sapphire as a function of temperature for three values of applied magnetic field. The field was increased monotonically to avoid hysteresis effects.

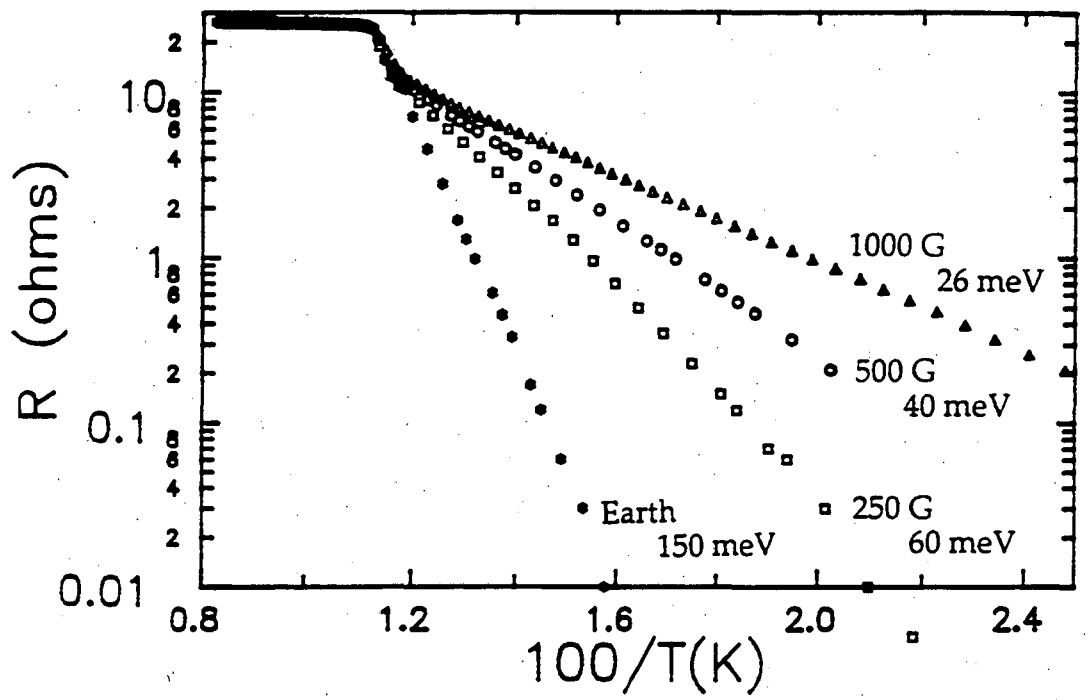

Figure 2.3: Resistance as a function of temperature for YBCO films on sapphire for various applied magnetic fields. The activation energies for thermally activated flux motion were extracted from the slopes of straight lines drawn through the data below T_c.

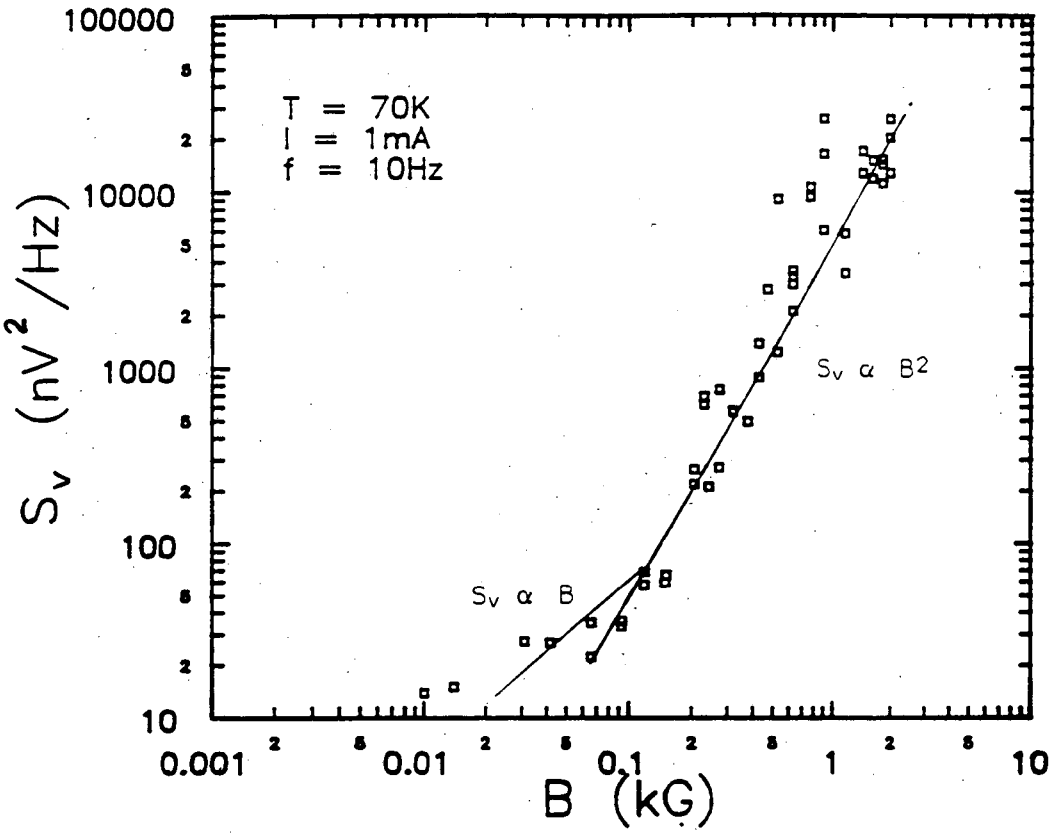

Figure 2.4: Voltage noise at 10 Hz in current-biased YBCO films on sapphire as a function of magnetic field. Lines for $S_v \propto B$ and $S_v \propto B^2$ are drawn as guides to the eye.

conjecture that the magnetic field-dependent noise shown in Fig. 2.2 arises from flux motion along the high angle grain boundaries between c-axis oriented grains in the YBCO film on sapphire.

2.4 Bolometer assembly

An important application for high-T_c bolometers is in laboratory infrared spectrometers with blackbody radiation sources. At long wavelengths, the blackbody power which couples to the bolometer decreases unless the bolometer area is increased in proportion to λ^2. We fabricated 1×1 mm bolometers for wavelengths from $20 - 100\,\mu$m and 3×3 mm bolometers for $100 - 300\,\mu$m. Films of c-axis oriented YBCO with in-plane epitaxy were produced by *in situ* laser ablation of 300 nm of YBCO on top of a buffer layer on the sapphire.[30] The 1×1 mm bolometer had a 50 nm thick buffer layer of $SrTiO_3$ and the 3×3 mm bolometer had a double buffer layer of 10 nm of Y_2O_3 on top of 10 nm of yttria-stabilized zirconia.

After removing the sample for the 1×1 mm bolometer from the YBCO deposition chamber, we sputter-cleaned the YBCO surface in a 1:5 O_2 + Ar gas mixture and then sputter deposited 200 nm of Ag *in situ*. For the sample which would become the 3×3 mm bolometer, we patterned the YBCO by lithography and then deposited Ag contacts. Each of the $6 \times 6 \times 0.5$ mm sapphire substrates was then waxed face down onto a polishing block and lapped to $20\,\mu$m thickness. The substrate was diced into bolometer chips which were annealed in 1 atm of oxygen at 550° C for at least 30 minutes to obtain electrical contacts with low noise. The bolometer chips were suspended in a temperature regulated brass ring and then a radiation absorber was deposited on the back side. Two $25\,\mu$m diameter Cu wires were attached by silver paint to serve both as electrical leads and as a weak thermal link to the brass ring. Figure 2.5 schematically shows the completed bolometers.

The spectral response of the bolometer is determined by the radiation absorber attached to it. Radiation incident on the back side of the bolometer in Fig. 2.5a is absorbed by a $10\,\mu$m thick layer of gold black. Gold black is a porous matrix of microscopic gold clusters which absorbs radiation from $1 - 100\,\mu$m by multiple scattering[32]. It can be produced by evaporating gold in the presence of $\sim 5 - 10$ Torr of argon. The density of gold black is $\sim 0.1\%$ that of solid gold and only increases the heat capacity of the composite bolometer by 0.3%. At 90K, gold black is in thermal equilibrium with the bolometer substrate.

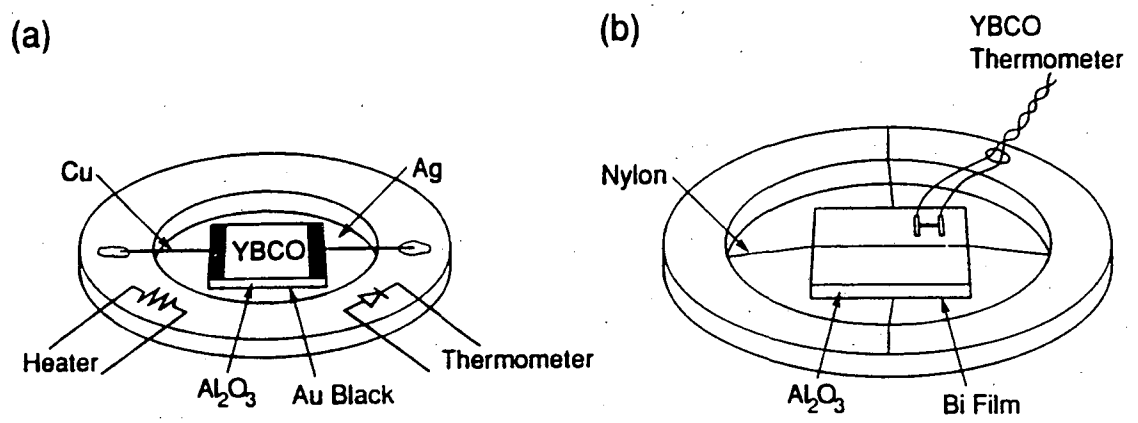

Figure 2.5: Schematic diagram of two high-T_c bolometer architectures. (a) A $1 \times 1 \times 0.02$ mm bolometer for wavelengths $\lambda < 100\,\mu$m with an unpatterned YBCO thin film thermometer on a sapphire substrate and an infrared absorber of gold black. (b) A $3 \times 3 \times 0.02$ mm bolometer for $\lambda > 100\,\mu$m with a patterned YBCO thermometer on sapphire and a thin Bi film as the infrared absorber.

During our first attempts at gold black deposition, radiation from the tungsten evaporation filament heated up the bolometer and the YBCO thermometer lost some oxygen. Consequently, the resistive transition broadened and the electrical noise increased slightly. Also, the gold black matrix partially collapsed because of the heating. This problem was solved by using a narrow gauge tungsten filament bent into a V-shape. This geometry minimized the throughput for infrared emission from the filament and significantly reduced the radiative heating of the bolometer during gold black deposition.

Radiation incident on the front side of the bolometer in Fig. 2.5b passes through the substrate and is absorbed on the back side by a 42 nm thick Bi film of $200\,\Omega$ sheet resistance. This configuration absorbs up to $\sim 50\%$ of the incident radiation and minimizes standing wave resonances in the sapphire substrate for light of normal incidence[2].

2.5 Bolometer characterization

Both bolometers were characterized with electrical and optical measurements. For brevity, we will only describe measurements for the 1×1 mm bolometer. The bolometer responsivity was calculated from electrical measurements. The inset of Fig. 2.6 shows the resistive transition of the thinned bolometer chip for a 1 mA bias current. Comparison with

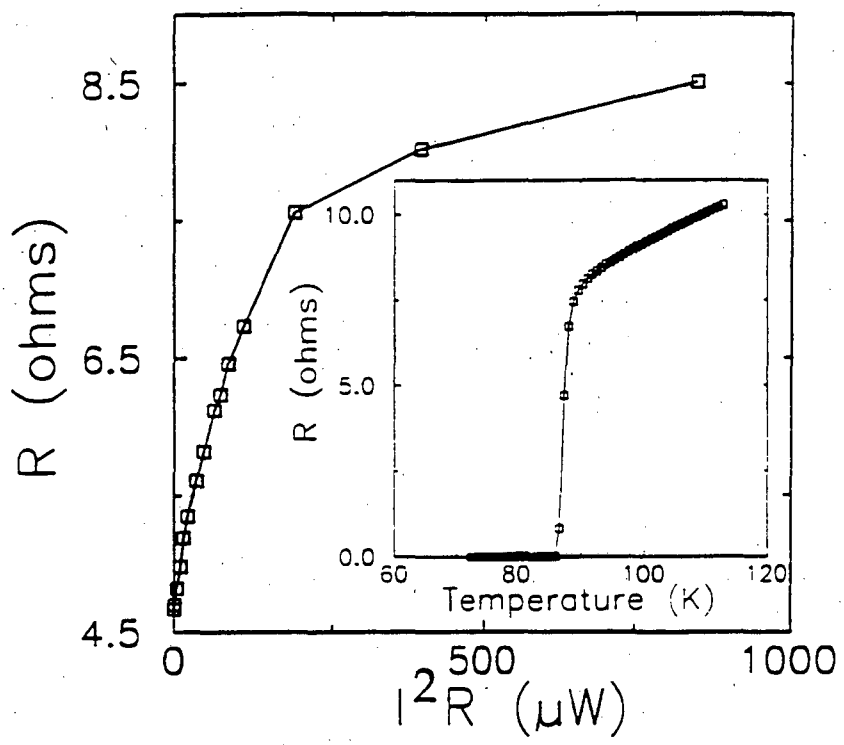

Figure 2.6: Resistance of the bolometer as a function of electrical heating from the bias current. The nonlinearity of this curve arises from the temperature rise and the dependence of the resistance on temperature. Inset: R(T) for the bolometer measured at 1mA.

measurements made immediately after YBCO deposition showed no noticeable degradation. The steepest part of the resistive transition has a slope $dR/dT = 6.2\,\Omega/\mathrm{K}$ where $R = 3\,\Omega$. Figure 2.6 shows the dependence of the bolometer resistance on power dissipated by the bias current. The shape of this curve is consistent with bias power heating, assuming that the isothermal film is ohmic. The thermal conductance $G = 2.7 \times 10^{-4}\,\mathrm{W/K}$ was obtained from $R(T)$ and from the slope at small bias power I^2R.

The bolometer time constant $\tau = 55\,\mathrm{ms}$ was obtained by measuring the high frequency roll-off of the response to chopped light from a He-Ne laser. We infer a value $C = 1.5 \times 10^{-5}\,\mathrm{J/K}$ from the measured values of G and τ. This value is consistent with the value $C = 1.2 \times 10^{-5}\,\mathrm{J/K}$, computed from handbook data, and gives us confidence in the value G calculated from Fig 2.6. From the measured values of G, dR/dT, and τ, we calculate a responsivity of $S = 19\,\mathrm{V/W}$ at 10 Hz and $I = 3\,\mathrm{mA}$.

The spectral response of the bolometer was first measured at visible wavelengths

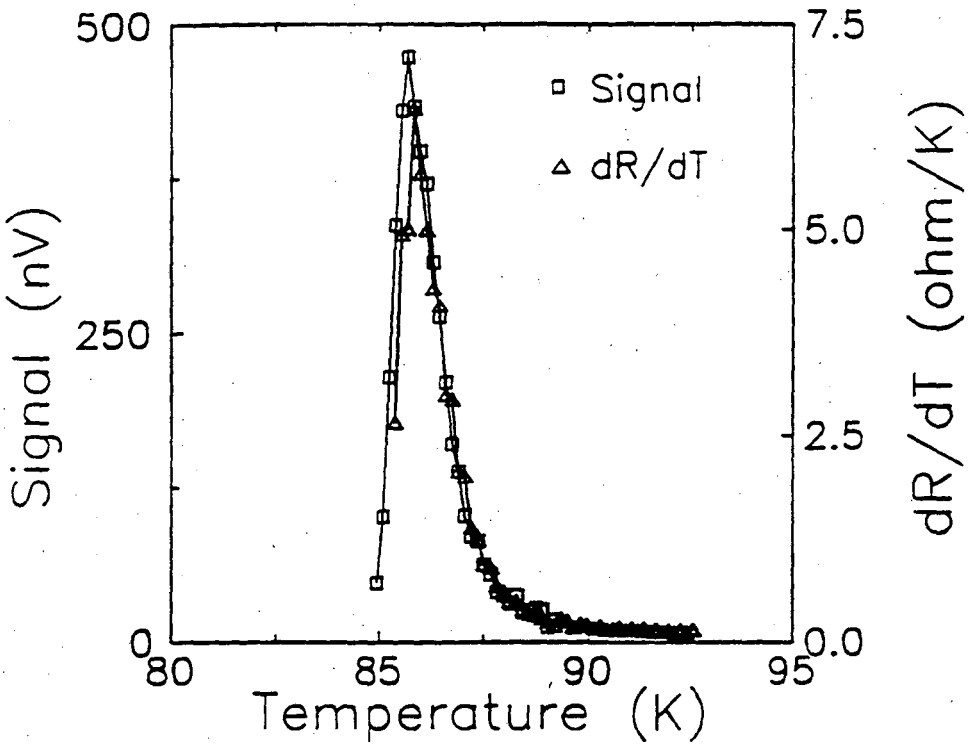

Figure 2.7: Voltage response of the bolometer to chopped laser light compared with dR/dT. The similarity of the two curves indicates that the response is bolometric.

with 632 nm He-Ne laser light. The YBCO film, which has an absorptivity[33] of $\sim 90\%$ at this wavelength, was used as the radiation absorber. Figure 2.7 compares the response to chopped laser light with the slope of the resistive transition. These data are consistent with bolometric response. The peak signal corresponds to an optical responsivity of $S = 17\,\mathrm{V/W}$ at 10 Hz.

Using the measured noise and optical responsivity, we compute the optical NEP = $2.4 \times 10^{-11}\,\mathrm{W\,Hz^{-1/2}}$. The maximum current allowed by the stability condition is I = 4mA. Assuming that the excess noise in a better sample would be less than Johnson noise, the NEP could be improved to $10^{-11}\,\mathrm{W\,Hz^{-1/2}}$ at 10 Hz.

The 3×3 mm bolometer with a Bi absorber was characterized in a similar fashion. In this case $G = 3.4 \times 10^{-4}$ W/K, $\tau = 120$ ms, and $C = 4 \times 10^{-5}$ J/K. In this geometry, the YBCO was patterned into a $50 \times 600\,\mu$m strip to avoid obscuring the incident light before it reaches the absorber. At the midpoint of the transition $R = 110\,\Omega$ and $dR/dT = 36\,\Omega$/K. Measurements of the voltage noise with $I = 1$ mA gave NET = $1.4 \times 10^{-7}\,\mathrm{K/Hz^{1/2}}$. In

general, we observe that patterned YBCO films of small size tend to have high excess voltage noise and poor NET. We calculate an electrical NEP = $3.6 \times 10^{-10}\,\mathrm{W/Hz^{1/2}}$ at 10 Hz for the 3 x 3 mm bolometer.

2.6 Spectral measurements.

We measured the response of both bolometers to infrared light using a Fourier transform spectrometer in the step-and-integrate mode with a quartz mercury arc source. Radiation from the spectrometer output was coupled to the detector through a brass light pipe and a light concentrating cone. A room temperature filter of 25 μm thick black polyethylene in the light pipe blocked visible radiation.

Figure 2.8 compares the ratio of two identical spectra with a resolution of $4\,\mathrm{cm^{-1}}$ measured with the pyroelectric detector[9] and with the high-T_c bolometer. The optical throughput was intentionally restricted such that detector noise would appear in the spectra. The deviation from unity of this ratio is a measure of the detector sensitivity. Clearly the high-T_c bolometer is more sensitive. There is a strong reflection mode in sapphire which may account for the feature at $450\,\mathrm{cm^{-1}}$ in Fig. 2.8a. This would indicate that some of the infrared radiation is transmitting through the gold black absorber and into the sapphire bolometer substrate.

Another demonstration of detector sensitivity is to measure the absorption spectrum of water vapor with the highest frequency resolution possible without detector noise obscuring the spectrum. We filled 75 cm of 1.3 cm diameter light pipe with 50 Torr of water vapor. Figure 2.9a shows the resulting transmittance spectrum measured with the 1 x 1 mm bolometer with H_2O rotational lines resolved to $1\,\mathrm{cm^{-1}}$. Figure 2.9b shows lower frequency H_2O rotational lines measured with the 3 x 3 mm bolometer and resolved to $0.5\,\mathrm{cm^{-1}}$. Both spectra were measured for 20 min. and agree with previously published measurements[34].

In summary, we have fabricated, and tested the first high-T_c bolometers with higher sensitivity than competing room temperature detectors. A 1 x 1 mm bolometer with a radiation absorber of gold black smoke has a noise equivalent power NEP = $2.4 \times 10^{-11}\,\mathrm{W/Hz^{1/2}}$ at 10 Hz and has useful sensitivity over wavelengths $20 - 100\,\mu$m. A 3 x 3 mm bolometer with a Bi film radiation absorber has NEP = $3.6 \times 10^{-10}\,\mathrm{W/Hz^{1/2}}$ at 10 Hz and has useful sensitivity over wavelengths $100 - 300\,\mu$m. Water vapor transmission spectra

were measured to demonstrate the sensitivity of both devices.

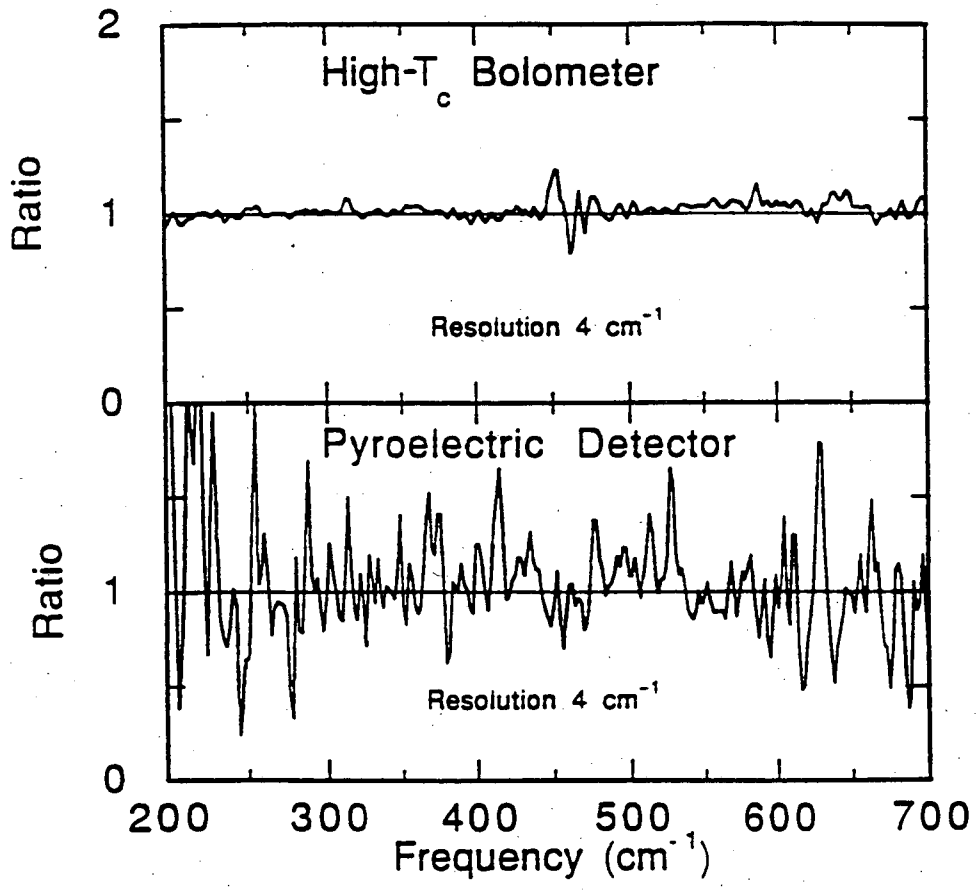

Figure 2.8: (a) Ratio of two identical spectra with $4\,\mathrm{cm}^{-1}$ resolution measured with the high-T_c bolometer. (b) Ratio of two identical spectra with $4\,\mathrm{cm}^{-1}$ resolution measured with a pyroelectric detector. The optical efficiency was intentionally degraded so that the noise could be seen clearly. The throughput and efficiency were nominally identical for both ratios.

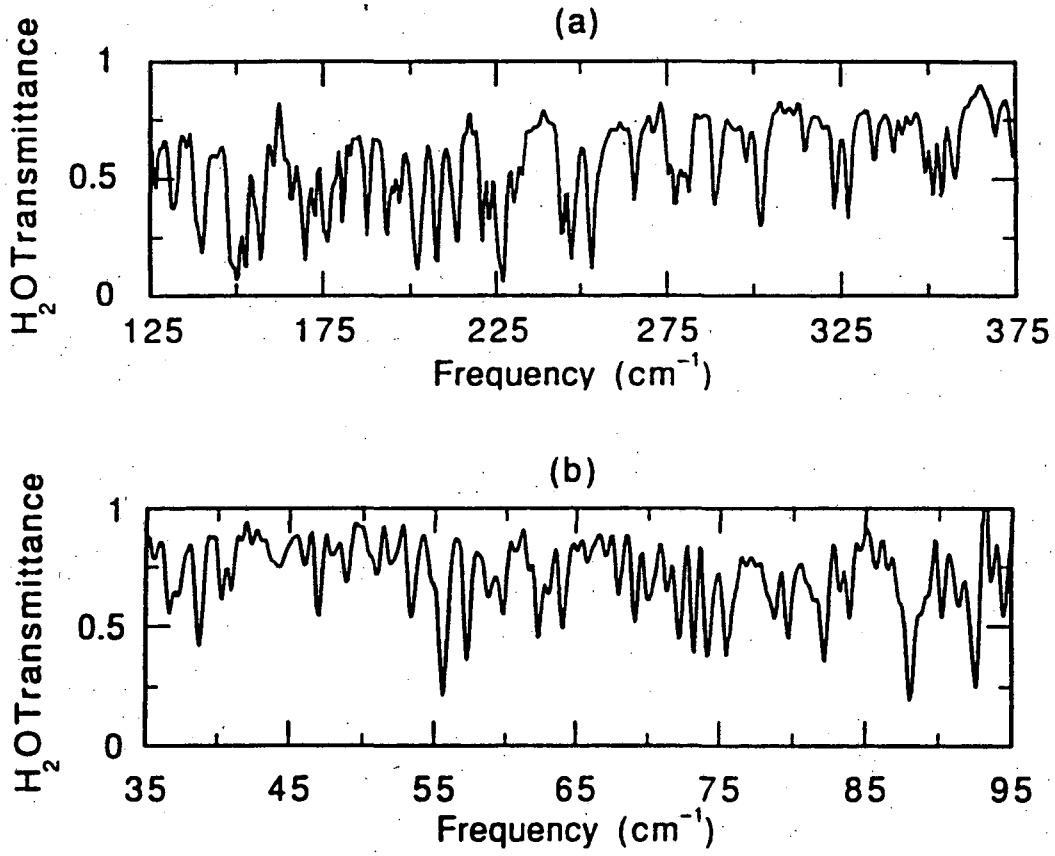

Figure 2.9: Transmittance spectra of 50 Torr of water vapor measured with high-T_c bolometers. (a) Rotational modes of H_2O resolved to $1\,cm^{-1}$ with the bolometer in Fig. 2.5a. (b) Rotational modes of H_2O resolved to $0.5\,cm^{-1}$ with the bolometer in Fig. 2.5b.

Chapter 3

Imaging Arrays of High-T_c Bolometers

The composite high-T_c bolometers on sapphire substrates described in Chapter 2 were designed for single pixel applications such as far-infrared laboratory spectroscopy. The areas of these bolometers were chosen from 1 to 10 mm^2 to match the throughput of laboratory Fourier transform spectrometers. For such large areas, there are stringent requirements on thermometer sensitivity which require the use of high quality epitaxial c-axis $YBa_2Cu_3O_{7-\delta}$ (YBCO) films on favorable substrates with sharp resistive transitions and low voltage noise under current bias. Arrays of much smaller bolometers are potentially useful for thermal imaging. The absorbing area A can be as small as the diffraction limit $A = \lambda^2/\Omega$, where Ω is the solid angle of the pixel's field of view. The lower heat capacity of such small bolometers relaxes the requirement on thermometer sensitivity. The possibility then exists that YBCO on amorphous substrates like silicon nitride (Si_3N_4) could be used. Researchers at Honeywell are working on linear arrays of micromachined bolometers on substrates of Si_3N_4 membranes for thermal imaging at 10μm[35].

This chapter discusses the sensitivity of high-T_c bolometers as a function of thermometer NET, bolometer area, and wavelength. The discussion is directly relevant to the design of imaging arrays of high-T_c bolometers for wavelengths from $10 - 1000\,\mu$m. The required thermometer sensitivity for bolometers of various areas will be compared with the voltage noise $S_v^{1/2}(f)$ measured for current-biased YBCO films on various substrates. Next, a design is developed for a single pixel in an array of Si membrane bolometers operating

at the diffraction limit for $\lambda = 100\,\mu$m. A more general design is then presented for other wavelengths, optical systems, and membrane materials. We will also discuss a scheme for reading out two dimensional bolometer arrays which performs real-time signal integration on the chip.

3.1 Resistance fluctuations

Our own measurements on YBCO films and those of others[37, 38] indicate that the excess voltage noise in current-biased films depends sensitively on film quality. It can be modeled as resistance fluctuations, $S_v(\omega) = (I\delta R)^2$, where $[\delta(\ln R)]^2$ usually has a frequency dependence between ω^{-1} and ω^{-2}, and scales roughly as the reciprocal of the film volume[39]. A resistance fluctuation δR can be written as the noise equivalent temperature using (2.2)

$$\mathrm{NET} = \delta(\ln R)R(dR/dT)^{-1}, \tag{3.1}$$

where $R(dR/dT)^{-1}$ is roughly the width of the resistive transition. For thermometer materials with resistance fluctuation noise, the film noise term in the NEP (2.3) will dominate other contributions to the NEP from readout noise if the bias current is made large enough that

$$I\delta R > \left[4kT_cR + e_n^2 + (i_nR)^2\right]^{1/2}. \tag{3.2}$$

As will be discussed below, this condition can be met for all of the YBCO films we have measured to date without exceeding the thermal stability constraint set by bias heating.

Phenomena such as thermopower, Bi film resistance, gas expansion, and dielectric constant changes have been used as thermometers for thermal far-infrared detectors operating above 77 K[40]-[44]. For applications with frequencies less than 100 Hz, the best NET of these technologies is in the range of $10^{-6}\,\mathrm{K\,Hz^{-1/2}}$. If these thermometer technologies are restricted to thin films useful for large micromachined arrays[42], such as bismuth films, the NET is $> 10^{-5}\,\mathrm{K\,Hz^{-1/2}}$. High-$T_c$ thin film thermometers promise values of NET $< 10^{-8}\,\mathrm{K\,Hz^{-1/2}}$, and hence orders of magnitude increase in detector sensitivity.

3.2 NET measurements for YBCO thermometers

Fabrication of useful high-T_c composite bolometers requires films on very thin substrates to minimize heat capacity. We have chosen to study films on sapphire, silicon, and

Sample	Source	Geometry	R(dR/dT)$^{-1}$ [K]	δ(ln R) [Hz$^{-1/2}$]	NET [K Hz$^{-1/2}$]	ρ_{dc} (midpoint) [$\mu\Omega$ cm]
A	Conductus	1 x 1 mm x 300 nm YBCO on 20 nm $SrTiO_3/Al_2O_3$	1	3×10^{-8}	3×10^{-8}	37
B	Xerox	1 x 3 mm x 40 nm YBCO on 50 nm YSZ/Si	2.6	3×10^{-8}	8×10^{-8}	55
C	Conductus	3 x 3 mm x 300 nm YBCO on 20 nm YSZ/Si_3N_4	6	4×10^{-7}	2.4×10^{-6}	270
D	Xerox	1 x 3 mm x 40 nm YBCO on 50 nm YSZ/Si	5	10^{-6}	5×10^{-6}	190

Table 3.1: Characteristics of YBCO films for use as thermometers on high-T_c bolometers.

silicon nitride substrates which are strong enough to be made thin. Table 3.1 summarizes the properties of four YBCO films which were deposited by laser ablation at Conductus and Xerox. These are representative of the best performance that has been obtained to date. Samples A and B were epitaxial c-axis films deposited on crystalline substrates with buffer layers. Sample A was made *in situ* by depositing a 20 nm thick buffer layer of $SrTiO_3$ on $\{1\bar{1}02\}$ sapphire followed by 300 nm of epitaxial c-axis YBCO[30]. After breaking vacuum, silver contact pads were sputter-deposited through a shadow mask and annealed in oxygen at 500°C for 60 min. Sample B was made using a silicon substrate. A process was specifically developed to provide a pristine Si surface for epitaxial growth[45, 46]. First, a weak HF and ethanol solution was used to strip the native SiO_2 layer and to terminate the exposed silicon bonds with hydrogen. Then the Si substrate was transferred to the deposition system via a nitrogen gas-purged glove box and load-lock. The substrate was heated in vacuum to drive off the hydrogen and 40 nm of YBCO was deposited *in situ* on a 50 nm thick yttria stabilized zirconia (YSZ) buffer layer. Because of the difference in thermal expansion between silicon and YBCO, the YBCO films are under tensile stress and must be grown thinner than $\sim$ 50 nm to avoid cracking. Silver contacts were again sputter-deposited but were not annealed to avoid driving surface contaminants into the thin YBCO film. Samples C and D were mostly c-axis YBCO deposited on amorphous Si_3N_4 films with YSZ buffer layers. The Si_3N_4 films were deposited on Si at 850°C by Low Pressure Chemical Vapor Deposition (LPCVD) at 350 mTorr using SiH_2Cl_2 and NH_3. The YBCO films were deposited by a laser ablation process similar to that used for sample A.

We measured the voltage noise with an AC-coupled, room temperature transformer

and an FET amplifier. The samples were mounted on a temperature-controlled stage in a cryostat and current-biased at values typical for bolometer operation. Figure 3.1 shows the voltage noise for epitaxial samples A and B. The experiment was done by integrating the noise in a 2 Hz bandwidth for 15 minutes at each temperature point. The noise at the steepest part of the resistive transition for Sample A ($YBCO/SrTiO_3/Al_2O_3$) gives NET = $3 \times 10^{-8}\,K\,Hz^{-1/2}$. This sample was as quiet as the best YBCO films that we have measured to date on any substrate. In general, films that satisfy other standard requirements for quality (e.g. large J_c, small ΔT) consistently show low noise before processing. Samples A and B had high critical current ($J_c > 10^6 A/cm^2$, $T = 77K$) and, as shown in Table I, narrow resistive transitions, and low resistance fluctuation noise. Processing, especially in the form of narrow, patterned lines, has been observed to increase noise. Therefore, we have avoided extensive processing of the films after deposition by using large area YBCO thermometers with the minimum resistance necessary to satisfy (3.2). This approach also minimizes film volume dependent mechanisms for 1/f noise. Also, poor quality films tend to degrade more rapidly with processing than high quality films. After the substrate thickness of Sample A was reduced by grinding to 25μm, it was used for the composite bolometer with a gold black absorber described in Chapter 2. The best NET yet obtained for YBCO on a silicon substrate is NET = $7 \times 10^{-8} K\,Hz^{-1/2}$.

The resistive transitions for samples C and D of $YBCO/YSZ/Si_3N_4$ shown in Fig. 3.2 are significantly broader than for samples A and B and the voltage noise is higher. Consequently, the values of NET are about 100 times poorer. In general, we expect that YBCO samples with poor epitaxy make noisier thermometers. One contribution is switching noise from thermally activated flux motion, as described in Chapter 2. Based on our experience with other substrates, we expect that the NET's for YBCO films on Si_3N_4 will improve as that technology matures.

3.3 Design of a Si membrane bolometer

For practical reasons, bolometers for use in large format imaging arrays must be produced by optical lithography and micromachining. Silicon and Si_3N_4 are well suited to such fabrication techniques. Yttria-stabilized zirconia is another candidate membrane material. It is compatible with high quality YBCO thermometers, has low thermal conductivity, and can be etched into free-standing membranes [47]. In this section we discuss the

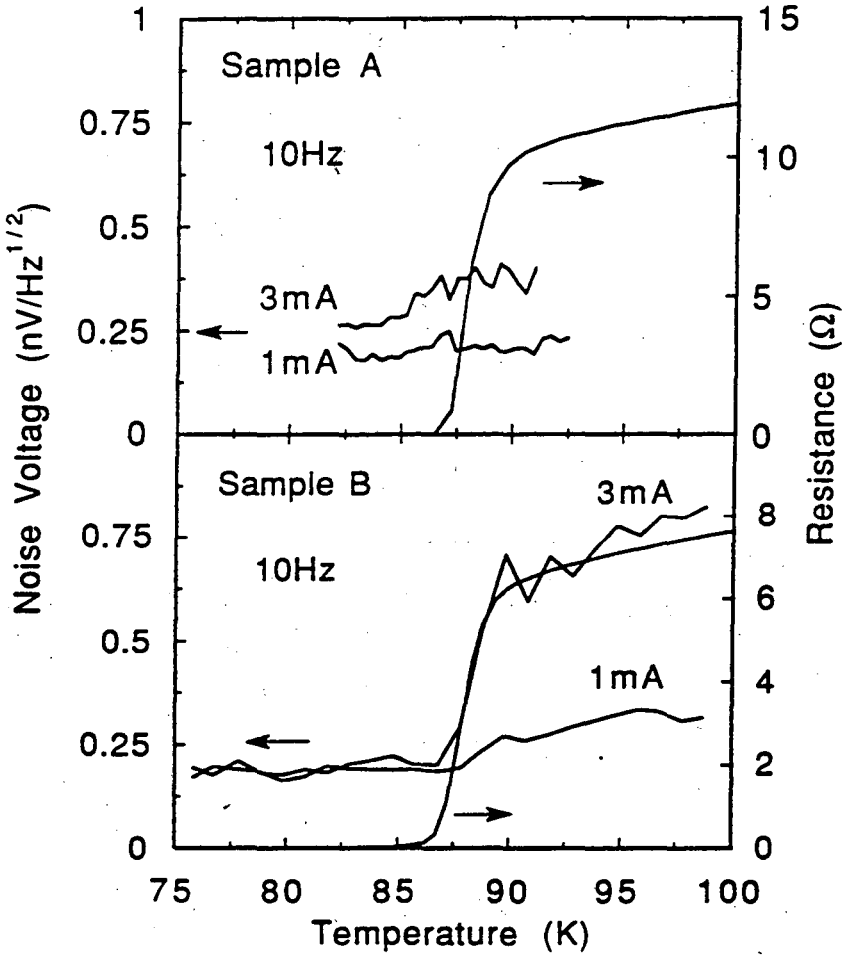

Figure 3.1: Resistance and voltage noise at 10 Hz in current-biased YBCO films as a function of temperature. The noise in the measurement system is 0.15 $nV/Hz^{1/2}$. Sample A is 300 nm of epitaxial YBCO on a 20 nm buffer layer of $SrTiO_3$ on sapphire. Sample B is 40 nm of epitaxial YBCO on a 50 nm buffer layer of yttria-stabilized zirconia on silicon.

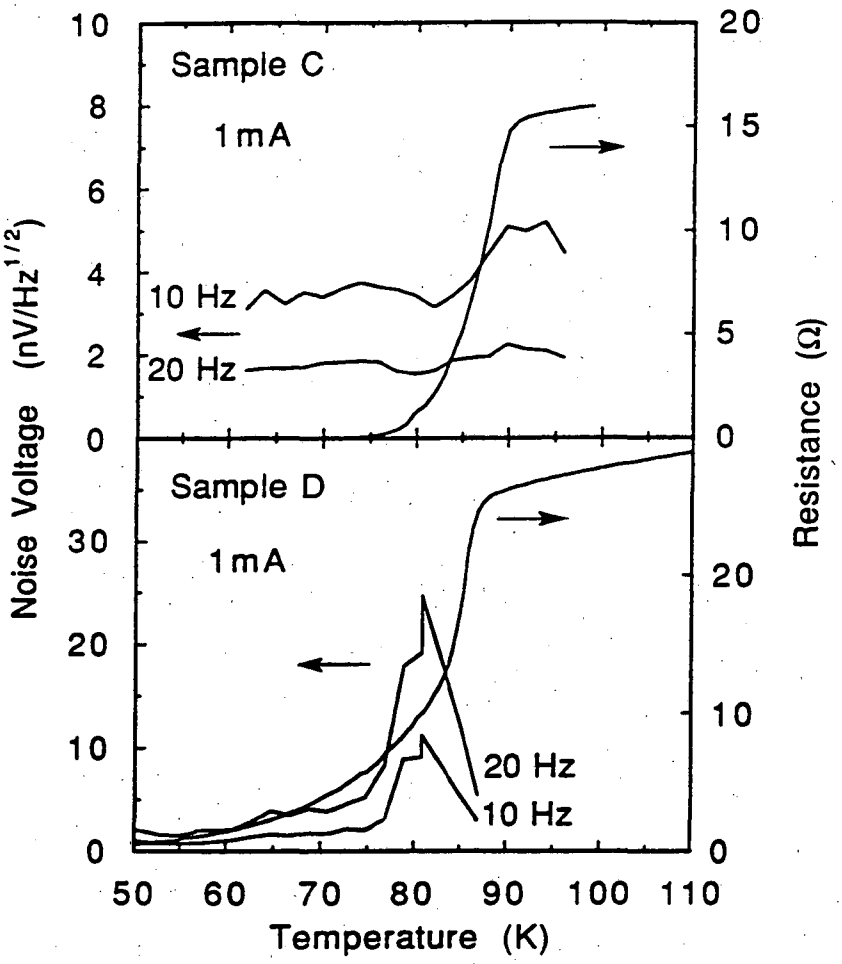

Figure 3.2: Resistance and voltage noise at 10 Hz in current-biased YBCO films as a function of temperature. The noise in the measurement system is 0.15 $nV/Hz^{1/2}$. Sample C is 300 nm YBCO on a 20 nm buffer layer of yttria-stabilized zirconia on Si_3N_4. Sample D is 40 nm YBCO on a 50 nm buffer layer of yttria-stabilized zirconia on Si_3N_4.

thermal properties of a silicon membrane bolometer pixel and estimate its sensitivity.

For a given optical system, the area of a pixel which couples optically to N spatial modes is proportional to the wavelength squared

$$A = \lambda^2 N/\Omega, \tag{3.3}$$

where Ω is the solid angle of the field of view of the pixel. The goal of this design is an imaging array with f/6 optics ($\Omega = 0.02\,\mathrm{sr}$) which has useful sensitivity for wavelengths $30 - 100\,\mu\mathrm{m}$ and is diffraction-limited ($N = 1$) at $\lambda = 100\,\mu\mathrm{m}$. From (3.3), the pixel size is $0.7 \times 0.7\,\mathrm{mm}$. Using handbook values [24], we estimate the heat capacity for a $0.5\,\mu\mathrm{m}$ thick Si membrane to be $C = 1.5 \times 10^{-7}\,\mathrm{J/K}$. For a thermal conductance $G = 5 \times 10^{-5}\,\mathrm{W/K}$, the thermal response time is $\tau = C/G = 3\,\mathrm{ms}$. Such a thermal conductance can be achieved with two $1000 \times 90 \times 0.5\,\mu\mathrm{m}$ legs of Si which support the membrane. Figure 3.3 is a diagram of such a bolometer with the width of the Si legs exaggerated for clarity. From (1.2), the limit to the NEP from thermal fluctuations for this bolometer is $\mathrm{NEP} = 3 \times 10^{-12}\,\mathrm{W\,Hz^{-1/2}}$. If sample B from Table I were used as the thermometer, then $\mathrm{NEP} = 5 \times 10^{-12}\,\mathrm{W\,Hz^{-1/2}}$. This NEP is significantly better than the $\mathrm{NEP} = 3.5 \times 10^{-11}\,\mathrm{W\,Hz^{-1/2}}$ of the best Schwartz-type thermopiles used in this wavelength range [5].

We have fabricated $0.5\,\mu\mathrm{m}$ thick Si membranes which are supported by two $1000 \times 100 \times 0.5\,\mu\mathrm{m}$ legs. The membrane was defined with an etch-stop layer produced by selective ion implantation of 180 keV BF_2^+ at a dose of $10^{16}\,\mathrm{cm^{-2}}$. After a 60s anneal at 1000°C, the Si samples were etched in a solution of 80°C KOH. There are some disadvantages to the boron etch stop. The boron concentration results in a degenerately doped Si membrane which is under tensile stress and may be difficult to fabricate reproducibly to the dimensions needed for sensitive high-T_c bolometers. Also, a degenerately doped Si membrane has a high infrared conductivity which renders resistive submillimeter radiation absorbers, such as Bi films, ineffective [2]. Gold black radiation absorbers should be satisfactory for shorter wavelengths. We are presently investigating an electrochemical etch-stop which uses a reverse-biased $p - n$ junction to slow the Si etch rate in KOH [48]. This technique requires much lower ion implantation doses of $\sim 10^{12}\,\mathrm{cm^{-2}}$ and may solve some of the problems associated with the BF_2^+ ion implant.

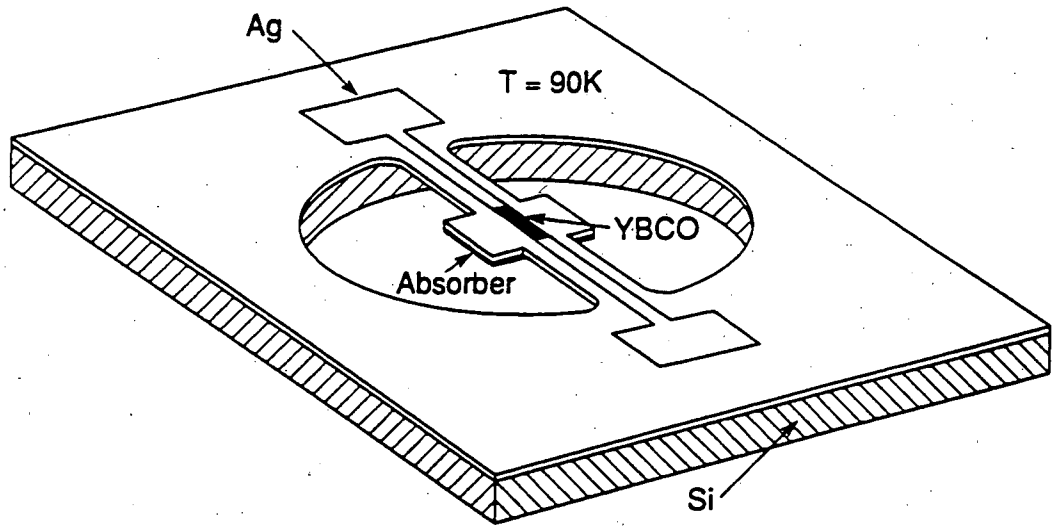

Figure 3.3: Diagram of a membrane bolometer. The bolometer consists of a radiation absorber and a YBCO thermometer deposited on a membrane of Si or Si_3N_4 which is isolated from heat heat sink by two legs of the same membrane material.

3.4 Optimizing membrane bolometer design

The previous section outlined the basic design of a Si membrane bolometer for an array of bolometers which are diffraction-limited at $\lambda = 100\,\mu$m. This section presents a more general technique for designing arrays of bolometers as a function of wavelength, substrate material, and of the throughput coupled through the optical system to a single pixel.

3.4.1 Detectivity scaling arguments

Many considerations enter the choice of the constant of proportionality N/Ω in (3.3) which relates A and λ^2. The optical filling factor is the ratio of the area of the infrared absorber to the area of the unit cell for a single pixel—which may include other components such as charge-storage capacitors or readout circuitry. For $\lambda = 10\,\mu$m, an acceptable filling factor of (50-60%) can be achieved[36] with $N/\Omega \approx 50$. Diffraction-limited pixels (N=1) with f/6 optics ($\Omega = 0.02\,$sr) and $A = 5 \times 10^{-5}$cm^2 preserve the filling factor (50-60%) and are useful at 10 μm for applications requiring high spatial resolution. Multi-mode pixels (N=10) with f/2 optics ($\Omega = 0.2\,$sr) also preserve this filling factor and are useful at

10μm for applications requiring high sensitivity when detector noise-limited. The specific detectivity $D^* = A^{1/2}/\mathrm{NEP}$ is convenient for comparing detectors with different areas.

Bolometers of the design in Fig. 3.3 made on thin Si_3N_4 membranes can have very low heat capacity per unit area C_A and can be made with very low G because of the mechanical strength and the low bulk thermal conductivity of Si_3N_4. The relatively high NET of our present thermometers on Si_3N_4, however, limits the use of this substrate to relatively small bolometers with high responsivity to minimize the contribution of film noise in (4). Such bolometers are well suited, for example, to imaging arrays for $\lambda \approx 10\mu$m. Bolometers made on Si membranes have smaller values of NET, but will probably be limited to larger values of C_A and G because of the thermal properties of Si. They are therefore appropriate for higher throughput applications at longer wavelengths. The very low values of NET obtained on thinned sapphire substrates make this technology appropriate for very large bolometers. We will quantify this argument by calculating the dependence of the detectivity D^* on area and thus on λ for each of the above technologies using the values of NET from Table 3.1.

The bolometer substrate technology chosen sets material limits to the heat capacity per unit area C_A that can be achieved. In addition, for the membrane technologies, there is a minimum practical value for the thermal conductance G_{min} set by the strength of the legs. The legs break if they are made longer and narrower to achieve $G < G_{\mathrm{min}}$ If we assume that the required response time τ and the factor $A/\lambda^2 = N/\Omega$ are set by the application, then the required $G = C_A A/\tau$ will be equal to G_{min} at a specific wavelength λ_o given by

$$\lambda_o = \left(\frac{G_{\mathrm{min}}\tau}{C_A}\frac{\Omega}{N}\right)^{1/2} . \tag{3.4}$$

For $\lambda < \lambda_o$, the bolometer will be faster than is required and therefore less sensitive than optimum. For $\lambda > \lambda_o$, the available range of G includes the optimum value.

We estimate C_A and G_{min} for a Si_3N_4 bolometer based on a 0.75 μm thick Si_3N_4 membrane which was built at Berkeley by other workers[49]. This membrane was supported by two Si_3N_4 legs with dimensions $0.75 \times 0.75 \times 20\,\mu$m. For a bolometer with two such legs, we calculate $G_{\mathrm{min}} \approx 0.3\,\mu\mathrm{W/K}$ by using a handbook value for the thermal conductivity of bulk Si_3N_4 at 90 K. For a Si membrane bolometer with two undoped Si legs of the same dimensions, $G_{\mathrm{min}} \approx 30\,\mu\mathrm{W/K}$. From handbook data,[24] we estimate that G_{min} of ion-implanted Si legs might be roughly $0.5G_{\mathrm{min}}$ of unimplanted Si legs at 90K. The reduction in G presumably arises from radiation damage of the Si. We expect the heat capacity of the

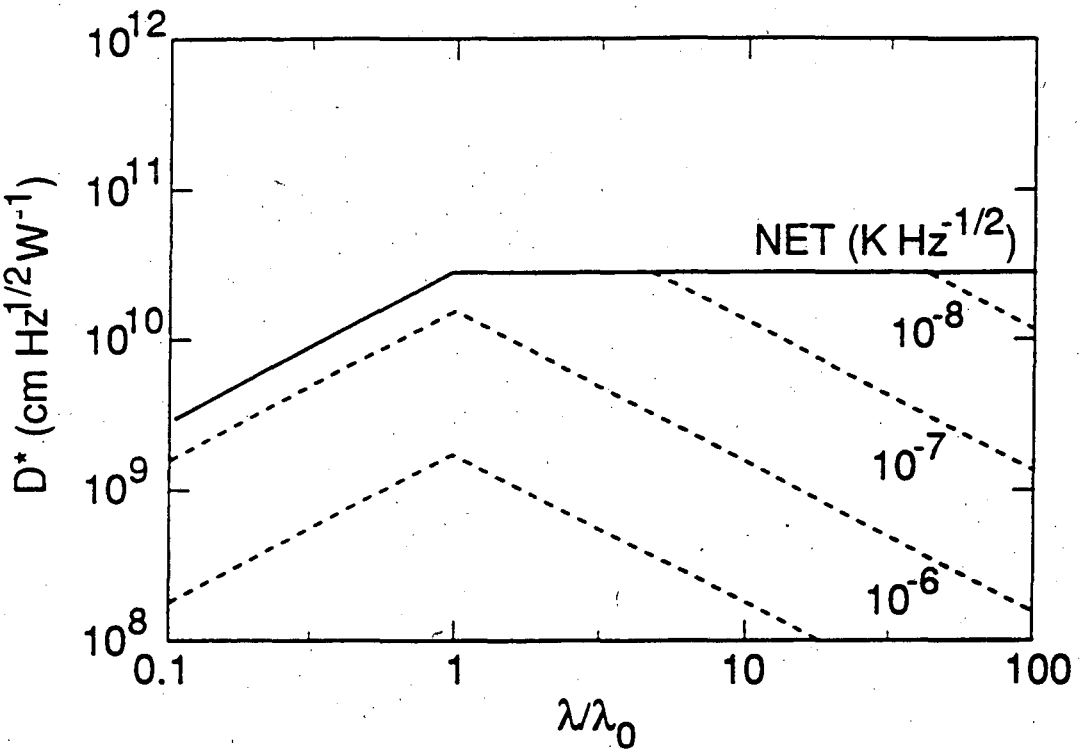

Figure 3.4: Specific detectivity D^* as a function of reduced wavelength λ/λ_o where λ_o depends on the minimum achievable values of the heat capacity per unit area C_A and thermal conductance $G_{\min}$ as well as the response time τ, the number N of electromagnetic modes which couple, and the solid angle Ω of the pixel's field of view. The solid line shows the predicted phonon noise limit for a bolometer on a thin membrane. The dashed lines show upper limits on D^* for thermometers with various values of NET.

YBCO thermometer and silver electrical contacts to dominate the substrate heat capacity, so we choose $C_A = 2.7 \times 10^{-5}\,\mathrm{J\,K^{-1}cm^{-2}}$ for both Si and Si_3N_4 membrane bolometers.

Figure 3.4 shows the prediction for D^* as a function of the normalized wavelength λ/λ_o for a fixed value of N/Ω and $\tau = 10\,\mathrm{ms}$. The solid line shows the upper limit on D^* imposed by phonon noise

$$D^* = \left(\frac{A}{4kT_c^2G}\right)^{1/2}. \tag{3.5}$$

For $\lambda > \lambda_o$, $G \propto A$, so $D^*(\lambda)$ is constant. For $\lambda < \lambda_o$, $G = G_{\min}$, so $D^*(\lambda) \propto A^{1/2} \propto \lambda$.

The performance of the bolometer is limited by thermometer noise if NET $> 10^{-8}\,\mathrm{K/Hz^{1/2}}$. The dashed lines show the limits on D^* from thermometer noise for various

values of NET calculated from (2.3) and

$$D^* = \left(\frac{A}{G^2(\mathrm{NET})^2(1+\omega^2\tau^2)} \right)^{1/2}. \tag{3.6}$$

For $\lambda > \lambda_o$, $G \propto A$, so $D^*(\lambda) \propto A^{-1/2} \propto 1/\lambda$. For $\lambda < \lambda_o$, G is held constant at $G_{\min}$ and $D^*(\lambda) \propto A^{1/2} \propto \lambda$. Hence D^* peaks at $\lambda = \lambda_o$ for a pixel limited by thermometer noise. The wavelength λ_o for Si_3N_4 is 0.1 of the value of λ_o for Si since the thermal conductivity of Si_3N_4 is $\sim 1/100$ that of Si at 90K.

3.4.2 Comparison of the detectivity to other technologies

For a given value of N/Ω, response time τ, and combination of YBCO thermometer and substrate, we can compute λ_o and plot the curve from Fig. 3.4 as D^* versus λ. Figure 3.5 shows this plot for $N/\Omega = 50$ and $\tau = 10$ ms for our best YBCO thermometer on both Si_3N_4 and Si membranes. For comparison, Fig. 3.5 also shows the performance of typical pixels in several different large format arrays operated at 77K along with the photon noise limits for photovoltaic and photoconductive detectors that view 300K radiation in a 0.02 sr field of view. The predicted performance for YBCO/YSZ/Si_3N_4, shown in Fig. 3.5, could be competitive with HgCdTe at $\lambda = 10\mu$m and one order of magnitude more sensitive than HgCdTe at $\lambda = 20\mu$m[50]. The performance of this array at longer wavelengths is better than room temperature detectors, but is rapidly degraded by thermometer noise. An array optimized for longer wavelengths can have a better peak value of D^*. Choosing $N/\Omega = 5$ and $\tau = 10$ ms, the peak in D^* is three times higher and occurs at $\lambda = 45\,\mu$m for the same thermometer NET.

The predicted performance for a YBCO/YSZ/Si bolometer with the same assumed geometry as for Si_3N_4 is also shown in Fig. 3.5. The region of phonon noise limited D^* appears at longer wavelengths than for Si_3N_4 because of the higher bulk thermal conductivity of silicon. The limit to D^* from thermometer noise is higher than that of bolometers on Si_3N_4 because of the lower NET of YBCO on silicon. Arrays of high-T_c bolometers on Si membranes may be useful for imaging applications for $\lambda > 20\mu$m. One example is long wavelength atmospheric imaging from NASA planetary probes such as Cassini[5].

The most important potential impact of the high-T_c bolometer is in a LN-cooled large format imaging array for $8-14\,\mu$m. This possibility depends both on the performance of the bolometer arrays as discussed above and also on the performance available from

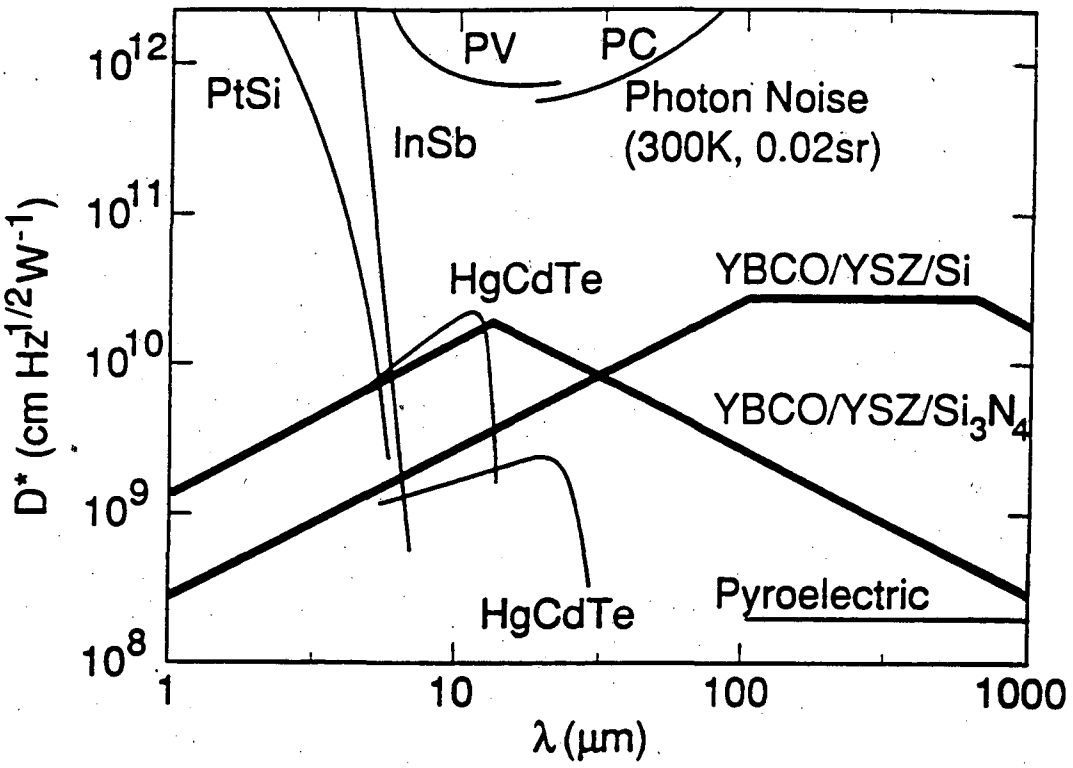

Figure 3.5: Specific detectivity D^* as a function of wavelength for diffraction-limited pixels with $\Omega = 0.02\,\mathrm{sr}$ (f/6 optics) and $\tau = 10\,\mathrm{ms}$. The thick lines show the predicted D^* for high-T_c bolometers on silicon and Si_3N_4 membranes using YBCO thermometers. These lines were calculated using estimates for the minimum achievable heat capacity and thermal conductance and using measurements of voltage noise in high-T_c thermometers. Typical values of D^* for InSb, PtSi, and HgCdTe detectors in two dimensional staring arrays operated at 77K are shown for comparison. Also shown are the photon noise limits for photovoltaic and photoconductive detectors which view 300K radiation in a 0.02 sr field of view.

the competing HgCdTe technology. Although accurate predictions are not possible, this important question deserves further discussion. Two dimensional (2D) staring arrays for 300K thermal imaging in the atmospheric window from $8-14\,\mu$m require high D^* per pixel, good uniformity, and low-noise readout electronics. The predicted D^* of a high-T_c bolometer used from $8-14\,\mu$m is worse than the D^* of a HgCdTe photovoltaic detector in a single pixel or linear array format. However, it is difficult to make 2D arrays of HgCdTe photovoltaic detectors which are larger than 128×128 pixels[51]. Even these arrays suffer from low yields and high costs. The performance of arrays of HgCdTe detectors which operate from $8-14\,\mu$m also suffers from high backgrounds and high leakage currents. These currents rapidly saturate the charge storage capacity of a CCD readout and can restrict the integration time of the signal[51, 52]. Many thermal imaging systems which require high spatial resolution across the field of view operate at shorter wavelengths so as to use more mature technologies[53] with larger numbers of pixels such as PtSi[54] or InSb. Although the yield and uniformity of such arrays are excellent, the atmosphere is more opaque at these wavelengths. Also, radiation from a 300K black body is weaker at 4μm than at 10μm but stray light from visible sources such as the sun is stronger at 4μm than at 10μm. We believe large 2D arrays of high T_c bolometers on Si_3N_4 membranes will have useful sensitivity from $8-14\,\mu$m and could have advantages in yield and cost over large 2D arrays of HgCdTe. Without building such an array, we can not quantitatively predict the uniformity of the responsivities of pixels across the array. Equation (1.1) shows the uniformity in S depends only on variations in I, G, and $dR(T)/dT$. Temperature gradients across the array could produce variations in $dR(T)/dT$ from pixel to pixel. But, temperature gradients which are smaller than $\sim 0.1R(dR/dT)^{-1}$ should not seriously degrade uniformity since $R(T)$ is mostly linear on this temperature scale.

3.5 Electronic readout for bolometer arrays

We have predicted useful sensitivity for a single pixel high-T_c bolometer with a dedicated low-frequency amplifier. Many imaging applications require large arrays of bolometers where constraints on power dissipation and filling factor only allow for a small number of amplifier channels. In simple circuits, the electrical signal from a pixel is only integrated for a tiny fraction of the observation time. The electrical noise from a pixel in an array can therefore be much greater than the noise from a single pixel with a dedicated am-

plifier. We now discuss a scheme which provides signal integration over the full observation time, but does not require one amplifier per pixel.

The NEP of a bolometer pixel has contributions from thermal fluctuations, including infrared source fluctuations, as well as the phonon noise, represented by the first term in (1.2). It also has contributions from voltage fluctuations in the thermometer, represented by the second and third terms in (1.2). Thermal fluctuations occurring for $\omega_{\rm fluct}\tau \gg 1$ are integrated by the thermal response time of the bolometer. Therefore, a bolometer which operates in the source noise or phonon noise limit with τ equal to the frame time does not require additional electrical integration. In principle, however, a bolometer optimized for sensitivity has equal contributions to the NEP from both thermal fluctuations and voltage fluctuations. In practice, the bolometer designs that we have described above are sometimes limited by voltage noise fluctuations. Therefore, integration of the electrical signal is desirable.

Photovoltaic detectors in a CCD array integrate the photocurrent with a charge storage well next to each detector. Ideally, the storage capacity of the well is larger than the product of the photocurrent and the time interval between samplings by the readout amplifier. Consequently, charge fluctuations which occur faster than the sampling rate are averaged. A bolometric detector outputs a voltage equal to the product of the absorbed infrared power and the responsivity (1.1). An RC filter could be implemented next to the bolometer which integrates voltage fluctuations occurring on time scales shorter than RC. The RC time should approximately equal the frame time.

As a specific example, we consider a 64 x 64 imaging array of high-T_c bolometers similar to existing arrays of bismuth bolometers built at Honeywell[36]. Since both the readout amplifiers and the bolometers have 1/f noise, we assume the incident radiation is chopped at 60 Hz. This leads to a frame rate of 30 Hz and a thermal time constant $\tau = 3$ ms for each bolometer pixel. The pixels are continuously biased and dissipate less than 5μW each. The whole array is read out once while observing the target, and again while observing the chopper blade. The two frames are then digitally subtracted. Assuming four readout amplifiers, each pixel is sampled for a maximum time $\tau_{\rm sample} = 3\,\mu$sec. Electrical noise in the thermometer occurring at higher frequencies than 60 Hz is then aliased across the bandwidth of the readout amplifier. An RC filter next to each pixel would roll off this high frequency noise before it is aliased.

Figure 3.6 shows a schematic implementation of the readout circuit for a two

dimensional bolometer array. The readout circuit elements could be fabricated on a separate silicon wafer which is bonded to the bolometer array with indium bumps. The R_fC filter appears in parallel with the high-T_c thermometer. For conceptual simplicity, we will first consider passive circuit components. In practice, circuits with active components may consume less power and surface area. Active components are frequently used in CCD arrays[55, 56]. A polysilicon resistor with $R_f = 10\,\mathrm{M}\Omega$ and a trench capacitor with $C =$ 300pF would give a time constant $R_fC = 3\,\mathrm{ms}$. Typically, $R_f \gg R$ so the contribution to the NEP from Johnson noise is mostly from R_f. This contribution will be negligible if the constraint (3.2) is modified to

$$I\delta R > \left[4kT_cR_f + \frac{e_n^2 + (i_nR_f)^2}{f_{\mathrm{chop}}\tau_{\mathrm{sample}}}\right]^{1/2} . \tag{3.7}$$

The divisor $f_{\mathrm{chop}}\tau_{\mathrm{sample}}$ accounts for the reduced integration time of noise from the readout amplifier. The resulting amplifier noise contribution to the NEP is negligible for available amplifiers[57]. For example, a bolometer on a Si_3N_4 membrane using sample C could satisfy conditions (3.7) and the thermal stability condition for $R_f = 10\mathrm{M}\Omega$ and the array parameters described above if the YBCO is patterned into a meander line with $R = 50\mathrm{k}\Omega$ at T_c.

It may be difficult to satisfy (3.7) as well as the condition for thermal stability using only passive components because of size constraints on the capacitors and difficulty in making high resistance meander strips of YBCO. Although exact requirements on the anti-aliasing filter are specific to the system, we will mention two approaches which address these potential problems. First, the R_fC time constant could be reduced by reading out the array more frequently. For example, most of the signal integration could be performed by a bank of larger capacitors called a frame averager which is located outside the focal plane. In this scheme, multiplexers transfer charge from a small capacitor next to a pixel to a much larger capacitor out of the focal plane at a faster rate than the chopping frequency. Then the readout amplifier samples the capacitors in the frame averager at the chopping frequency. Second, two-transistor amplifiers with anti-aliasing filters could be fabricated in silicon for each pixel. Figure 3.7 shows a schematic diagram of a circuit which is functionally similar to Fig. 3.6 but which uses active components. The depletion-mode transistor T1 presents a current bias to the bolometer without dissipating much power. The depletion-mode transistor T2 functions both as R_f for the anti-aliasing filter and as a load resistance for the common source buffer stage made from T3. This circuit has both an anti-aliasing

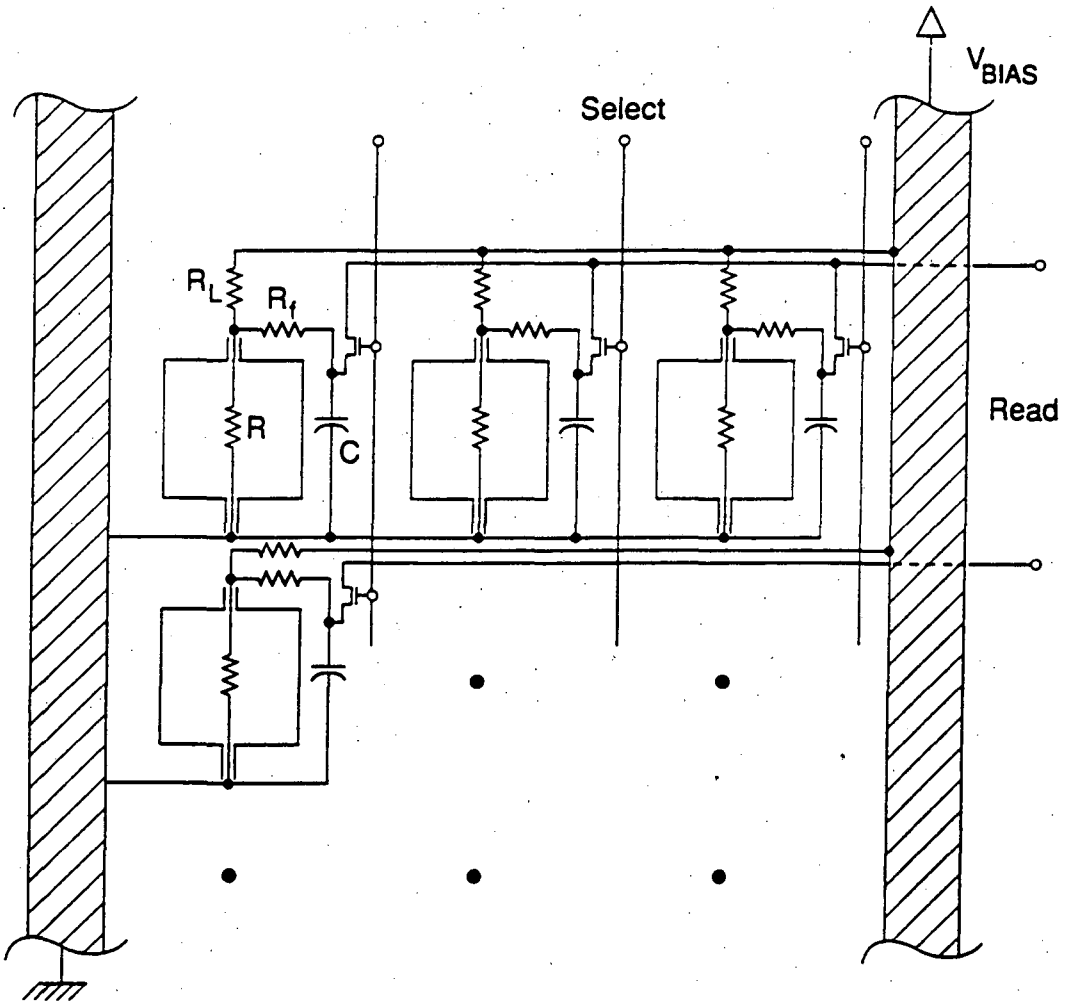

Figure 3.6: Schematic layout of a possible implementation of a high T_c bolometer array with a novel readout scheme in which above-band electrical noise from each pixel is integrated by an R_fC filter. In this scheme, a multiplexed readout amplifier which undersamples a given pixel does not alias above-band noise into the signal channel. The unit cell consists of a YBCO thermometer R, an R_fC filter, an access transistor, a load resistor R_L, and bias lines. The voltage across R appears on the appropriate "READ" line when the "SELECT" voltage is high. All pixels are constantly under bias. The readout circuit elements would be implemented on a separate Si wafer which could be indium bump-bonded to the bolometer pixels. The optical fill factor will probably be limited by geometrical constraints on the bolometer imposed by requirements for thermal isolation.

filter and voltage gain to buffer the signal from noise in the "Select" transistor. If a specific application requires a higher resistance from the active load, a current mirror could be used in place of the depletion-mode transistor[58]. The transistors can be MOSFETs in most applications. Some applications may benefit from the lower 1/f noise of JFETs.

3.6 Thermal imaging applications

Some of the membrane bolometer designs developed above could be used in thermal imaging arrays which operate in the atmospheric window from $8 - 12\,\mu$m. There is a substantial commercial market for infrared imagers. They are produced by more than eight different companies for applications as diverse as studies of the thermal efficiency of buildings, the diagnosis of malfunctions in machinery and electronic circuits, security systems, the detection of clear air turbulence for aircraft, and the detection of cancer in humans. Most of this work is done near $3\,\mu$m wavelengths because of the availability of suitable detector arrays of InSb or PtSi. Much of this work would benefit from cost-effective detectors operating from $8 - 12\,\mu$m. A demonstration of a high-T_c bolometer with a cost or sensitivity advantage over existing thermal imaging detectors would be a major development.

3.7 Summary

In this chapter, we have discussed the optimization of high-T_c bolometers for imaging arrays for wavelengths longer than $10\,\mu$m. An analysis of the thermometer sensitivity required for different pixel sizes indicates that there are useful applications for small Si_3N_4 membrane bolometers at $\lambda \sim 10\,\mu$m and larger Si membrane bolometers at longer wavelengths. A readout scheme for an array of bolometers which provides real-time signal integration on chip has also been described. There may be applications for arrays of high-T_c bolometers for thermal imaging.

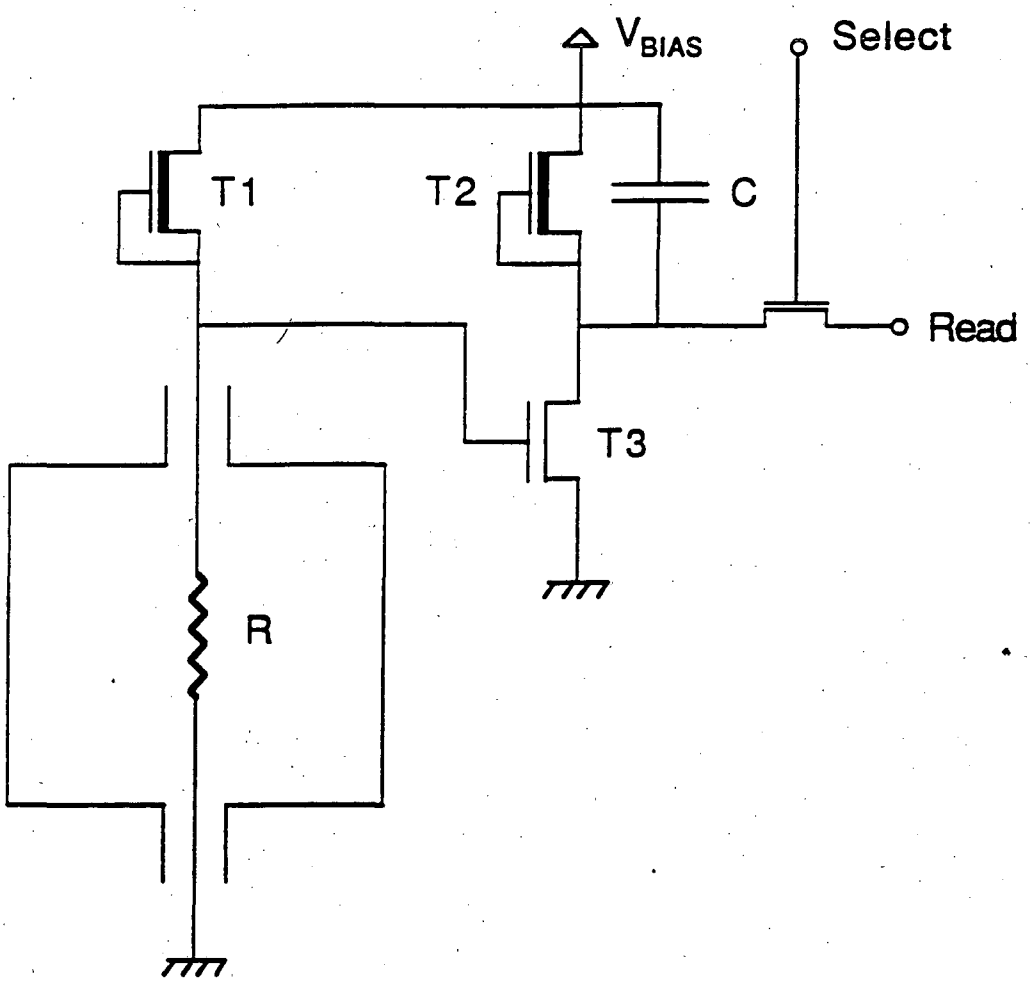

Figure 3.7: Schematic layout of a readout for a single pixel which is functionally similar to a single cell in Fig. 3.6 but uses active devices. This circuit has both an anti-aliasing filter and voltage gain to buffer the signal from noise in the "Select" transistor. The power consumption and size of this circuit can be much smaller than the circuit shown in Fig. 3.6.

Chapter 4

Nonisothermal High-T_c Bolometers

The high-T_c composite bolometers described in Chapters 2 and 3 are built from individual components which function as the radiation absorber, thermometer, substrate, and thermal link to the heat sink. At $T = 90\,\mathrm{K}$, the bolometer substrate is effectively isothermal and is the dominant contribution to the heat capacity. The thermal links are copper electrical leads for the sapphire bolometer or micromachined legs for the Si or Si_3N_4 membrane bolometers. The thermal link accounts for most of the temperature drop between the thermometer and the heat sink and is the dominant contribution to the thermal conductance. An equivalent circuit which consists of lumped elements accurately models the thermal response of these bolometers. Composite bolometers can be designed for a variety of applications since their individual components can be optimized independently. For applications such as Fourier transform spectrometers, the thermal conductance G and heat capacity C are usually adjusted so that the bolometer operates in the limit $\omega_c\tau < 1$. Here $\tau = C/G$ is the thermal time constant and $\omega_c/2\pi = 2v_{\mathrm{mirror}}/\lambda_c$ is the highest frequency at which interference fringes appear on the bolometer, where v_{mirror} is the mirror velocity and λ_c is the shortest wavelength to be measured. In the limit $\omega_c\tau < 1$, the bolometer responsivity (1.1) is independent of the fringe frequency for $\omega < \omega_c$.

There are applications for bolometers where some of the components serve multiple functions. This chapter discusses the design of nonisothermal bolometers on yttria-stabilized zirconia (YSZ) membranes for spectrometer applications. Such a bolometer consists of a

YBCO film of thickness ~ 40 nm deposited on a YSZ membrane of area 1 mm^2 and thickness 0.5 μm. The membrane is etched from a YSZ coated silicon wafer. Figure 4.1 shows a schematic diagram of such a bolometer. The membrane is heat-sunk along its perimeter and serves as both the bolometer substrate and as the thermal link. The YBCO film serves as both the thermometer and as the radiation absorber. The thermal response of the membrane bolometer can be analyzed with a continuum of distributed elements. Such a calculation gives effective values for $C_{\rm eff}$ and $G_{\rm eff}$ which are useful for comparing the performance of a membrane bolometer to the performance of a lumped-element, composite bolometer. The quantities $C_{\rm eff}$ and $G_{\rm eff}$ for the membrane bolometer are interdependent and are difficult to optimize independently. The membrane bolometer cannot be optimized for as many applications as a lumped-element bolometer such as the composite sapphire bolometer discussed in Chapter 2. For the application of Fourier-transform spectrometers, however, the membrane bolometer may be more manufacturable because of its simple geometry and it may be more sensitive because of its reduced heat capacity.

4.1 Fabrication considerations

4.1.1 Substrate material

Yttria-stabilized zirconia (YSZ) is a favorable substrate material because of its low thermal conductivity and its compatibility with YBCO. The fabrication of YSZ membranes is well-suited to micro-machining techniques such as those used with silicon nitride membranes. Films of YSZ have adequate fracture toughness to be made into membranes of submicron thickness. The process we used for fabricating YSZ membranes can be described as follows. First, a $1 \times 1 \times 0.05$ cm wafer of silicon with {100} orientation was coated with a 1 μm thick film of Si_3N_4. We then etched the Si_3N_4 off the polished side (front) of the wafer and patterned holes in the Si_3N_4 on the back of the wafer. The wafer was transferred to a laser-ablation chamber where 0.5 μm of YSZ was deposited on the front side[45]. The wafer is then etched in a 80° C solution of 750 g solid KOH dissolved in 1500 ml of water. The KOH solution etches silicon anisotropically but does not noticeably etch the YSZ film. The YSZ film functions as its own etch-stop.

This fabrication process is complicated by the need for a YBCO film of high quality on the YSZ membrane. The YBCO must be deposited on the YSZ film before the underlying

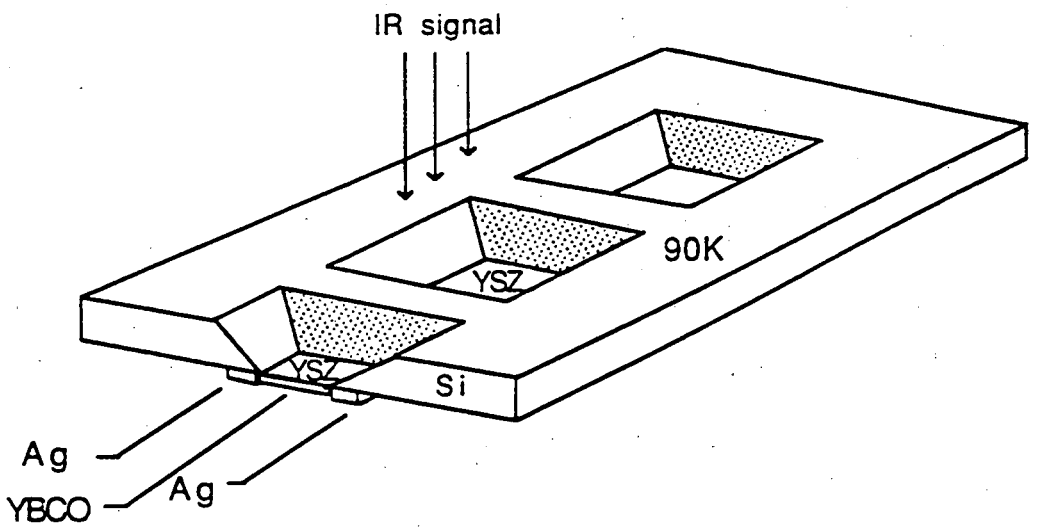

Figure 4.1: Diagram of three membrane bolometers. Each bolometer consists of a YBCO film which functions as the radiation absorber and as the thermometer. The YSZ membrane is in contact with the heat sink along its perimeter. Radiation is incident on the bolometer from the top side and is partially collected by the 54° facets in the silicon which are produced by the anisotropic Si etch.

silicon is etched because of the difficulty in uniformly maintaining the YSZ membrane at 700° C during deposition of YBCO. The YBCO film must then be protected from the KOH solution during etching. We have built an apparatus for etching YSZ membranes from samples which are already coated with YBCO. It consists of a 5-sided box of teflon. A teflon flange holds the silicon chip as the sixth side. The edges of the chip are protected by the flange and the KOH solution only etches the silicon through the patterned holes in the Si_3N_4. The inside of the box is filled with water and contains a red LED. The enclosure is sealed with silicone cement and is placed in the etchant until a photodiode detects red light from the LED transmitting through the thin YSZ membrane. We have produced YSZ membranes of 0.4 μm thickness with areas up to 3 mm^2 using this technique.

4.1.2 Infrared absorber

In earlier work on sapphire composite bolometers, we used a gold black absorber for wavelengths from 0.5 – 50 μm and a resistive bismuth film from 50 – 1000 μm [4]. A 30 nm Bi film deposited on the back of the YSZ bolometer would have a surface resistance

$R_s \approx 150\Omega$ and could absorb $\sim 50\%$ of the radiation incident through the YSZ substrate [2]. Such a metal film must be much thinner than the skin depth and must have a quasiparticle scattering rate which is higher than the frequency of the photons to be absorbed. An alternative scheme is to use a YBCO film on the front of the bolometer as the absorber of infrared radiation incident from the back. This could be the same YBCO film used for the thermometer. We use data from Gao *et al.* on the infrared conductivity [59] of a 48 nm thick YBCO film measured near T_c to estimate the absorption efficiency of a YBCO absorber. We assume that radiation is incident normally on the back side of the YSZ membrane (the side not coated with YBCO) and that the YSZ and YBCO films are infinite in area. We also assume the thickness t of the YBCO film is much thinner that the skin depth and that the infrared sheet resistance is $R_s \approx (\sigma_1 t)^{-1}$. From the conductivity data of Gao *et al.*, a 20 nm thick film of YBCO would have a value of R_s which monotonically decreases from $250\,\Omega$ to $110\,\Omega$ for wavelengths of $30 - 100\,\mu$m respectively. We assume the dielectric constant of YSZ[60] to be $\epsilon = 12.5$ and use the equations derived by Clarke *et al.*[2] to calculate the power absorbed by the bolometer. Although these equations are derived for radiation of normal incidence, Clarke *et al.* argue they are accurate to within a few percent for angles of incidence up to 60°. For wavelengths from $30 - 100\,\mu$m, we calculate that the YBCO film absorbs between $46 - 49\%$ of the incident radiation. Such an absorption efficiency is competitive with the resistive metal film absorbers used on composite bolometers.

The geometry of the YBCO film may also be favorable for use as the thermometer. A square of YBCO film of 20 nm thickness with resistivity $\rho_n = 200\,\mu\Omega - \text{cm}$ would have a DC resistance of $100\,\Omega$. A DC resistance $> 100\,\Omega$ is required for adequate coupling to a readout amplifier. As we discussed in Section 3.2, the voltage noise in YBCO films tends to increase when they are patterned into small volumes. The YBCO film for the YSZ bolometer covers essentially the entire area of the membrane and may help to avoid this problem.

4.1.3 Electronic read-out circuit

Amplifiers which have noise temperatures lower than 90K for a $100\,\Omega$ source resistance are not readily available. An FET amplifier coupled through a transformer has excellent performance $T_N < 1\,\text{K}$ but is bulky and undesirable for commercial applications. We have built instrumentation amplifiers based on LT1028 operational amplifiers made by

Linear Technologies Corp. which use a bipolar input stage and have a noise temperature of 180K for a 200 Ω source impedance. All of the YBCO thermometers we have measured to date show electrical noise at least two times higher than Johnson noise. Therefore, such amplifiers are currently adequate for the best YBCO thermometers.

Bolometers are usually operated as square-law detectors so that the output signal depends linearly on the absorbed power. The maximum power that the membrane bolometer can absorb and respond to linearly is that power which does not produce temperature gradients $> \delta T$ across the membrane. Here δT is the width of the part of the resistive transition where $dR_A/dT = const.$ The maximum AC component of the power is therefore $P_{\max} = \eta A\Omega(G + i\omega C)\delta T$, where η is the optical efficiency. The dynamic range of a bolometer is the ratio of the maximum power which does not saturate the bolometer to the minimum detectable power in a 1 Hz noise bandwidth. The minimum detectable power in a 1 Hz bandwidth is $P_{\min} = \eta A\Omega(\mathrm{NEP})$. Assume that the contributions to the NEP in (1.2) from amplifier noise and from photon noise are negligible. Then thermometer noise and thermal fluctuation noise are the largest contributors to $P_{\min}$. Consider the limits when either thermometer noise or thermal fluctuations dominate. The ratio of $P_{\max}$ to $P_{\min}$ gives the dynamic range

$$D.R. = \frac{(G + i\omega C)}{\mathrm{NEP}} \approx \begin{cases} \delta T/\mathrm{NET}\,, & \text{thermometer noise limit.} \\ \frac{(G+i\omega C)\delta T}{(4kT^2G)^{1/2}}\,, & \text{thermal fluctuations limit.} \end{cases} \tag{4.1}$$

In the limit imposed by thermometer noise, the dynamic range is independent of the thermal parameters of the bolometer. In the limit of thermal fluctuations, the dynamic range depends on G.

In order to adjust the maximum power $P_{\max}$, the bolometer can be operated in a thermal feedback circuit in which the bolometer is kept at constant temperature by feeding back a heater current which cancels the temperature changes induced by the incident infrared signal. The feedback current then carries the signal information. Figure 4.2 shows such a circuit which is qualitatively similar to the flux-locked loop circuit used to read out SQUID magnetometers. This circuit is easily analyzed in the regime $\omega\tau < 1$. The AC signal voltage V_{sig} from the thermometer is fed back to a heater on the bolometer through a voltage-to-current converter such that $\delta I = gV_{\mathrm{sig}}$, where g is the programmable conductance of the voltage-to-current converter. A DC current I is added to the feedback current δI in a summing amplifier which drives the secondary heater. To lowest order in δI, the heater

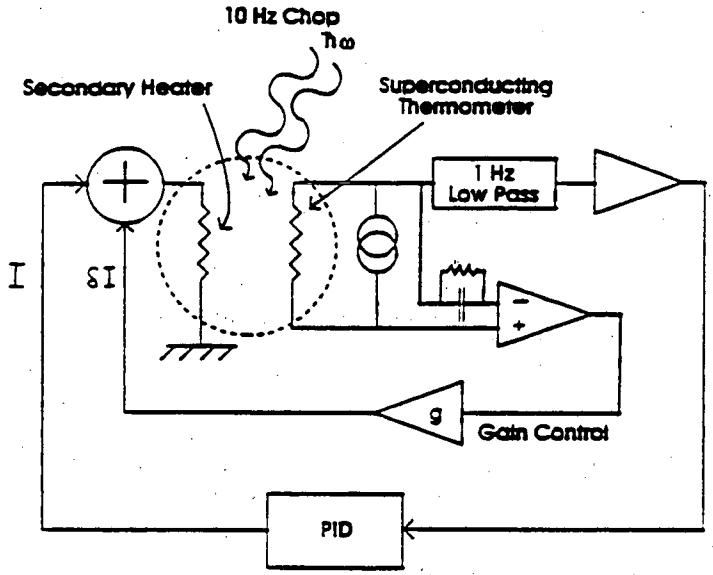

Figure 4.2: Feedback circuit for adjusting the operating range in infrared power of the bolometer.

power dissipated in the bolometer is

$$(I + \delta I)^2 R_h = I^2 R_h + 2I\,\delta I R_h + \ldots, \tag{4.2}$$

where R_h is the heater resistance. Equation (4.2) can be solved for V_{sig} and written as a voltage responsivity

$$S(\omega) = \frac{I dR/dT}{G\,(1 + 2g(IR_h/G)(dR/dT))}, \tag{4.3}$$

with a loop gain $A = 2g(IR_h/G)(dR/dT)$. When A is reduced to zero, Eq. (4.3) is the same as the responsivity (1.1) derived in the first chapter. This feedback circuit allows adjustment of the bolometer responsivity through the loop gain A. Adjusting the quantity $(1 + A)$ is functionally equivalent to adjusting the thermal conductance G of the bolometer. The thermal conductance cannot be reduced below $P_o/(90 - 77)$K, where P_o is the infrared power which loads the bolometer. A bolometer with its NEP limited by voltage noise fluctuations can operate at a higher maximum power—from the background and from the modulated signal—before it saturates if A is increased so that $(1+A) > 1$. The NEP of such a bolometer is degraded in proportion and the dynamic range is unchanged. A bolometer with its NEP limited by thermal fluctuations can have its dynamic range increased in proportion to $\sqrt{1 + A}$. Hence, the circuit provides an electronically tunable G which allows a bolometer to operate in a variety of infrared loading conditions.

The RC network in series with the preamplifier has a time constant equal to the thermal time constant of the bolometer. This acts as a zero which cancels the pole in the frequency-dependent response of the bolometer. At the output of the preamplifier, the response of the bolometer is independent of frequency even when $\omega\tau > 1$. The responsivity of the bolometer may be slightly enhanced by operating with positive feedback $(1+A) < 1$. This could make a bolometer limited by voltage fluctuations more sensitive as long as the feedback circuit remains stable. It may be difficult to enhance the sensitivity by more than a factor of two and keep the thermal circuit stable.

4.2 Thermal analysis and estimate of the NEP

This section presents an analysis of the membrane bolometer in terms of distributed elements. A comparison of the distributed-element solution with the response of a lumped-element bolometer shows that equivalent thermal parameters $C_{\rm eff}$ and $G_{\rm eff}$ exist for the membrane bolometer. The contributions to the minimum NEP from thermal fluctuations and thermometer noise can then be calculated.

There are many conceivable geometries for a membrane bolometer. A square or rectangular geometry is the most practical to fabricate given the properties of the anisotropic etch of silicon. For the square bolometer shown in Fig. 4.1, radiation is incident on the bolometer from the top side and is partially collected by the 54° facets in the silicon which are produced by the anisotropic etchant. Our goal is a qualitative understanding of the thermal response of nonisothermal membrane bolometers. For simplicity, we choose a circular geometry which has only one spatial coordinate. Consider a disc-shaped membrane of YSZ with radius a with the perimeter in thermal contact with the silicon substrate which functions as a heat sink. The equation which governs heat transfer[61] can be written as

$$\nabla^2 T - \frac{c_p}{\kappa}\partial_t T = \frac{\rho}{\kappa}, \tag{4.4}$$

where T is the temperature, c_p and κ are the specific heat and thermal conductivity of the membrane material respectively, and ρ is the amount of power absorbed per unit volume. This equation describes diffusive heat flow and implicitly assumes the speed of sound is much greater than $\omega a/2\pi$ where $\omega/2\pi$ is the highest frequency at which the incident radiation is modulated and a is the radius of the membrane. If the speed of sound in YSZ is 5×10^5 cm/s, the heat flow in a 1 mm diameter membrane is no longer diffusive at frequencies above

$\sim 5\,\mathrm{MHz}$. There are no solutions of (4.4) which describe propagating waves of heat flow[62].

Assume uniform absorption of infrared radiation occurs across the membrane and neglect any effects from ohmic heating of the thermometer. If the thermometer noise arises from resistance fluctuations, the optimum bias current I in (3.2) is that which makes voltage fluctuations in the thermometer larger than the amplifier noise. If $I^2 dR/dT \ll G_{\mathrm{eff}}$, then ohmic heating can be neglected. For simplicity, the temperature T is measured relative to the temperature of the heat sink. The perimeter of the membrane is in contact with the heat sink and leads to the boundary condition $T(r = a, \omega) = 0$. We assume the incident power has the form $\rho = \rho_o(1 + \cos(\omega t))$. Since (4.4) is linear in T, the temperature of the membrane will have the form $T(r,t) = T_0(r,0) + T_1(r,\omega)\exp(-i\omega t)$. Integrating (4.4) with $\omega/2\pi = 0$ gives a solution for $T_0(r,0)$.

$$T_0(r,0) = \frac{\rho_o}{4\kappa}\left(a^2 - r^2\right) . \tag{4.5}$$

A solution of (4.4) for nonzero values of ω is

$$T_1(r,\omega) = \frac{\rho_o}{i\omega c_p}\left(\frac{J_0\left[\sqrt{\frac{\omega c_p}{2\kappa}}(1+i)r\right]}{J_0\left[\sqrt{\frac{\omega c_p}{2\kappa}}(1+i)a\right]} - 1\right) . \tag{4.6}$$

The Bessel function $J_0[(1+i)x]$ has a complex argument and is referred to as either a Kelvin function or a Farmyard function in microwave handbooks. It is used to calculate wave propagation in lossy coaxial transmission lines.

Inspection of (4.6) suggests there is a characteristic relaxation time for a circular membrane

$$\tau_r = a^2 c_p/\kappa . \tag{4.7}$$

This is roughly the time for a circular membrane to approach a steady state temperature distribution if constant power suddenly illuminates the membrane and is uniformly absorbed across the entire area. Table 4.1 shows the thermal conductivity, specific heat, and relaxation time for membranes of Si, Si_3N_4, and YSZ with radius $a = 0.5\,\mathrm{mm}$. A nonisothermal bolometer can have a value of τ_r which can be varied by a factor of 500 by making an appropriate choice of membrane material.

Figure 4.3 shows plots of $T_1(0,\omega)$ computed from (4.6) for four values of $\omega\tau_r$ for a YSZ membrane of thickness $0.5\,\mu\mathrm{m}$ and radius 0.5 mm. The incident power is $1\,\mu\mathrm{W}$. For $\omega\tau_r = 0$, the temperature decreases quadratically with distance from the center of the

Material	κ (W/cm K)	c_p (J/cm^3 K)	$\tau_r = a^2 c_p/\kappa$ (ms)
Si	5.5	0.53	0.24
Si_3N_4	0.056	0.31	14
YSZ	0.015	0.72	120

Table 4.1: Thermal properties of materials at 90 K for nonisothermal membrane bolometers of radius $a = 0.05$ cm.

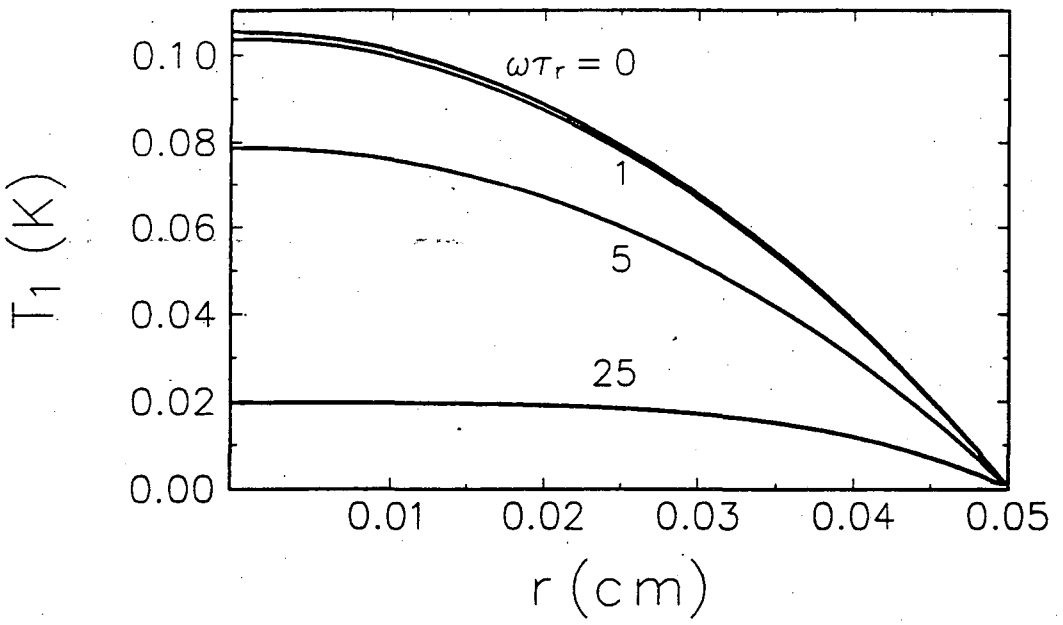

Figure 4.3: Plots of (4.6) as a function of radial distance from the center of the membrane computed numerically for three values of $\omega\tau_r$. At frequencies $\omega\tau_r \gg 1$, most of the central region responds isothermally at ω and a temperature gradient appears along the perimeter of the membrane.

membrane, as predicted by (4.5). For $\omega\tau_r = 1$, the AC component $T_1(r,\omega)$ has a shape which is similar to the curve for $\omega\tau_r = 0$. As $\omega\tau_r$ is increased until $\omega\tau_r \gg 1$, most of the central region responds isothermally at ω and a temperature gradient appears along the perimeter. In this regime the temperature in the central region oscillates in response to the modulated incident power, however, the amplitude of oscillation is reduced and is out of phase since the edge of the membrane is farther away than a thermal diffusion length $a > l_{\text{thermal}} \equiv \sqrt{2\kappa/\omega c_p}$.

It is instructive to examine the limiting forms of (4.6) at the center of the membrane for small and large values of $\omega\tau_r$. The contribution from (4.6) to the temperature at the center of the membrane is

$$T_1(0,\omega) = \frac{\rho_o}{i\omega c_p}\left(J_0\left[\sqrt{\omega\tau_r}\right]^{-1} - 1\right). \tag{4.8}$$

Figure 4.4a shows the oscillating component of the temperature at the center of the membrane $T_1(0,\omega)$ plotted as a function of $\omega\tau_r$. For $\omega\tau_r < 1$, the response at the center of the membrane is independent of frequency. For $\omega\tau_r \gg 1$, the response decreases in proportion to ω^{-1}. In these limits for $\omega\tau_r$, the Kelvin function in (4.8) can be approximated using series expansions. The terms of lowest-order give analytical expressions for the effective thermal parameters C_{eff} and G_{eff} of the membrane bolometer.

For $x \ll 1$, $J_0[(1+i)x]$ is [63]

$$J_0[(1+i)x] = \left[1 - \frac{(x/2)^4}{(2!)^2} + \frac{(x/2)^8}{(4!)^2} - \ldots\right] + i\left[(x/2)^2 - \frac{(x/2)^6}{(3!)^2} + \frac{(x/2)^{10}}{(5!)^2} - \ldots\right]. \tag{4.9}$$

Substitution of (4.9) into (4.8) gives a limiting form which is the same as the DC solution (4.5). Therefore, to within an error $O[(\omega\tau_r)^2]$, the temperature at the center of the membrane is

$$T_1(0,\omega) \approx \frac{\rho_o a^2}{4\kappa}, \quad \omega\tau_r \ll 1. \tag{4.10}$$

For $x \gg 1$, the asymptotic form for $J_0[(1+i)x]$ is

$$J_0[(1+i)x] = \frac{\exp(\beta)}{\sqrt{2\pi x}}\cos(\alpha) + i\frac{\exp(\beta)}{\sqrt{2\pi x}}\sin(\alpha), \tag{4.11}$$

where $\alpha = x/\sqrt{2} - \pi/8 - 1/8\sqrt{2x} - \ldots$ and $\beta = x/\sqrt{2} + 1/8\sqrt{2x} - \ldots$. Substituting this expression into (4.8) gives

$$T_1(0,\omega) \approx \frac{\rho_o}{i\omega c_p}, \quad \omega\tau_r \gg 1. \tag{4.12}$$

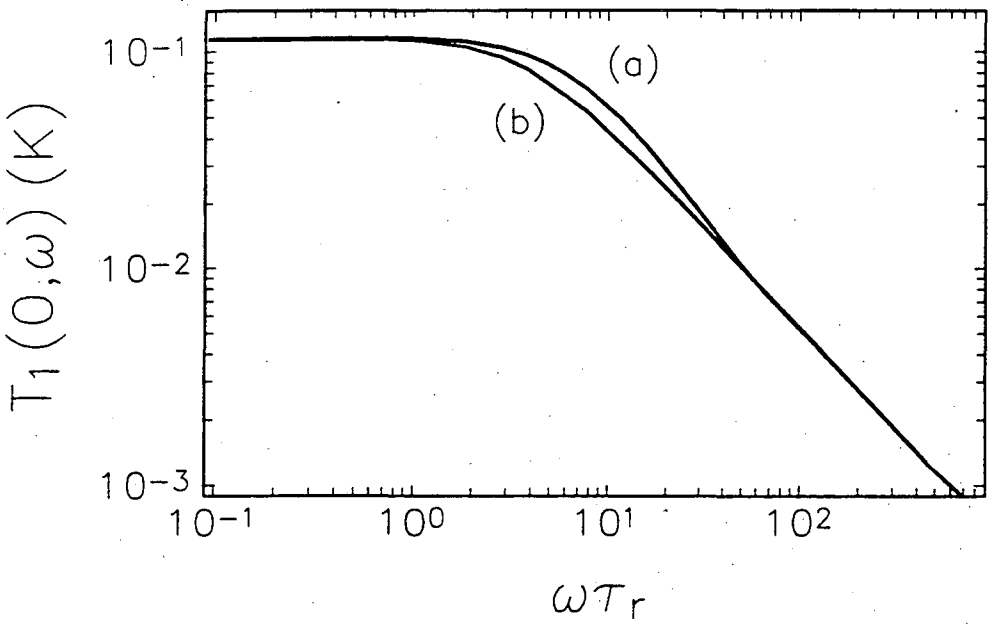

Figure 4.4: (a) The oscillating component of the temperature at the center of the membrane $T_1(0,\omega)$ plotted as a function of $\omega\tau_r$. (b) Plot of the single-pole response of a composite bolometer.

This is the same frequency dependence as for a lumped-element bolometer operating in the regime $\omega\tau_r > 1$.

We can compare the response of the membrane bolometer to the response of a lumped-element bolometer as follows. If the numerator and denominator of (4.10) and (4.12) are multiplied by the volume of the membrane Ω, the temperature oscillation at the center of the membrane can be compared to a single-pole response

$$T_1(0,\omega) \approx \frac{\rho_o \Omega}{G_{\rm eff} + i\omega C_{\rm eff}}, \tag{4.13}$$

where

$$\begin{aligned} C_{\rm eff} &= c_p \Omega, \\ G_{\rm eff} &= 4\pi\kappa t_{\rm YSZ}, \\ \tau_{\rm eff} &\equiv C_{\rm eff}/G_{\rm eff} = 0.25\tau_r, \end{aligned} \tag{4.14}$$

and $t_{\rm YSZ}$ is the thickness of the YSZ membrane. Figure 4.4b shows (4.13) plotted as a function of $\omega\tau_r$. The similarity of the two curves in Fig. 4.4 shows that (4.13) provides a useful

intuitive picture for designing nonisothermal membrane bolometers. If the thermometer only measures the temperature at the center of the membrane, the membrane bolometer behaves like a lumped-element bolometer with effective thermal parameters given by (4.14) when operated in the regime $\omega\tau_{\rm eff} \ll 1$ or $\omega\tau_{\rm eff} \gg 1$. The two types of bolometer have different behaviors in the regime $\omega\tau_{\rm eff} \approx 1$. With these effective thermal parameters, one can estimate the sensitivity of the YSZ membrane bolometer using (1.2) for the NEP of a lumped-element bolometer.

Before estimating the NEP, we give an example of how the effective thermal parameters in (4.14) are modified by the finite size of the YBCO thermometer. A practical bolometer design would not use a YBCO thermometer which measures the temperature only at the center of the membrane as was assumed in (4.8). Such a thermometer would probably have much film noise because of its small size and also could not be used as the radiation absorber. We consider the response of a disc-shaped thermometer which covers the central $\sim 80\%$ of the membrane area. The thermometer film is kept away from the membrane edge to avoid averaging over the large thermal gradients which occur there. We assume the sheet resistance R_A of the thermometer film has a linear dependence on temperature such that $dR_A/dT = const.$ If current density is constant everywhere in the thermometer, the component of the thermometer resistance which oscillates in response to modulated incident radiation is

$$R_1(\omega) = 2\int_0^{0.9a}\left(2\int_0^{\sqrt{0.8a^2-x^2}}\left[\frac{dR_A}{dT}T_1(x^2+y^2,\omega)\right]^{-1}dy\right)^{-1}dx\,. \qquad (4.15)$$

Equation (4.15) can be integrated numerically. Assume that the incident power is $\rho_o\Omega = 1\,\mu$W and that $dR_A/dT = const.$ everywhere on the YBCO thermometer. Then the effective rise in temperature which is measured by the thermometer is $T_{\rm eff}(\omega) \equiv R_1(\omega)(dR_A/dT)^{-1}$. Effective thermal parameters which account for a thermometer of finite area can be calculated by using $T_{\rm eff}(\omega)$ in place of $T_1(0,\omega)$ in (4.13). The new effective thermal admittance is defined as $|G'_{\rm eff} + i\omega C'_{\rm eff}| \equiv \rho_o\Omega/T_{\rm eff}(\omega)$.

In the limit $\omega\tau_r \gg 1$, the thermal admittance is $\omega C'_{\rm eff}$. For $\omega\tau_r = 125$, solving (4.6) and (4.15) gives $C'_{\rm eff} = 2.6\times10^{-7}$ J/K for the YSZ bolometer described above. For $\omega\tau_r \ll 1$, the thermal admittance is $G'_{\rm eff}$ and for $\omega\tau_r = 0.15$, $G'_{\rm eff} = 1.7\times10^{-5}$ W/K. The effective thermal parameters are

$$C'_{\rm eff} \;=\; 0.9c_p\Omega\,,$$

$$\begin{aligned} G'_{\rm eff} &= 23\kappa t_{\rm YSZ}\,, \\ \tau'_{\rm eff} &\equiv C'_{\rm eff}/G'_{\rm eff} = 0.12\tau_r\,. \end{aligned} \tag{4.16}$$

For the membrane and thermometer geometries that we chose, $C'_{\rm eff}$ is 90% of the total heat capacity of the membrane and $G'_{\rm eff}$ is 23 times the thermal conductance associated with uniform heat flow through a square of the membrane. The time constant $\tau'_{\rm eff}$ is more useful to bolometer designers than τ_r. The responsivity of the membrane bolometer is reduced by a factor $0.9/\sqrt{2}$ when $\omega\tau'_{\rm eff} = 1$. For comparison, the responsivity of a lumped-element bolometer is reduced by a factor $1/\sqrt{2}$ when $\omega\tau = 1$.

The NEP of the YSZ membrane bolometer can be estimated using the equation for the NEP (1.2) of a composite bolometer with the parameter $|G'_{\rm eff} + i\omega C'_{\rm eff}|$ substituted for $|G + i\omega C|$. If the current I is adjusted so that the inequality (3.2) is satisfied, the voltage fluctuations from $1/f$ noise in the YBCO film will be larger than the voltage fluctuations from the readout amplifier. Then thermal fluctuations and thermometer noise are the dominant contributions to the NEP. We will calculate the contribution to the NEP from thermal fluctuations and from voltage fluctuations in the YBCO thermometer for $\omega\tau'_{\rm eff} = 1$, which occurs at $\omega/2\pi = 11$ Hz. At $\omega\tau'_{\rm eff} = 1$, $T_{\rm eff}(\omega) = 35\,{\rm mK}$ for the YSZ membrane bolometer. Therefore, the thermal admittance is $|G'_{\rm eff} + i\omega C'_{\rm eff}| = 2.8 \times 10^{-5}\,{\rm W/K}$. The NEP contribution from thermal fluctuations calculated from (2.1) is ${\rm NEP}_{\rm thermal} = 3.5 \times 10^{-12}\,{\rm W\,Hz^{-1/2}}$ for $T = 90\,{\rm K}$. We assume that the thermometer is a film of YBCO with equivalent noise to the film of YBCO/YSZ/Si described in Table 3.1. The contribution to the NEP from thermometer noise is then

$$|G'_{\rm eff} + i\omega C'_{\rm eff}| \cdot {\rm NET} = 1.7 \times 10^{-12}\,{\rm W\,Hz^{-1/2}}\,. \tag{4.17}$$

Hence, at $\omega/2\pi = 11\,{\rm Hz}$, the NEP of the YSZ nonisothermal bolometer is limited by thermal fluctuation noise. Since the responsivity is approximately constant at frequencies below 11 Hz, thermal fluctuations are the dominant contribution to the NEP for $\omega/2\pi < 11\,{\rm Hz}$. For frequencies above 11 Hz, the admittance $|G'_{\rm eff} + i\omega C'_{\rm eff}| \approx \omega C'_{\rm eff}$. Therefore the contribution to the NEP from thermometer fluctuations is proportional to ω. For $\omega/2\pi = 18\,{\rm Hz}$ the contributions to the NEP from thermometer noise and thermal fluctuations are equal. For $\omega/2\pi > 18\,{\rm Hz}$, the NEP is dominated by thermometer noise and is proportional to ω. The total NEP arising from thermal fluctuations and thermometer noise corresponds to a detectivity $D^* = 2.3\times10^{10}\,{\rm cm\,Hz^{1/2}/W}$ at 11 Hz. The detectivity for the YSZ nonisothermal

bolometer at 11 Hz compares favorably with $D^* = 4.2 \times 10^9\,\mathrm{cm\,Hz^{1/2}/W}$ for the sapphire composite bolometer and $D^* = 2 \times 10^8\,\mathrm{cm\,Hz^{1/2}/W}$ for the pyroelectric detector, both measured at 10 Hz.

Assume that the bolometer operates in a regime where thermometer noise is the largest contribution to the NEP. For the YBCO film on YSZ on Si in Table 3.1, the dynamic range (4.1) is $D.R. = 3{\times}10^7 = 150\,\mathrm{dB}$. Equation (4.1) is basically correct for both a lumped-element bolometer and for the membrane bolometer. The dynamic range written this way is independent of the optical throughput and of the thermal parameters of the bolometer. For a detector to realize the dynamic range (4.1), the incident power must be kept below P_{max}, the largest power to which the bolometer responds linearly.

The YSZ nonisothermal bolometer may be useful for commercial infrared spectrometers. A typical Fourier transform infrared spectrometer (FTIR) sold by Nicolet, Inc. has a 1500 K blackbody source of infrared radiation. Assume that the spectral range of interest is $40 - 400\,\mathrm{cm^{-1}}$, the optical efficiency is 10%, and an f/1 mirror focuses the radiation onto a $1\,\mathrm{mm^2}$ detector. The power in this band computed from (1.6) is 3.4 mW. Some pyroelectric detectors can operate linearly at this power level. For a YBCO thermometer with $\delta T = 2\,\mathrm{K}$, the maximum power that the YSZ bolometer can measure without saturating is $P_{\mathrm{max}} = 56\,\mu\mathrm{W}$ at 10 Hz. An infrared power of 3.4 mW would readily saturate the YSZ bolometer. The infrared power must be attenuated either with a 1% neutral density filter or by reducing the optical throughput $A\Omega$ by a factor of $\alpha = 0.01$. Reducing the efficiency of the optical system allows the bolometer to operate in the linear regime but increases the NEP by a factor of $\alpha^{-1} = 100$. The NEP of the bolometer mounted in the FTIR can be written as

$$\mathrm{NEP} = \frac{P_{\mathrm{max}}}{\alpha \cdot (D.R.)}\,. \tag{4.18}$$

A bolometer which is operated in such a spectrometer with $\alpha < 1$ is more sensitive than a pyroelectric detector operating just below its saturation power only if the dynamic range of the bolometer is larger than the dynamic range of the pyroelectric detector. The dynamic range of the pyroelectric detector is limited by the analog-to-digital converter (ADC) in the readout electronics of the Nicolet FTIR[64]. Currently available ADC's use 16 bits and have 96 dB of dynamic range[65]. Signal processing techniques in the FTIR such as gain-switching can increase the effective dynamic range to $\sim 120\,\mathrm{dB}$. If the pyroelectric detector and the YSZ membrane bolometer use the same ADC in the FTIR, their effective dynamic

ranges are equal. Hence, the sensitivity of a YSZ membrane bolometer is at best equal to the sensitivity of a pyroelectric detector for FTIR applications with high background loading.

Some spectroscopic measurements have low background loading. Two examples are measurements of very small samples, and transmittance measurements of opaque samples. The YSZ bolometer is more sensitive than the pyroelectric detector if the infrared power loading P_o satisfies the condition

$$P_o < (\mathrm{NEP}_{\mathrm{pyro}}) \cdot (D.R.), \tag{4.19}$$

where $\mathrm{NEP}_{\mathrm{pyro}}$ is the NEP of the pyroelectric detector and $D.R. = 120\,\mathrm{dB}$.

A YSZ bolometer with a neutral density filter which can be placed in and out of the optical path may have applications for this type of spectrometer. The YSZ bolometer would give equivalent performance to the pyroelectric detector for high background measurements, and superior performance for low background measurements. For frequencies $\nu > 400\,\mathrm{cm}^{-1}$, the competing detector technology is HgCdTe cooled to 77 K. The detectivity of the YSZ bolometer $D^* = 2.3 \times 10^{10}\,\mathrm{cm\,Hz}^{1/2}/\mathrm{W}$ at 11 Hz is slightly worse than for HgCdTe $D^* = 4 \times 10^{10}\,\mathrm{cm\,Hz}^{1/2}/\mathrm{W}$ [66]. The detectivity of the YSZ bolometer, however, degrades at higher modulation frequencies as ω^{-1} while D^* of the HgCdTe detector is roughly constant until $\omega/2\pi \approx 1\,\mathrm{MHz}$.

The most common spectrometers are gas-purged rather than evacuated. They are susceptible to low-frequency noise from the air-conditioners in many laboratories. Therefore, the rapid-scan mirror is typically operated at a speed v_{mirror} such that the fringe frequency $\omega/2\pi = 2v_{\mathrm{mirror}}/\lambda$ is $> 200\,\mathrm{Hz}$. The YSZ membrane bolometer is in the roll-off regime $\omega\tau_{\mathrm{eff}} > 1$ at 200 Hz. Isothermal composite bolometers are typically designed to be operated at $\omega\tau < 1$ in order to avoid the $1/\omega$ frequency-dependence of the responsivity. For the YSZ bolometer this corresponds to increasing G_{eff} until $G_{\mathrm{eff}} = \omega_c C_{\mathrm{eff}}$, where ω_c is the highest frequency of the interference fringes. The value of G_{eff} for the YSZ bolometer could be increased by gas-cooling or by adding a layer of metal to the membrane. From (4.17), it is apparent that the NEP is not reduced for $\omega < \omega_c$ by increasing G_{eff} until $G_{\mathrm{eff}} = \omega_c C_{\mathrm{eff}}$. Only the dependence on frequency changes. From (4.1), it is apparent that the dynamic range is not increased by making $G_{\mathrm{eff}} = \omega_c C_{\mathrm{eff}}$. The saturation power P_{max} is increased by a factor $\sqrt{2}$ at ω_c and by a larger factor at lower frequencies. There may be an advantage for FTIR applications in *not* increasing G_{eff} and operating the YSZ bolometer in the regime $\omega\tau_{\mathrm{eff}} > 1$.

As was shown in (1.6), the power per unit bandwidth from a blackbody which couples to a bolometer with a fixed throughput is proportional to λ^{-3}. For short wavelengths near λ_c, the power is large and produces fringes with large amplitude at $\omega = \omega_c$. An optimized YSZ bolometer would have the infrared signal attenuated by a factor α until the power associated with the fringes at ω_c is just below P_{max}. At longer wavelengths, the fringes are smaller and occur at $\omega < \omega_c$. The power associated with the fringes for $\omega < \omega_c$ is much less than P_{max}. Therefore, the signal-to-noise ratio of a spectrum at long wavelengths can be improved without saturation by a YSZ bolometer which operates in the roll-off regime since its NEP is reduced in proportion to ω. If desired, the $1/\omega$ dependence in the responsivity can be cancelled in the read-out circuit by placing a capacitor in series with the input of the preamplifier as is shown in Fig. 4.2. This has the effect of making the responsivity independent of frequency while preserving the factor of ω reduction of the NEP at low fringe frequencies.

4.3 Summary

A nonisothermal bolometer on a YSZ membrane with a YBCO infrared absorber might be the next generation high-T_c bolometer after the sapphire composite bolometer. The YSZ membrane bolometer can be both sensitive and easy to manufacture. A thermal analysis of a disc-shaped membrane bolometer shows that a nonisothermal bolometer can be modeled as a lumped-element, composite bolometer with effective values of C, G, and τ. We used values of these parameters for a YSZ membrane bolometer with a diameter of 1 mm and a thickness of 0.5 μm to predict a detectivity of $D^* = 2.3 \times 10^{10}\,\mathrm{cm\,Hz^{1/2}/W}$ at 11 Hz. This value of D^* is superior to the D^* of the sapphire composite bolometer and of the pyroelectric detector. The YSZ bolometer may have application to commercial infrared spectrometers.

Chapter 5

Theory of Superconducting Tunnel Junctions

This chapter provides some of the theoretical background necessary for understanding the high-frequency response of superconducting tunnel junctions. First, we discuss the energy gap and the density of states of a superconductor predicted by Bardeen, Cooper, and Schrieffer. These quantities are then used to derive an expression for the DC current-voltage characteristic. Finally, Werthamer's description of the high-frequency response of tunnel junctions is presented in the frequency-domain and in the time-domain.

5.1 BCS theory

A brief outline follows of some basic results of Bardeen-Cooper-Schrieffer (BCS) theory which apply to tunnel junctions[67]. Excellent descriptions of BCS theory exist in several books[68]-[70].

5.1.1 Energy gap

In 1956, Cooper presented his pair wavefunction by showing that the Fermi sea of electrons in a metal is unstable against the formation of a bound pair of electrons. This instability occurs regardless of how weak the interaction is, so long as it is attractive. Prior to 1956, Pines built on the work of Fröhlich and showed that within the "jellium" model the screened Coulomb repulsion can be weaker than the attractive interaction which occurs

when two electrons of opposite spin and momentum exchange virtual phonons of roughly the Debye energy. The basic idea is that the first electron polarizes the medium by attracting positive ions. These ions then attract the second electron, giving an effective attractive potential V between the electrons. A short Thomas-Fermi screening length is a necessary condition for the phonon-mediated attraction to be shielded from the Coulomb repulsion.

Below the critical temperature T_c, Cooper pairs form out of the unstable Fermi sea until the binding energy for creating an additional pair goes to zero. In BCS theory, this binding occurs for electrons within an energy $\hbar\omega_c$ from the Fermi surface, where $\hbar\omega_c$ is the cutoff energy of the attractive interaction V. The bound pairs can be thought of as overlapping composite particles with integral spin. They condense into a ground state with a condensation energy of approximately $-N(0)\Delta^2(0)/2$, where Δ is the superconducting energy gap and $N(0)$ is the density of states at the Fermi surface of the metal in the normal state. The first excited quasiparticle state is an energy Δ above the ground state. There are no low energy excitations below this energy. Two useful results from BCS involving the energy gap are

$$\begin{aligned} kT_c &= 1.13\hbar\omega_c \exp(-1/N(0)V) \approx 2\Delta(0)/3.52\,,\ N(0)V \ll 1\,, \\ \frac{\Delta(T)}{\Delta(0)} &\approx 1.74\left(1-\frac{T}{T_c}\right)^{1/2}\,, \end{aligned} \tag{5.1}$$

For bulk niobium, $T_c = 9.25\,\mathrm{K}$ and $2\Delta(0) = 3.05\,\mathrm{mV}$ [70].

5.1.2 Density of states

The excited states from the BCS ground state are Bogoliubov quasiparticle states. The Bogoliubov quasiparticle wavefunction can be written as a superposition of electron-like and hole-like excitations of the normal Fermi sea. The energies of these Bogoliubov excitations are

$$E_k = (\xi_k^2 + |\Delta_k|^2)^{1/2}\,, \tag{5.2}$$

where $\xi_k = (\hbar k)^2/2m$ is the kinetic energy of a single particle. There is a one-to-one correspondence between the Bogoliubov quasiparticles and the single particles of the normal state such that the density of states for the superconductor $N_s(E)$ can be related to the density of states for the normal metal $N_n(\xi)$.

$$N_s(E)dE = N_n(\xi)d\xi\,. \tag{5.3}$$

Combining (5.3) with (5.2) leads to the result

$$\frac{N_s(E)}{N_n(\xi)} = \frac{d\xi}{dE} = \begin{cases} \frac{E}{(E^2-\Delta^2)^{1/2}}, & (E > \Delta) \\ 0, & (E < \Delta) \end{cases} \tag{5.4}$$

A divergence arises in (5.4) at $E = \Delta$ since excitations with $\xi_k < \Delta$ that were in the gap region in the normal state have their energies raised above Δ in the superconducting state. The sharp divergence in $N_s(E)$ is a consequence of the sharp cutoff of the attractive pairing potential V at $\hbar\omega_c$. In real materials, the detailed shape of the peak in the density of states depends on the actual electron-phonon interaction and there are corrections to the shape of (5.4) of order $(T_c/\Theta_D)^2$, where Θ_D is the Debye temperature.

5.2 Tunneling

Ivar Giaever discovered the tunneling of quasiparticles through a thin insulating barrier between pairs of superconductors (SIS junction) and between a superconductor and a normal metal (SIN junction)[71]. He used quasiparticle tunneling measurements to confirm the density of states and the temperature dependence of the energy gap predicted by BCS. Two years later in 1962, Brain Josephson's prediction of pair tunneling—the Josephson current—along with its phase coherent properties eclipsed much of the work on applications on quasiparticle tunneling. The Josephson currents have been successfully exploited in low-frequency SQUID technology and show promise for high-speed digital technologies. Interest returned in the late 1970s to the quasiparticle tunneling current when Paul Richards discovered that the quasiparticle response of SIS junctions has nearly ideal properties for making microwave heterodyne mixers with low-noise. In this section we follow the treatment of Cohen, Falicov, and Phillips[72] for calculating the DC current-voltage (I-V) characteristic for the quasiparticle current and then we discuss Werthamer's[73] generalization of the theory for calculating the high-frequency response.

There is a non-zero probability of charge transfer by tunneling of electrons through the thin barrier that separates two superconductors in a SIS junction. This probability decays exponentially with the separation distance and depends on the details of the insulating material and on screening effects from the image potential in the superconductors. These aspects of the tunnel barrier can be lumped into a phenomenological tunneling matrix element T_{kq}. A perturbative term in the Hamiltonian which describes coupling between the

superconducting wavefunctions on either side of the barrier is

$$H_T = \sum_{k\,q} (T_{kq} c_k c_q^\dagger + T_{kq}^* c_q c_k^\dagger)\,, \tag{5.5}$$

where c_k (c_q) are electron destruction operators for the right (left) side of the junction and $c_k^\dagger$ ($c_q^\dagger$) are the electron creation operators. The total Hamiltonian for the system is

$$H = H_L + H_R + H_T + eV(t)N_L\,, \tag{5.6}$$

where H_L and H_R are the many-body Hamiltonians describing the left and right electrode respectively. The applied voltage is $V(t)$ and is assumed to modulate the chemical potential of the single-particle states on the left side described by the number operator

$$N_L = \sum_{k\sigma} {c_k}^\dagger c_k\,. \tag{5.7}$$

As long as we exclude the coherent processes of Josephson tunneling, the transition probability—and hence the current—is to first order proportional to $|\langle H_T \rangle|^2$. An important point is that the electron operators $c, c^\dagger$ must be written in terms of the Bogoliubov quasi-particle excitations of the superconductor before the perturbative terms associated with (5.5) can be calculated. For example[68],

$$c_{k\uparrow}^\dagger = u_k \gamma_{ek0}^\dagger + \nu_k^* \gamma_{hk1}\,, \tag{5.8}$$

where u_k and ν_k are BCS coherence factors and $\gamma_{ek0}^\dagger$ and γ_{hk1} are electron-like creation and hole-like destruction operators respectively. After squaring the matrix element associated with H_T, the first order contribution to the tunneling current is proportional to

$$(|u_k|^2 + |\nu_k|^2)|T_{kq}|^2 = |T_{kq}|^2\,. \tag{5.9}$$

The probability that a given pair state ($k\uparrow, -k\downarrow$) is occupied in the BCS ground state is

$$|\nu_k|^2 = 1 - |u_k|^2 = 1/2(1 - \xi_k/E_k)\,. \tag{5.10}$$

The BCS coherence factors of the form $u_k\nu_k$ drop out of the first order contribution to the tunneling current.

The disappearance of the coherence factors allows the computation of the tunneling current to be expressed in the "semiconductor model." In this model, the superconductor is represented by an ordinary semiconductor with a density of independent-particle states

obtained from (5.4) for positive and negative values of E. Here, the zero in E occurs at the Fermi energy of the normal metal. Also, elastic tunneling through the barrier is assumed—that is, there are no mechanisms for energy loss in the barrier. If the strength of the coupling between the superconducting electrodes through the barrier is small, then T_{kq} is small and H_T can be taken to first order:

$$\begin{aligned} I_{dc}(V) &= \frac{2\pi e}{\hbar^2}\sum_{kq\sigma}\int_{-\infty}^{\infty} d\omega_L d\omega_R |T_{kq}|^2 A_L(k,\omega_L) A_R(K,\omega_R) \times \\ &\quad [f(\hbar\omega_L) - f(\hbar\omega_R)]\delta(eV/\hbar + \omega_L - \omega_R), \end{aligned} \tag{5.11}$$

where $f(\hbar\omega) = [\exp(\hbar\omega/kT)]^{-1}$ is the Fermi-Dirac distribution function, and A_L, A_R are the single-particle spectral distribution functions for the left and right-side electrodes. In BCS, the spectral distribution function is given by

$$A(k,\omega) = |u_k|^2\delta(\omega - E_k/\hbar) + |\nu_k|^2\delta(\omega + E_k/\hbar)\,. \tag{5.12}$$

Substituting (5.10) and (5.12) into (5.11) gives

$$I_{dc}(V) = \frac{1}{R_N}\int_{-\infty}^{\infty} \frac{E - eV}{[(eV-E)^2 - \Delta_L^2]^{1/2}} \frac{E}{[E^2 - \Delta_R^2]^{1/2}} [f(E - eV) - f(E)]dE. \tag{5.13}$$

Here, we have assumed that $|T_{kq}|$ is constant over the energy range of interest and can be absorbed into R_N, the normal resistance of the junction at voltages $V > (\Delta_L + \Delta_R)/e$.

The semiconductor model provides an intuitive picture for describing the I-V curve. Figure 5.1 is a plot of the density of states (5.4) for single-particle excitations as a function of energy for each electrode. At $T = 0$ there are no thermally excited quasiparticles and there is an energy gap for tunneling to take place of $eV_g = (\Delta_L + \Delta_R)$. At this voltage, there is sufficient energy for an electron-like particle to tunnel into the conduction band on the right side, leaving a hole-like particle on the left side. This process represents a Cooper pair becoming unbound with one of the constituent electrons tunneling across the junction. Because of the singularity in the density of states, the onset of tunneling current is rapid. Above the sum-gap voltage V_g, the current I_{dc} asymptotically approaches V/R_N. Figure 5.2a shows an experimentally measured I-V curve for a $2 \times 2\,\mu$m $Nb/AlO_x/Nb$ junction fabricated at Conductus by A. T. Barfknecht. In an ideal BCS junction, the current rise at the sum-gap voltage is infinitely sharp. In real junctions, the current rise is smeared out by effects such as gap inhomogeneity, gap anisotropy, and quasiparticle lifetime broadening.

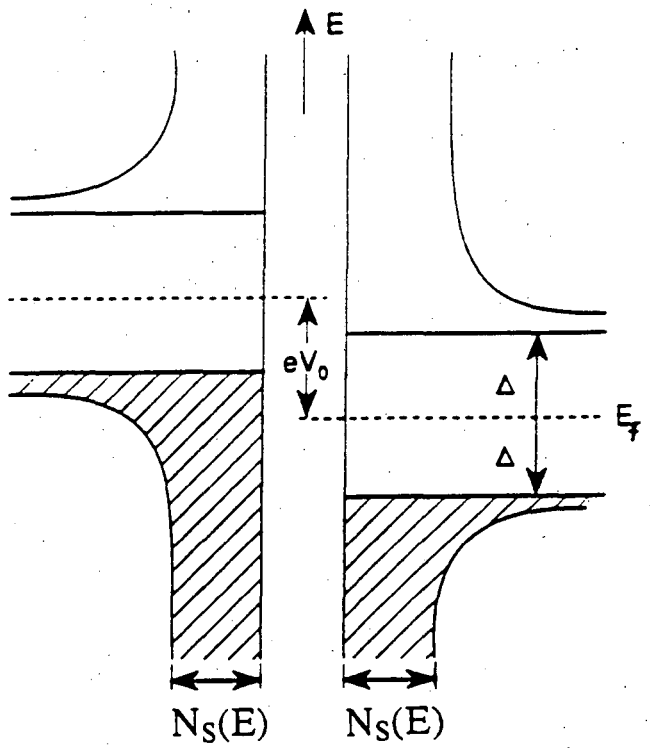

Figure 5.1: Energy for single-particle excitations in the semiconductor model of a SIS junction plotted against the density of states $N_s(E)$ for both superconducting electrodes. No current flows until the voltage $eV_o = 2\Delta$ and filled states in the left electrode can tunnel into the vacant states in the right electrode.

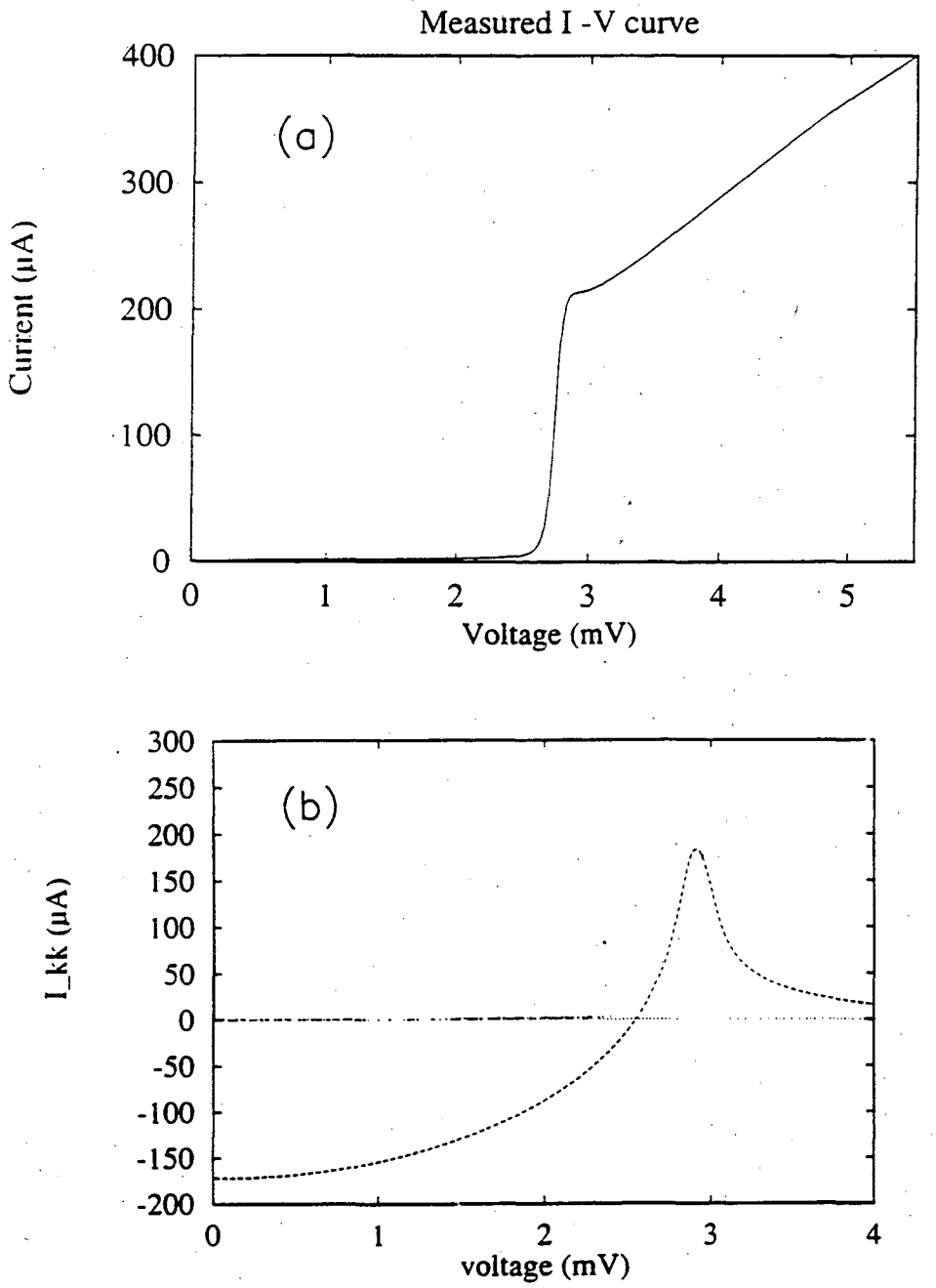

Figure 5.2: (a) Experimentally measured I-V curve of a $Nb/AlO_x/Nb$ trilayer SIS junction. The device area is $2 \times 2\,\mu m$. (b) Kramers-Kronig transform of the I-V curve.

5.3 High-frequency response of tunnel junctions

In this section, we outline the theory of the high-frequency response of the quasiparticle current in superconducting tunnel junctions. First, we follow the treatment of Werthamer in the frequency-domain[73]. Next we discuss the work of Harris and of Tucker in extending Werthamer's theory to the time domain[74, 75].

5.3.1 Frequency-domain theory

Werthamer used perturbation theory based on the Hamiltonian (5.6) and derived an expression for the tunneling current as a function of time in the presence of a time-varying voltage $V(t)$ and a DC bias voltage V_o.

$$\begin{aligned}\langle I(t)\rangle &= Im\int_{-\infty}^{\infty} d\omega d\omega' \Big(W(\omega)W^*(\omega')e^{-i(\omega-\omega')t} j_{qp}(\omega' + eV_o/\hbar) + \\ &\quad W(\omega)W(\omega')e^{-i(\omega+\omega')t+i\phi} j_p(\omega' + eV_o/\hbar)\Big)\,. \end{aligned} \tag{5.14}$$

Here, $j_{qp}(\omega)$ and $j_p(\omega)$ are the response functions of quasiparticles and Cooper pairs respectively. The first term in (5.14) is the quasiparticle tunneling current. The second term is the pair tunneling current which depends on the phase difference ϕ between the BCS ground state wavefunctions on the two sides of the junction. The real parts of the response functions correspond to reactive components in the current which lead or lag the applied AC voltage. The imaginary parts correspond to the resistive components which are in-phase with the applied voltage. The function $W(\omega)$ is the Fourier transform of the time-evolution operator $W(t)$ used in the interaction picture of time-dependent perturbation theory.

$$W(t) = \exp\left(-i\frac{e}{\hbar}\int_t dt'(V(t') - V_o)\right) = \int_{-\infty}^{\infty} d\omega W(\omega)e^{-i\omega t}\,. \tag{5.15}$$

For ideal BCS-like SIS junctions, the response functions j_{qp} and j_p can be calculated using the density of states for quasiparticles and Cooper pairs[73]. However, the calculation is tedious and does a poor job of modeling a real junction with the onset in current at V_g broadened. The quasiparticle response function j_{qp} can be obtained directly from the measured DC I-V curve. When the voltage across the junction contains only a DC component V_o, then $W(\omega) = \delta(\omega)$, and (5.14) becomes

$$\langle I(t)\rangle = Im[j_{qp}(eV_o/\hbar)] + Re[j_p(eV_o/\hbar)]\sin\phi + Im[j_p(eV_o/\hbar)]\cos\phi\,. \tag{5.16}$$

Because of the Josephson relation $\dot{\phi} = 2eV_o/\hbar$, the second and third terms oscillate at the Josephson frequency and the only contribution to the DC current comes from the first term. Therefore, the imaginary part of the quasiparticle response function is equal to the DC I-V curve

$$Im[j_{qp}(\omega_o)] = I_{dc}(V_o)\,, \tag{5.17}$$

where $\omega_o \equiv eV_o/\hbar$. The real part $Re[j_{qp}(eV_o)]$ does not contribute to the DC I-V characteristic. Therefore, measurements of the current in an SIS junction biased with a static voltage are not sensitive to the reactive component of the quasiparticle current. Instead, AC measurements are needed to measure the reactive component. In contrast, both the reactive $\cos\phi$ term and the resistive $\sin\phi$ term of the Josephson current contribute to the current when a static voltage biases the junction.

If we assume the shape of the DC I-V curve is known for all voltages, then we know $Im[j_{qp}(\omega_o)]$ for all frequencies. As is required by any finite, causal response function, $Re[j_{qp}(eV_o)]$ is related to the imaginary part by a Kramers-Kronig transform. For $j_{qp}(\omega)$,

$$\begin{aligned} Re[j_{qp}(\omega)] &= P\int_{-\infty}^{\infty} \frac{d\omega'}{\pi} \frac{Im[j_{qp}(\omega')] - \hbar\omega'/eR_N}{\omega - \omega'} \\ = I_{kk}(V) &= P\int_{-\infty}^{\infty} \frac{dV'}{\pi} \frac{I_{dc}(V') - V'/R_N}{V' - V}\,. \end{aligned} \tag{5.18}$$

In (5.18) an ohmic term is subtracted from the I-V curve to avoid a divergence of the integral. The result of the Kramers-Kronig transform in unaffected since only the nonlinear part of the I-V curve gives rise to a reactive component I_{kk}. Figure 5.2a shows an experimentally measured I-V curve and Fig. 5.2b shows its Kramers-Kronig transform. The peak in I_{kk} arises from the sharp nonlinearity in the I-V curve at V_g. For an ideal BCS junction, the peak in I_{kk} diverges logarithmically [73]-[75] at V_g.

In summary, using (5.14), (5.17), and (5.18) allows one to calculate the frequency-dependent response of the quasiparticle current to an arbitrary voltage waveform. The DC I-V curve, which is easily measured, contains all the information about the response of single-particle excitations in the SIS junction at high frequencies. This statement is subject to two conditions. First, the tunneling through the barrier must be elastic. Second, quasiparticles must not interact with each other and cause a loss of phase coherence in the tunneling. This condition is only met when the first term in H_T in the perturbation theory expansion is sufficient to describe the data.

5.3.2 Time-domain theory

Equation (5.14) for the frequency-domain is convenient for calculating the response of the quasiparticle current to an RF voltage of a single frequency. This equation is the basis for the quantum theory of SIS mixers[75]. In the small signal limit where the quasiparticle current responds linearly to an applied voltage, the results of (5.14) can be calculated for many RF frequencies and superposed. When nonlinear effects become important at larger signal levels, the different frequencies mix together and the frequency-domain calculation is no longer convenient for a large number of frequency components.

Following Harris[74], the quasiparticle tunneling current may alternatively be expressed in a form suitable for analysis in the time domain[76].

$$\langle I(t)\rangle = \frac{V(t)}{R_N} + Im\left(U^*(t)\int_{-\infty}^{t} dt'\bar{\chi}(t-t')U(t')\right). \tag{5.19}$$

The time-dependent phase factor induced by the potential across the barrier is represented as

$$U(t) = \exp\left(-i\frac{e}{\hbar}\int_{-\infty}^{t} dt'V(t')\right), \tag{5.20}$$

where $V(t)$ is the total potential across the junction. The phase factor $U(t)$ results from calculating the perturbation term $eV(t)N_L$ in (5.6) to all orders. The response function characterizing the nonlinear behavior of the junction is given by

$$\bar{\chi}(t) = \frac{2}{\pi}\int_0^{\infty} d\omega\left(I_{dc}(\hbar\omega/e) - \frac{\hbar\omega}{eR_N}\right)sin(\omega t). \tag{5.21}$$

Here we have assumed the DC I-V curve is antisymmetric, $I_{dc}(-V) = -I_{dc}(V)$, and that it approaches an ohmic resistance R_N at large bias voltages. The response function $\bar{\chi}(t)$ results from calculating the perturbation term H_T in (5.6) to first order. The function $\bar{\chi}(t)$ is the inverse Fourier transform of the response function $Im[(i/4e)j_{qp}(\hbar\omega_o/e)]$.

Equation (5.21) for $\bar{\chi}(t)$ was plotted by McDonald *et al.*[77] for an ideal SIS junction at T=0. The function $\bar{\chi}(t)$ behaves like the impulse response of the SIS junction and oscillates in time with the energy gap frequency $2\Delta/h$. The amplitude of oscillation decays only inversely with t at large times. Therefore, the current depends on the history of the voltage infinitely far into the past. The t^{-1} decay is expected for an ideal junction with an infinitely sharp onset in current since the inverse Fourier transform of a step function in the frequency-domain has temporal oscillations which decay as t^{-1}. For a real junction, the nonlinearity at V_g occurs over a finite range in voltage and $\bar{\chi}(t)$ dies off in a finite time.

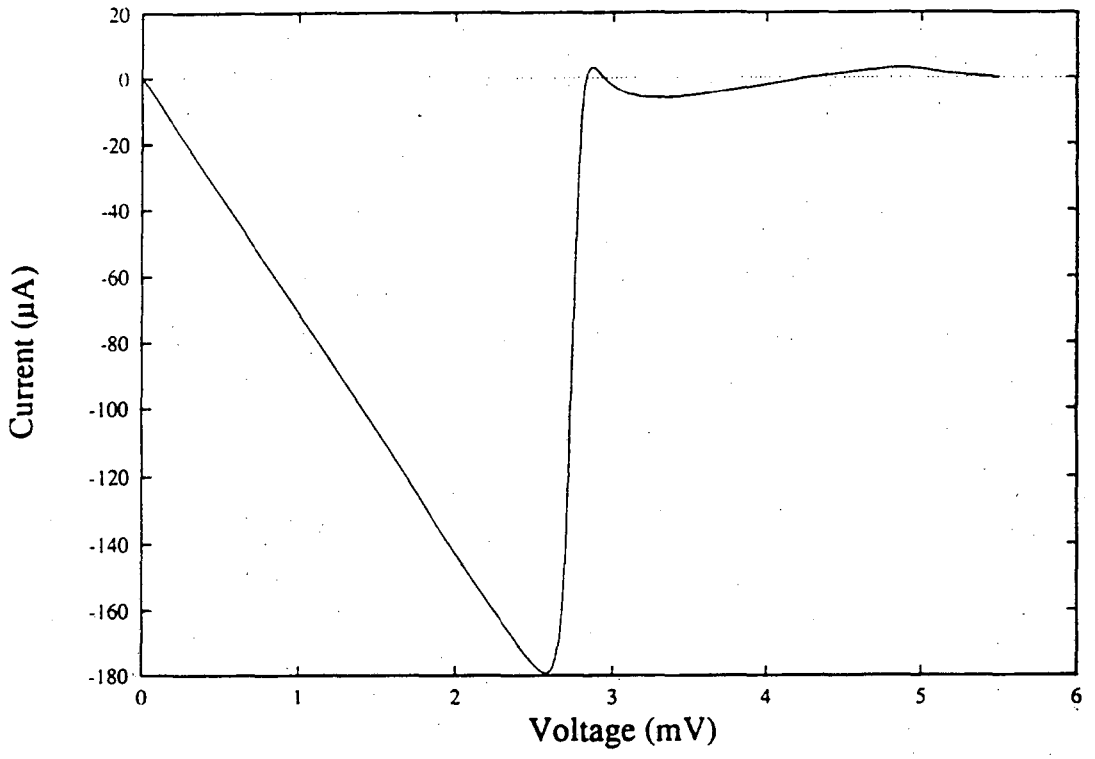

Figure 5.3: Measured I-V curve of a $Nb/AlO_x/Nb$ trilayer SIS junction with the current contribution from the normal resistance V/R_N subtracted.

The response of a junction with a very broad nonlinearity dies off in a short time. Figure 5.3 shows the DC I-V curve of Fig. 5.2a with R_N subtracted. The steep edge at 2.75 mV would be perfectly sharp for an ideal BCS junction. Figure 5.4 shows the response function $\bar{\chi}(t)$ calculated from Fig. 5.3. The oscillations in $\bar{\chi}(t)$ occur at the frequency of the energy gap. The energy gap of this junction is approximately 2.75 mV, slightly below the value for bulk Nb of 3.05 mV. A suppressed gap is common in $Nb/AlO_x/Nb$ trilayer junctions and probably arises from incomplete anodization of the Al film used to make the AlO_x tunnel barrier. The quasiparticles then tunnel into a thin Al film of thickness $< \xi_o$, where ξ_o is the coherence length. The thin film has its gap enhanced by the proximity effect from the Nb layer to a value slightly below the gap of Nb. The oscillations in $\bar{\chi}(t)$ in Fig. 5.2 decay in ~ 20 ps. This decay time arises from the width of the non-linearity shown in Fig. 5.2a.

In the limit where $\bar{\chi}(t)$ becomes negligibly small on a time-scale corresponding to the reciprocal of the applied frequency, the response will be effectively instantaneous. In this case, the tunneling current simply follows the classical, time-dependent modulation of

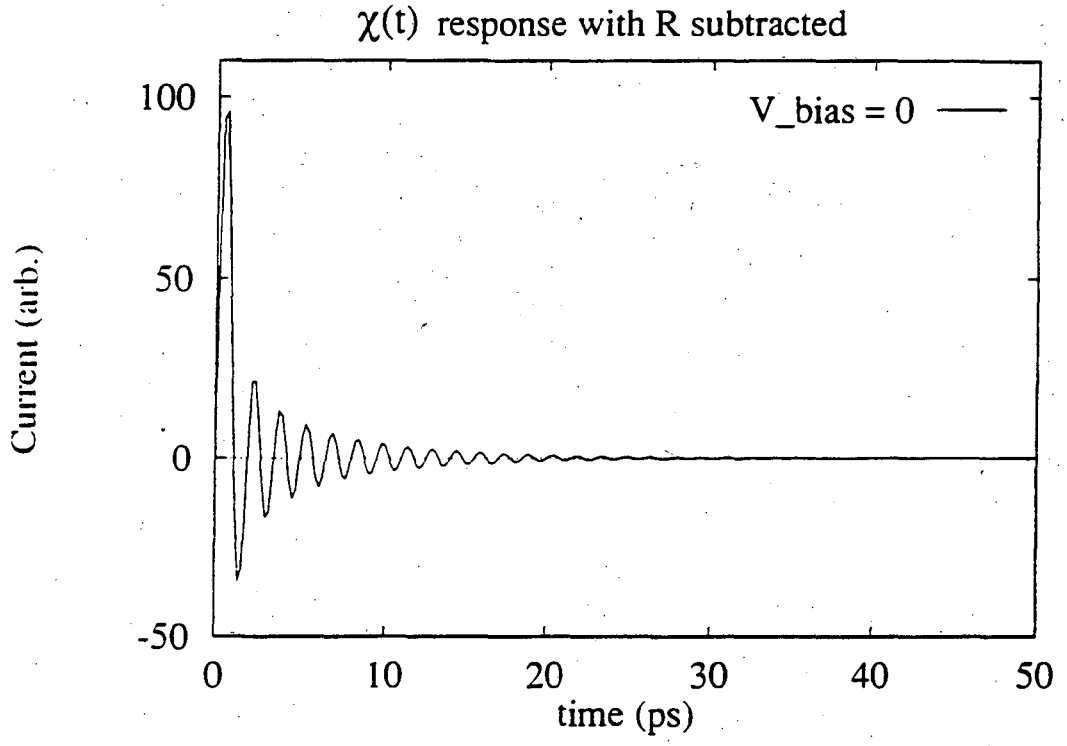

Figure 5.4: Response function $\tilde{\chi}(t)$ for the quasiparticle current calculated from the I-V curve in Fig. 5.3 with R_N subtracted.

the I-V curve and the in-phase conductance is independent of frequency. This regime is referred to as the "classical regime." If, on the other hand, the nonlinearity is sharp enough that $\bar{\chi}(t)$ remains finite over the RF period, then the current is a nonlocal function of time and the device operates in the "quantum regime." Because the junction response is no longer instantaneous, the in-phase conductance becomes frequency-dependent and results in the appearance of nonlinear reactances.

Given knowledge of the temporal RF waveform, the time-domain equation (5.19) allows one to calculate the quasiparticle response in the voltage-biased case. Equation (5.19) is appropriate for calculating the instantaneous current $\langle I(t)\rangle$ flowing through the SIS junction with the DC bias $V_o = 0$. For nonzero bias voltages, the integral in (5.20) diverges. The DC voltage bias can be accounted for in the response function $\bar{\chi}(t)$ by shifting the DC I-V curve along the voltage axis by V_o. This breaks the antisymmetry of the I-V curve about $V = 0$. The response function that should be used in (5.19) is then

$$\bar{\chi}(t) = \frac{i}{\pi}\int_{-\infty}^{\infty} d\omega \left(I_{dc}(\hbar\omega/e - V_o) - \frac{\hbar\omega - eV_o}{eR_N} \right) e^{-i\omega t}. \tag{5.22}$$

The time-dependent phase factor then becomes

$$U(t) = \exp\left(-i\frac{e}{\hbar}\int_{-\infty}^{t} dt'[V(t') - V_o] \right). \tag{5.23}$$

Given the voltage across the SIS junction $V(t)$, and the measured DC I-V curve, we can now calculate the nonlinear response of the quasiparticle current in the time-domain.

As an example of such a calculation, consider the voltage produced by a photoconductive switch. A photoconductor at the terminals of a dipole antenna which is voltage-biased and illuminated with a 100 fs laser pulse can produce a pulse of RF voltage at millimeter wave frequencies[83, 84]. Figure 5.5 shows the RF voltage produced by a photoconductive switch. Chapter 6 describes this particular photoconductive switch in detail. Using the voltage waveform in Fig. 5.5, we can calculate the time-dependent phase factor (5.23) and then convolve $U(t)$ with $\bar{\chi}(t)$ in (5.22) to calculate the quasiparticle current $\langle I(t)\rangle$. Figure 5.6 shows the results of such a calculation for bias voltages of 2.3 mV and 2.1 mV. For a bias voltage of 2.3 mV, there is a threshold for absorption of photons with energy $\hbar\omega > 2\Delta - V_o = 0.45\,\text{meV}$. Only the frequency components of the voltage waveform with $\omega/2\pi > 110\,\text{GHz}$ couple to the quasiparticle current. For $V_o = 2.3\,\text{mV}$, the current waveform in Fig. 5.6a resembles the shape of the applied voltage in Fig. 5.5 since most of the frequency components couple to the quasiparticle current. For $V_o = 2.1\,\text{mV}$, the

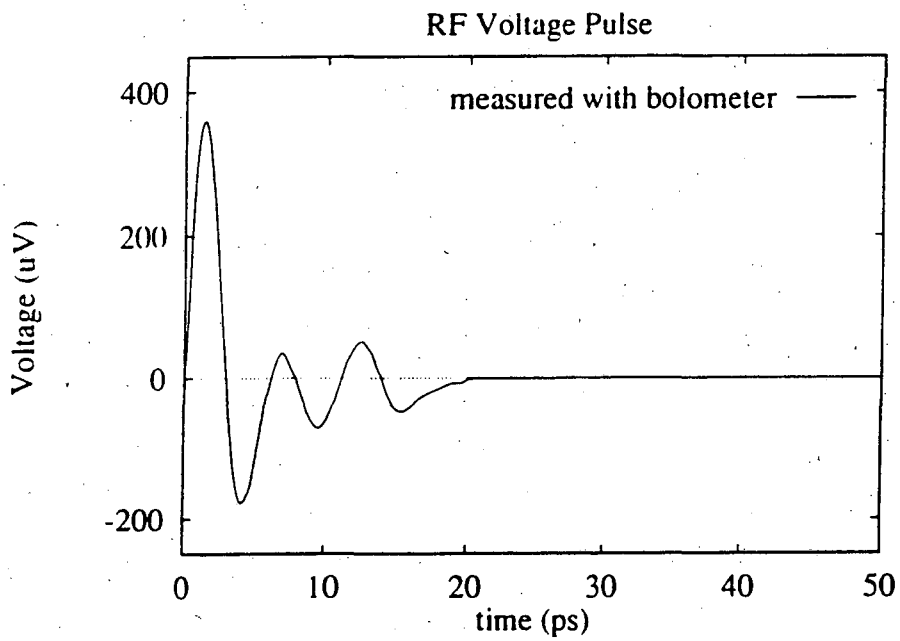

Figure 5.5: Voltage pulse produced by an Auston switch in the time-domain. The pulse shape was deduced using an interferometer and a LHe-cooled bolometer in the method described in Chapter 6.

absorption threshold occurs for $\omega/2\pi > 160$ GHz. The current oscillations of Fig. 5.6b have slightly lower amplitude than in Fig. 5.6a and lack the low-frequency components which appear in Fig. 5.6a. To a good approximation, the quasiparticle current responds linearly to the voltage waveform in Fig. 5.5 for $2.1 < V_o < 2.3$ mV. The quasiparticle current only contains frequency components which are present in the applied voltage.

Figure 5.7 shows the response of the quasiparticle current to the voltage pulse for $V_o = 1.0$ mV. The threshold for absorption of photons occurs for $\omega/2\pi > 424$ GHz. There is no amplitude of oscillation in the voltage of Fig. 5.5 for frequencies above 400 GHz. However, two-photon processes can couple to the quasiparticle current. For example, two photons of energy ω_1 and ω_2 can break a pair if $(\omega_1+\omega_2)/2\pi > 424$ GHz. The high-frequency oscillations in Fig. 5.7 arise from these nonlinear processes. The nonlinear dependence of the phase factor $U(t)$ on the applied voltage accounts for multiple-photon interactions with the quasiparticle current. Multiple-photon processes are treated in the theory since the term $eV(t)N_L$ in (5.6) is taken to all orders in the perturbation expansion. Interactions between quasiparticles can also produce a nonlinear response. These interactions are not

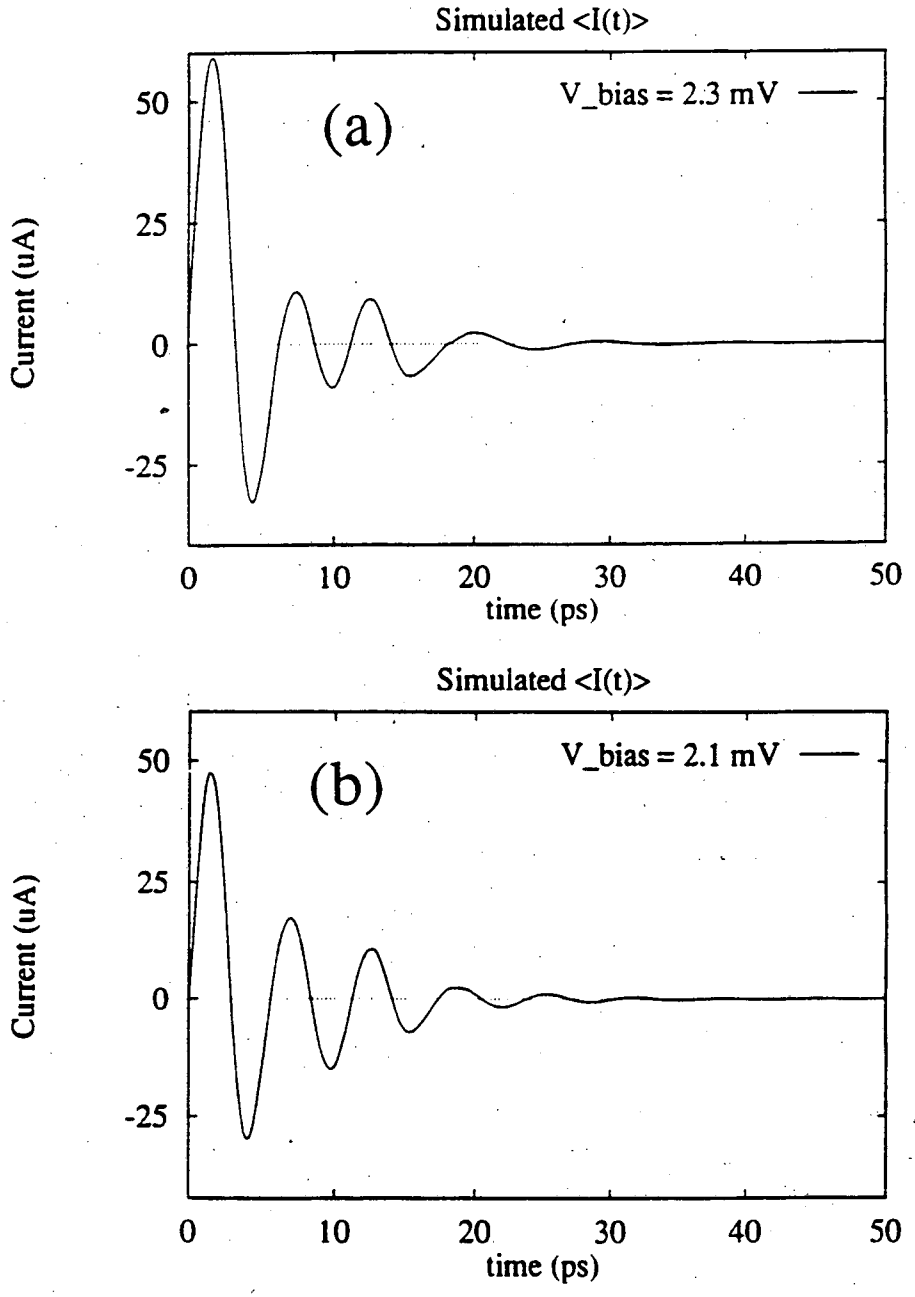

Figure 5.6: Calculation of the response of the quasiparticle current to the voltage pulse in Fig. 5.5. (a) $V_o = 2.3\,\mathrm{mV}$. (b) $V_o = 2.1\,\mathrm{mV}$.

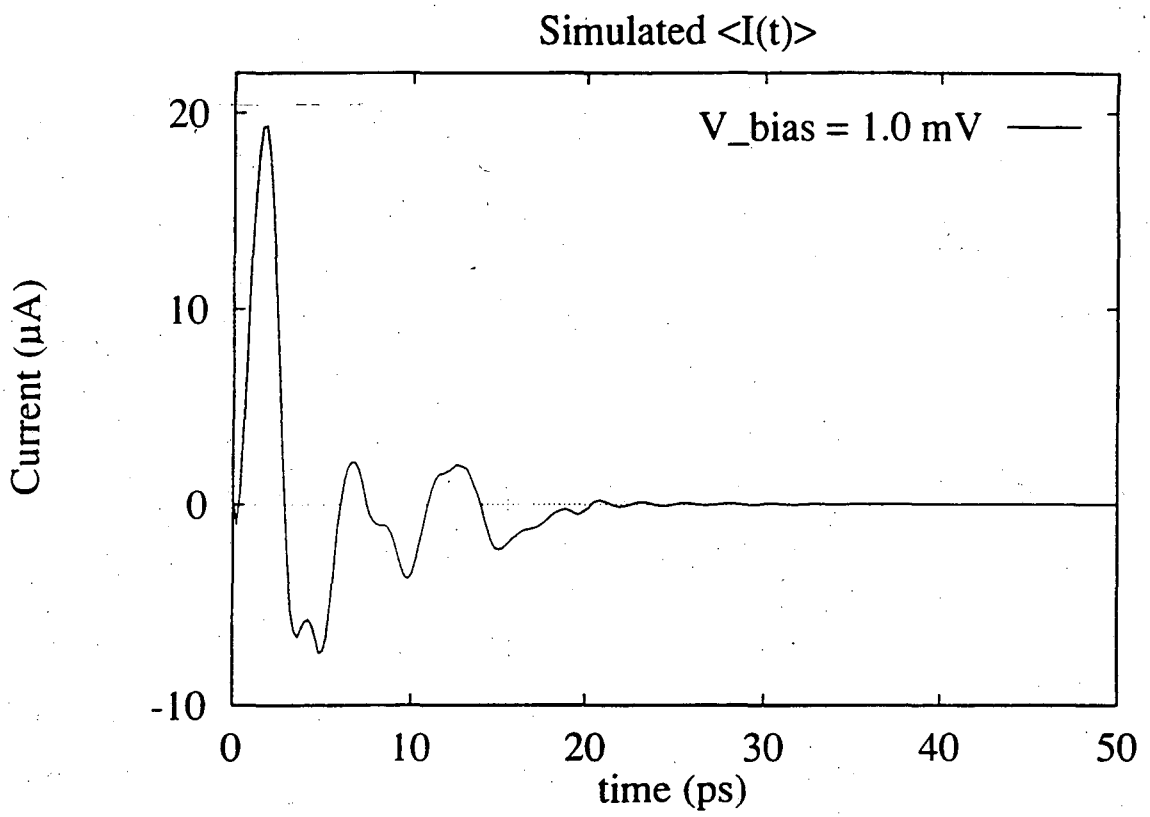

Figure 5.7: Calculation of the nonlinear response of the quasiparticle current to the voltage pulse in Fig. 5.5 for $V_o = 1.0\,\mathrm{mV}$. At this bias voltage, multiple photon processes contribute to the quasiparticle current.

accounted for by the theory since the term H_T in (5.6) is only taken to first order. We will address interactions between quasiparticles in the next chapter.

Chapter 6

Picosecond Response of Nb Tunnel Junctions

In this chapter, we discuss measurements of the response of Nb SIS junctions to picosecond pulses of millimeter wave radiation. This work was a collaboration with Chandu Karadi in the research group of Professor J. W. Orenstein at the University of California at Berkeley. A brief introduction describes previous work with constant wave (CW) sources of millimeter waves. The experimental technique for measuring SIS junctions in the time-domain is then presented. Results for the linear response of the SIS junction are compared with the theory of linear photon-assisted tunneling. Preliminary results from nonlinear measurements are also presented.

6.1 Introduction

In Chapter 5, we discussed the sharp nonlinearity which occurs in the I-V curve of an SIS junction at a voltage $2\Delta/e$, where Δ is the energy gap of the superconductor. If the junction is excited with photons of energy $\hbar\omega$, where $\hbar\omega/e$ is greater than the width of the nonlinearity in the I-V curve, there is a threshold for the absorption of photons which occurs at $\hbar\omega = 2\Delta - eV_o$, where V_o is the bias voltage. This regime is sometimes called the "quantum regime" since the amount of radio-frequency (RF) power absorbed by a voltage-biased junction has a strong dependence on frequency. The component of the quasiparticle current which is in-phase with the applied voltage gives rise to the quantum conductance. The out-of-phase component gives the quantum susceptance. The strong dependence on

frequency of the total admittance of the SIS junction in the quantum regime allows SIS quasiparticle mixers to have conversion gain at microwave frequencies[75, 78].

Previous workers measured the response of SIS junctions in the quantum regime at a single frequency near 80 GHz using CW oscillators. Hu *et al.* made the first measurement of the quantum susceptance[79]. They patterned a planar antenna and an inductive microstrip stub in parallel with a $Nb/AlO_x/Pb$ junction. The parallel combination of the inductive stub and the geometrical capacitance of the junction formed an LC resonator. Using a Fourier-transform spectrometer, they observed small shifts in the resonant frequency as a function of the bias voltage V_o. The existence of the quantum susceptance was deduced from the voltage-dependence of the shift in the resonance frequency. Worsham *et al.* performed a reflection measurement at 80 GHz on an array of two $Nb/AlO_x/Nb$ junctions mounted in a waveguide using a voltage standing wave ratio (VSWR) technique[80]. They deconvolved the junction impedance from the embedding impedance of the waveguide mount and deduced the full voltage-dependence of the quantum conductance and susceptance at 87 GHz.

We have made the first measurement of the quasiparticle response in a $Nb/AlO_x/Nb$ junction over a broad bandwidth from $75 - 200$ GHz. We used a photoconductive switch as a pulsed source of millimeter wave radiation which has broader bandwidth than CW microwave oscillators and has an average power which is two orders of magnitude higher than that of a blackbody source with $T = 1000$ K. The power is sufficiently high such that radiation can be weakly coupled to the SIS junction via an antenna which is impedance-mismatched. Consequently, the quasiparticle response is not significantly broadened by the radiation resistance of the antenna.

Equation (5.19) is an expression for the quasiparticle current which oscillates back and forth across an SIS junction which is excited by a short voltage pulse. Figure 5.6 is a simulation of the quasiparticle response to a voltage pulse from the photoconductive switch described above. In principle, this response could be measured by illuminating an SIS junction with a pulse from the photoconductive switch and measuring the current through the SIS junction with an oscilloscope with < 1 ps temporal resolution. In practice, oscilloscopes with adequate speed and sensitivity for this measurement are not available. The linear response of a stationary system can be measured by using two fast voltage pulses which are separated in time by a variable delay. The voltage pulses interact with the system and are then multiplied together and time-averaged in a correlator. The correlator can be

a square-law detector[81] such as a bolometer which produces an output current which is proportional to the square of the input voltage $I_{out} \propto |V_{in}|^2$.

In the case of the SIS junction, we infer the high-frequency response by measuring the change in the DC current through the junction as a function of the time-delay between the two pulses. The voltage pulses probe the high-frequency conductivity of the junction and the square-law behavior of the junction itself is used as the correlator. An intuitive description of how the pulses interact with the quasiparticle current follows. Consider two equivalent voltage pulses of ~ 1 ps duration which are separated by a variable time-delay. The first pulse incident on the junction causes the quasiparticle current to oscillate back and forth across the junction as was simulated in Fig. 5.6. Assume that the second pulse arrives at the junction after a small time-delay such that the quasiparticle current is still oscillating in response to the first pulse. The second pulse induces an oscillating current which can add constructively or destructively to the current from the the first pulse. If the currents add constructively, there is a large amplitude of oscillation and a correspondingly large square-law signal I_{out}. If the currents add destructively, the oscillations are small and I_{out} is small. By measuring the square-law signal as a function of the time-delay, we indirectly measure the coherent oscillation of the quasiparticle current through the junction.

6.2 Photoconductive switch

The picosecond pulses of millimeter wave radiation were generated by rapidly closing a photoconductive switch which was fabricated at the terminals of a dipole antenna and was biased with a DC voltage. The photoconductive switch can be short-circuited in less than 1 ps by a 100 fs pulse of visible light from a mode-locked laser with photon energy $\hbar\omega > E_g$, where E_g is the bandgap of the photoconductor. The DC bias voltage accelerates the excess carriers and there is a sudden rise in the current flowing between the antenna terminals. In $1-2$ ps, the excess carriers recombine and the current decays rapidly. By the Larmor power formula[82], the radiated RF power is proportional to

$$P_{\mathrm{RF}} \propto \left|\frac{dI}{dt}\right|^2 . \tag{6.1}$$

If the photoconductor is voltage-biased at frequencies ~ 1 THz, then $dI/dt \propto V_{dc}/R(t)$, where $R(t)$ is the time-dependent resistance of the photoconductor. Then the power is

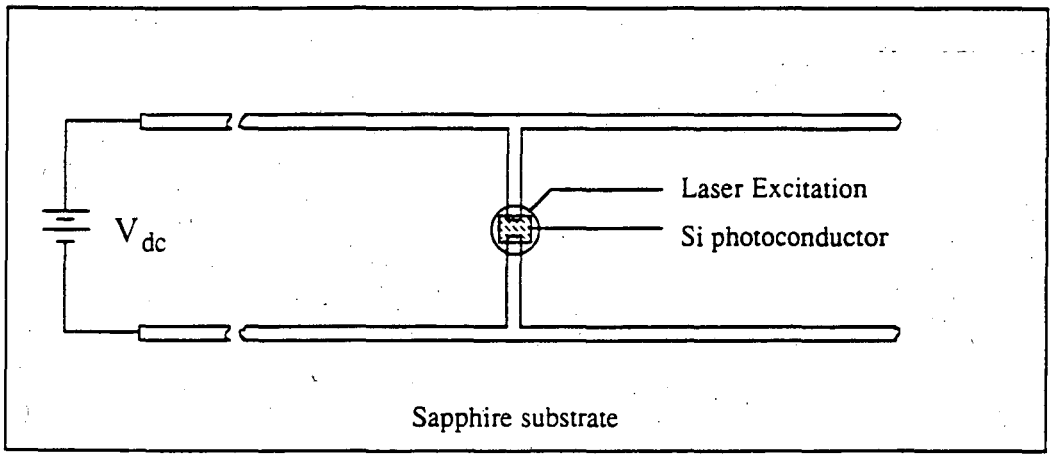

Figure 6.1: Schematic diagram of a photoconductive switch coupled to a dipole antenna fabricated on a silicon-on-sapphire wafer.

proportional to the square of the bias voltage

$$P_{\mathrm{RF}} \propto |V_{dc}|^2 \ . \tag{6.2}$$

Experimentally, we observe that the emitted RF power obeys (6.2).

Silicon photoconductive switches were fabricated on silicon-on-sapphire (SOS) wafers[83, 84]. Figure 6.1 is a schematic diagram of the photoconductive switch coupled to a dipole antenna. The silicon was ion-implanted at doses of $10^{15}\,\mathrm{cm}^{-2}$ with oxygen ions at energies 100 keV and 200 keV. The oxygen impurities are electrically neutral and cause radiation-damage in the silicon which reduces the lifetime of excess carriers. A dipole antenna was patterned in the middle of a 20 mm long transmission line consisting of two parallel aluminum lines of width $10\,\mu$m and separated from each other by $300\,\mu$m. There is a $10\,\mu$m wide gap between the antenna terminals where the ion-damaged silicon was patterned. The photoconductor was excited with a Ti:sapphire laser operating at 800 nm with 100 fs pulses and an average power of 200 mW. The time-averaged power emitted by the photoconductive switch was 68 nW with 40 V of DC bias. The laser pulses repeat at a frequency of 100 MHz and the duty cycle of the millimeter wave pulse is approximately 0.1%. The emitted pulses are nearly a single cycle of electric field oscillation and have a center frequency of 180 GHz and a 3dB bandwidth of 80 GHz.

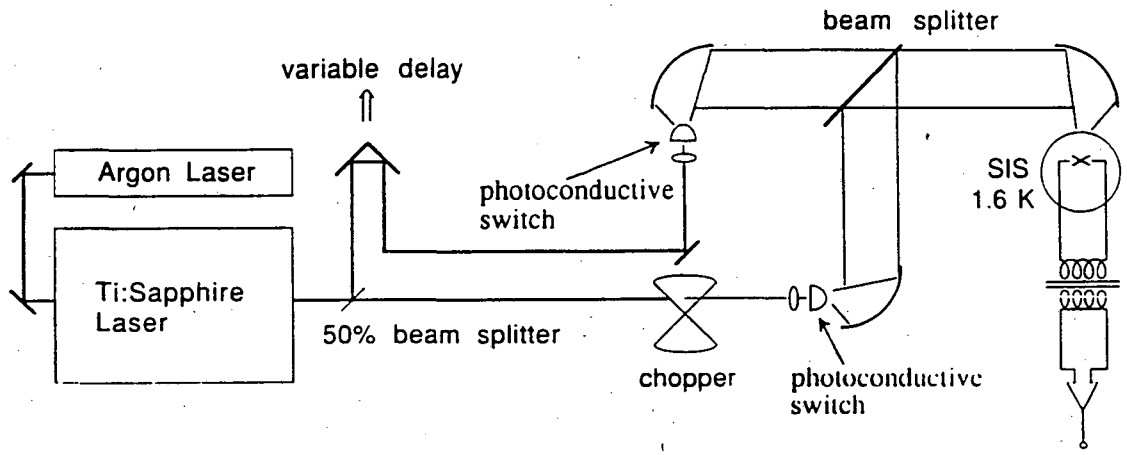

Figure 6.2: Schematic diagram of the millimeter wave interferometer used to measure the high-frequency response of an SIS junction.

6.3 Interferometer

This section discusses the interferometer used to measure the high-frequency response of an SIS junction. First, the interferometer is analyzed for the case of a square-law detector. Then we present calibration data which were measured with a LHe-cooled bolometer as the square-law detector.

Figure 6.2 shows a schematic diagram of an interferometer which illuminates an SIS junction with two pulses of millimeter radiation. A 50% beam splitter divides a 100 fs optical pulse from the Ti:sapphire laser into two pulses, one of which is delayed by a variable amount. Both optical pulses are focused onto nominally identical photoconductive switches, each biased with a variable DC voltage. Each photoconductive switch emits a pulse of millimeter wave radiation which is partially collimated by a 13 mm diameter sapphire hyperhemisphere and then further collimated by an f/1 parabolic mirror with a diameter of 9 cm. The two beams are combined into one with a 175 μm thick Mylar beamsplitter. An f/3 parabolic mirror then focuses the combined beam through a 25 μm thick polypropylene window on a liquid helium cryostat which houses the SIS junction. The cryostat with the SIS junction rests on a kinematic mount and can temporarily be replaced by a cryostat containing a helium-cooled bolometer for calibration measurements.

The interferometer treats the two millimeter wave pulses asymmetrically. One of the pulses transmits through the Mylar beamsplitter while the other pulse reflects off the beamsplitter. The reflected pulse undergoes a phase shift of π relative to the transmitted

pulse in addition to any phase shifts arising from the optical delay line. When the delay time τ between the two optical pulses is zero, the electric field amplitudes of the two millimeter wave pulses are of opposite sign and cancel. We will show that the cross-correlation of the two electric field amplitudes is antisymmetric about $\tau = 0$.

For clarity, we analyze the effect of a single frequency of the millimeter wave pulse propagating through the interferometer. Assume that a square-law detector such as a bolometer replaces the SIS junction in Fig. 6.2. Also, assume the square-law detector absorbs the incident radiation with unity efficiency at all frequencies. The amplitude of the electric field at the square-law detector which reflects from the beamsplitter is $E_1(t) = r_\perp E_1(\omega)e^{-i\omega t}$, where $r_\perp$ is the coefficient for the reflected electric field. The electric field which transmits through the beamsplitter is $E_2(t) = t_\perp E_2(\omega)e^{-i(\omega t+\phi)}$, where $t_\perp$ is the transmission coefficient and $\phi = \omega\tau = 2d\omega/c$ is the phase difference between $E_1(t)$ and $E_2(t)$ caused by a displacement d of the mirror in the optical delay line. The voltage which appears at the output of the square-law detector is proportional to

$$\begin{aligned} |\langle E_1(t) + E_2(t+\tau)\rangle|^2 &= |\langle E_1(t)\rangle|^2 + |\langle E_2(t)\rangle|^2 + \\ &\quad \langle E_1^*(t)E_2(t+\tau)\rangle + \langle E_1(t)E_2^*(t+\tau)\rangle\,, \end{aligned} \tag{6.3}$$

where the bra and ket denote averaging over time

$$\langle E_1^*(t)E_2(t+\tau)\rangle = \lim_{T\to\infty}\int_0^T E_1^*(t)E_2(t+\tau)dt\,. \tag{6.4}$$

Substituting the expressions for $E_1(t)$ and $E_2(t)$ into (6.3) gives

$$\begin{aligned} |\langle E_1(t) + E_2(t+\tau)\rangle|^2 &= |\langle E_1(\omega)\rangle|^2\,|r_\perp|^2 + |\langle E_2(\omega)\rangle|^2\,|t_\perp|^2 + \\ &\quad \langle E_1(\omega)E_2(\omega)\rangle\left(r_\perp^* t_\perp e^{-i\phi} + r_\perp t_\perp^* e^{i\phi}\right)\,. \end{aligned} \tag{6.5}$$

Expressions for $r_\perp$ and $t_\perp$ for p-polarized radiation incident on a dielectric membrane are:

$$\begin{aligned} r_\perp &= \frac{r_{12} + r_{23}e^{i2\beta}}{1 + r_{12}r_{23}e^{i2\beta}} \\ t_\perp &= \frac{t_{12} + t_{23}e^{i\beta}}{1 + r_{12}r_{23}e^{i2\beta}}\,, \end{aligned} \tag{6.6}$$

where $\beta = (\omega/c)nd\cos\theta_2$, $\sin\theta_2 = n^{-1}\sin\theta_1$, and θ_1 is the angle of incidence measured from the normal of the plane of the beamsplitter. The quantities r_{ij} and t_{ij} are the Fresnel coefficients for the vacuum/Mylar interfaces[85]

$$r_{12} = \frac{\cos\theta_1 - n\cos\theta_2}{\cos\theta_1 + n\cos\theta_2}$$

$$\begin{aligned} r_{23} &= \frac{n\cos\theta_2 - \cos\theta_1}{n\cos\theta_2 + \cos\theta_1} \\ t_{12} &= \frac{2\cos\theta_1}{\cos\theta_1 + n\cos\theta_2} \\ t_{23} &= \frac{2n\cos\theta_2}{n\cos\theta_2 + \cos\theta_1} . \end{aligned} \tag{6.7}$$

where $n = 1.85$ is the index of refraction of Mylar for millimeter wavelengths[86]. High-frequency losses in the Mylar beamsplitter are neglected. Numerical calculations of the quantities $r_\perp t_\perp^*$ and $r_\perp^* t_\perp$ indicate the following:

$$\begin{aligned} Re[r_\perp^* t_\perp] &= Re[r_\perp t_\perp^*] = 0 \\ Im[r_\perp^* t_\perp] &= -Im[r_\perp t_\perp^*] \neq 0 . \end{aligned} \tag{6.8}$$

Figure 6.3 shows the beam splitter efficiency $2Im[r_\perp t_\perp^*]$ plotted as a function of frequency for a Mylar beamsplitter with thickness 175 μm and $\theta_1 = \pi/4$. This beamsplitter has useful efficiency from 50 – 450 GHz. Substitution of (6.8) into (6.5) gives

$$\begin{aligned} |\langle E_1(t) + E_2(t+\tau)\rangle|^2 &= |\langle E_1(\omega)\rangle|^2 |r_\perp|^2 + |\langle E_2(\omega)\rangle|^2 |t_\perp|^2 + \\ &\quad 2\langle E_1(\omega) E_2(\omega)\rangle Im[r_\perp t_\perp^*] \sin\phi . \end{aligned} \tag{6.9}$$

Equation (6.9) can be generalized for the case when $E_1(t)$ and $E_2(t)$ are comprised of photons with many different frequencies ω. Then, application of the Wiener-Khintchine theorem[81] gives

$$\begin{aligned} |\langle E_1(t) + E_2(t+\tau)\rangle|^2 &= \frac{1}{2\pi}\int_{-\infty}^{\infty} d\omega \left\{ |\langle E_1(\omega)\rangle|^2 |r_\perp|^2 + |\langle E_2(\omega)\rangle|^2 |t_\perp|^2 + \right. \\ &\quad \left. 2\langle E_1(\omega) E_2(\omega)\rangle Im[r_\perp t_\perp^*] \sin(\omega\tau) \right\} . \end{aligned} \tag{6.10}$$

Equation (6.10) shows we can measure the power spectrum of the absorbed electric field as a function of frequency by monitoring the output of the square-law detector as a function of time delay $\tau = 2d/c$ and calculating its sine Fourier transform.

$$\langle E_1(\omega) E_2(\omega)\rangle = (Im[r_\perp t_\perp^*])^{-1} \int_0^\infty Re[\langle E_1^*(t) E_2(t+\tau)\rangle] \sin(\omega\tau) d\tau . \tag{6.11}$$

The operation of conventional Fourier transform spectrometers (FTS) is based on an equation similar to (6.11) but with $\sin(\omega\tau)$ replaced by $\cos(\omega\tau)$ and $Im[r_\perp t_\perp^*]$ replaced by $|r_\perp t_\perp^*|^2$. These changes are a result of the symmetric design used for most FTS's. In

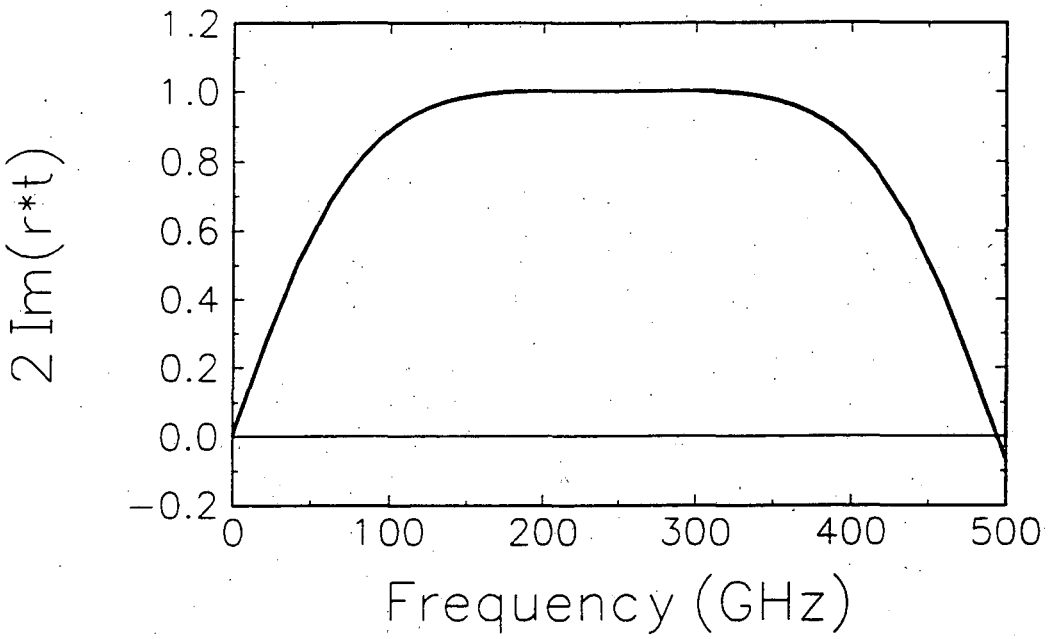

Figure 6.3: Beam splitter efficiency $2Im[r_\perp t_\perp^*]$ plotted as a function of frequency for a Mylar beamsplitter with thickness 175 μm and $\theta_1 = \pi/4$. This beamsplitter has useful efficiency from $50 - 450$ GHz.

an FTS, a single radiation source emits light which is divided by the beamsplitter into two components, each of which transmits and reflects off the beamsplitter. In principle, the FTS and the interferometer in Fig. 6.2 give equivalent information when used for linear spectroscopy. Section 6.7 discusses how the sine-symmetry of the interferometer used in this work has advantages for making nonlinear measurements.

The first measurements using the interferometer were made for calibration of the photoconductive switches. The cryostat housing the SIS junction in Fig. 6.2 was replaced with a cryostat containing a composite bolometer which operates at $T = 1.6$ K. The bolometer was designed for measurements with low background power. Its spectral range is restricted to frequencies < 600 GHz by a cooled low-pass filter of fluorogold which prevents 300 K thermal radiation from saturating the bolometer. The DC voltage across each photoconductive switch was adjusted until the RF power in each arm of the interferometer was the same. The intensity of one of the visible beams from the laser was modulated at 10 Hz with a chopper wheel and a lock-in amplifier measured the signal from the bolometer. Figure 6.4a shows the signal at the output of the lock-in amplifier plotted as a function of the mirror

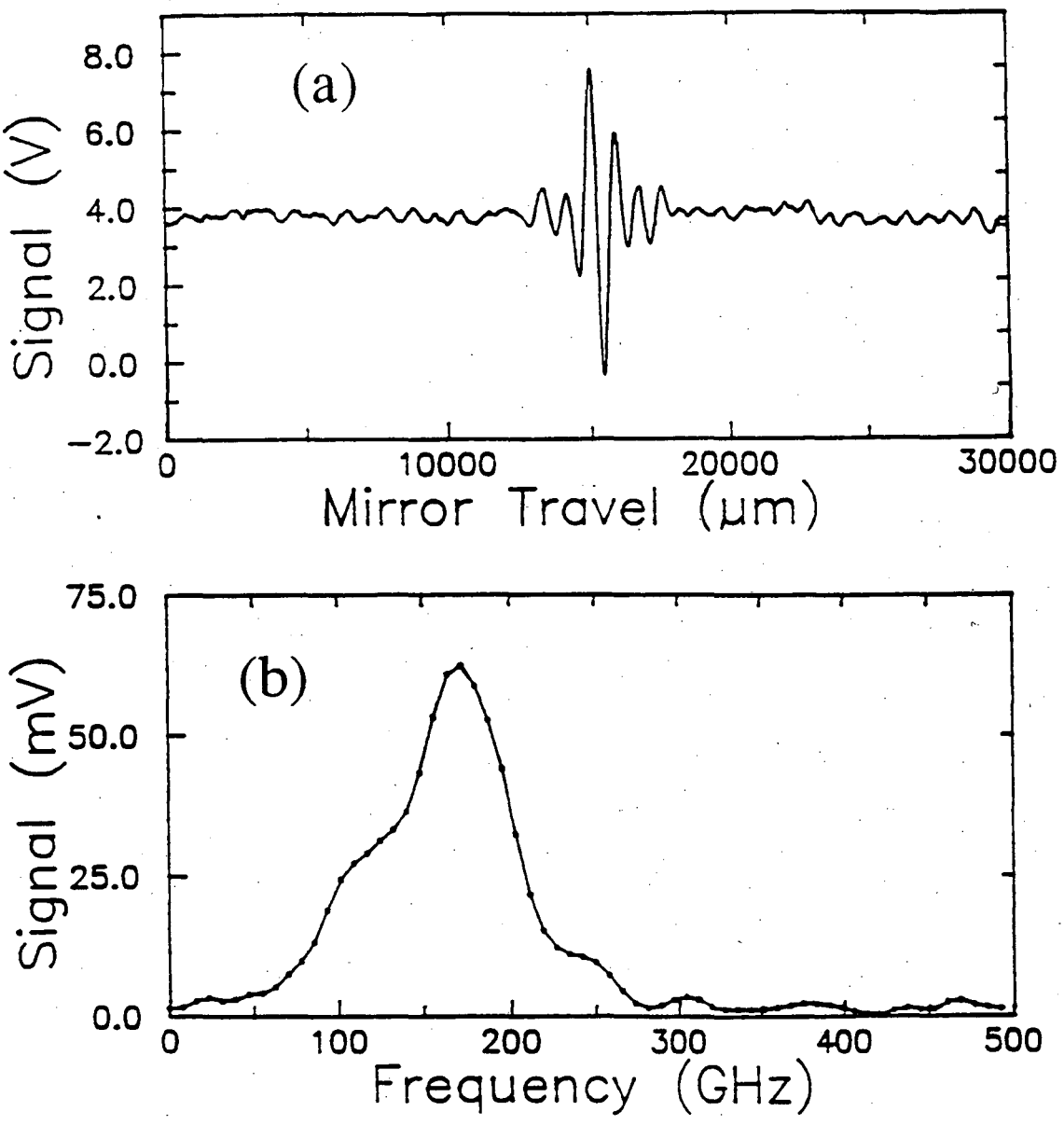

Figure 6.4: Measurements using the interferometer in Fig. 6.2 using a bolometer in place of the SIS junction. (a) Bolometer signal plotted as a function of mirror displacement in the delay line. (b) Amplitude of the Fourier-transform of the interferogram. The spectral power of the photoconductive switches peaks at 180 GHz and has an $\sim$ 80 GHz bandwidth

displacement d. A null appears in the interferogram at zero time-delay ($d = 1550\,\mu$m). Here, the electric fields have a phase difference of π and cancel. For time delays $|\tau| > 0$, the interferogram has sine-symmetry. The power spectrum calculated from the Fourier transform of Fig. 6.4a is shown in Fig. 6.4b. The spectral power peaks at 180 GHz and the bandwidth between the -3 dB points is ~ 80 GHz. Comparison with Fig. 6.3 indicates the beamsplitter efficiency is roughly constant over the bandwidth of the photoconductive switch. The small structure in the spectrum of Fig. 6.4 may arise from interference effects related to the coupling of the Winston cone to the quasioptical system.

6.4 SIS junction fabrication

The SIS junctions were fabricated at Conductus, Inc. with a Nb trilayer process[87] which is primarily used for fabricating digital circuits based on Josephson junctions. Figure 6.5 shows a schematic cross-section of such a junction. The Nb trilayer is deposited *in situ*. First, the Nb counter electrode is sputtered onto a silicon wafer of 4" diameter. Next, a thin aluminum film is deposited and oxidized to form the insulating tunnel barrier. The top Nb electrode is then deposited and selectively anodized to define the junction area. A layer of SiO_2 is deposited for electrical isolation. Finally, a Nb "wire-up" layer is deposited which serves as one terminal of a planar log-periodic antenna. The counter electrode forms the other antenna terminal.

A typical junction has a $2 \times 2\,\mu$m area and a critical current density of $5 \times 10^3\,\mathrm{A\,cm^{-2}}$. The capacitance is $C \approx 200$ fF and $R_N = 14\,\Omega$. For a frequency $\omega/2\pi = 180$ GHz, the product $\omega R_N C \approx 3$ gives an indication of the amount of RF power which is shunted through the geometric capacitance C. A magnetic field of about 100 G cancels the Cooper pair tunneling current and allows us to isolate the quasiparticle tunneling current.

6.5 Video detector response

The nonlinearity in the I-V curve of the SIS junction leads to frequency conversion. In the case of video detection, an RF voltage V_ω of angular frequency ω is converted to a DC current. For RF voltages with $eV_\omega/\hbar\omega \ll 1$, video detection in an SIS junction has a square-law behavior. A sharp nonlinearity leads to efficient conversion from RF to DC. The current responsivity—defined as the induced DC current per unit RF power incident on the

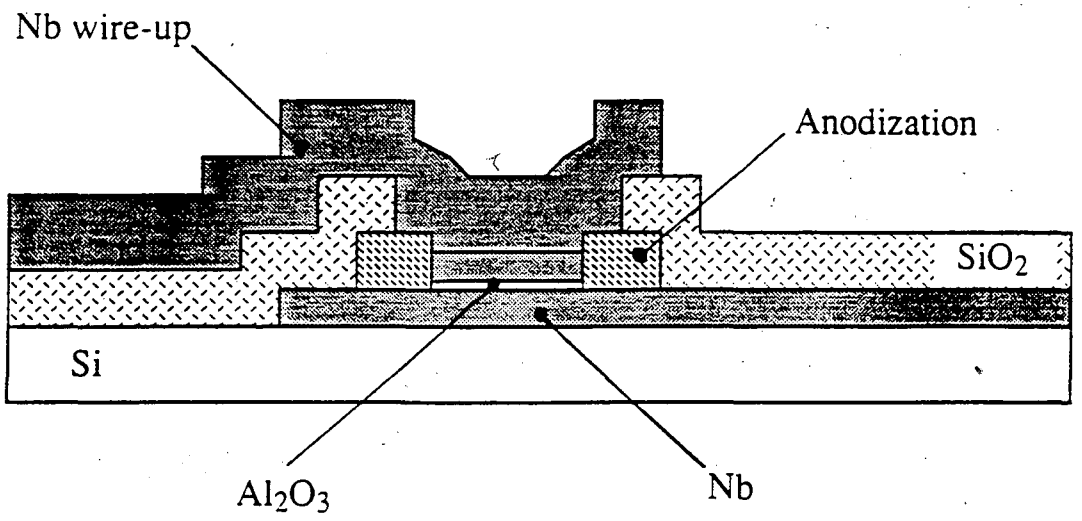

Figure 6.5: Schematic diagram of the cross-section of a $Nb/AlO_x/Nb$ trilayer junction fabricated at Conductus, Inc.

junction—is a measure of the conversion efficiency of an SIS video detector. Tucker derived the following expression by using the equations presented in Chapter 5 in the small-signal limit $eV_\omega/\hbar\omega \ll 1$

$$S_I(\omega) = \frac{\Delta I_{DC}}{P_{RF}} = \frac{e}{\hbar\omega}\frac{I_{DC}(V_o + \hbar\omega/e) - 2I_{DC}(V_o) + I_{DC}(V_o - \hbar\omega/e)}{I_{DC}(V_o + \hbar\omega/e) - I_{DC}(V_o - \hbar\omega/e)}C_{RF}\,. \tag{6.12}$$

The RF coupling coefficient is

$$C_{RF} = 1 - \left|\frac{Y_A - Y_J^*}{Y_A + Y_J}\right|^2\,, \tag{6.13}$$

where Y_J is the junction admittance and Y_A is the antenna admittance. The expression for $S_I(\omega)$ in (6.12) reduces to the classical expression

$$S_I(\omega) = \frac{1}{2}\frac{d^2I_{DC}/dV_o^2}{dI_{DC}/dV_o}C_{RF}\,, \tag{6.14}$$

in the limit of small ω where

$$(e/2\hbar\omega)(I_{DC}[V_o + \hbar\omega/e] - I_{DC}[V_o - \hbar\omega/e]) = \frac{dI_{DC}}{dV_o}\,. \tag{6.15}$$

The admittance of an SIS junction with capacitance C can be written as $Y_J = G_q + i(B_q + \omega C)$. The quantum conductance G_q and the quantum susceptance B_q can be calculated from the DC I-V curve and from the Kramers-Kronig transform $I_{KK}(V)$ of the

DC I-V curve, respectively [75].

$$G_q = \frac{e}{2\hbar\omega}[I_{DC}(V_o + \hbar\omega/e) - I_{DC}(V_o - \hbar\omega/e)] \quad (6.16)$$

$$B_q = \frac{e}{2\hbar\omega}[I_{KK}(V_o + \hbar\omega/e) - 2I_{KK}(V_o) + I_{KK}(V_o - \hbar\omega/e)] \; . \quad (6.17)$$

In the small-signal limit, processes involving the absorption of single photons dominate the response. The induced DC current ΔI_{DC} is proportional to $P_{RF}(\omega)$. The response of an SIS junction to a pulse of RF power can then be calculated by adding the values of ΔI_{DC} computed using (6.12) for each frequency component in the pulse. At large signal levels $eV_\omega/\hbar\omega \approx 1$, multiple-photon absorption processes are important and the broad-band response is best calculated using the time-domain formulation (5.19).

We used a photoconductive switch to illuminate an SIS junction with pulses of RF power at a repetition rate of 100 MHz. Figure 6.6 shows the time-averaged video response plotted as a function of V_o for two values of RF power. Consider the curve measured with $4.2\,\mu$W of RF power. For $V_o < 1.5\,$mV, there is no discernible video signal since only photons in the pulse in Fig. 6.4 with frequency $\omega/2\pi > (2\Delta - V_o)/h \approx 300\,$GHz contribute to single-photon absorption. For $V_o = 2.5\,$mV, there is a peak in the video response. This peak occurs at a lower frequency $(2\Delta - V_o)/h \approx 60\,$GHz than the frequency of the peak in Fig. 6.4 because of the frequency-dependence of $S_I(\omega)$. The factors $e/\hbar\omega$ and C_{RF} in (6.12) reduce $S_I(\omega)$ when the frequency is increased. For bias voltages larger than the gap voltage $V_o > 2.75\,$mV, the video response is negative. The negative video response arises from stimulated emission of photons from occupied quasiparticle states in the "conduction band" of the right side of the junction in Fig. 5.1. These states are occupied because of DC injection of quasiparticles across the junction which occurs for $eV_o > 2\Delta$.

The video response for $4.2\,\mu$W of RF power has been multiplied by the ratio of the RF powers $68/4.2 = 16$. If the video response were linear in power, the two curves would be identical. The near overlap of the two curves for $2.3 < V_o < 2.7\,$mV indicates that the video response is nearly linear in power from $4.2\,\mu$W to $68\,\mu$W. At lower voltages, the curves no longer overlap. There is more signal at $V_o = 2\,$mV for the $68\,\mu$W curve than a linear extrapolation in power from the $4.2\,\mu$W curve predicts. The excess signal arises from nonlinear absorption processes where two or more photons coherently interact with a quasiparticle and cause it to tunnel. For example, two 90 GHz photons could cause a quasiparticle to tunnel when $(2\Delta - eV_o)/h = 180\,$GHz. The difference in shape of the two curves in Fig. 6.6 shows that the photoconductive switch has sufficient power for studying

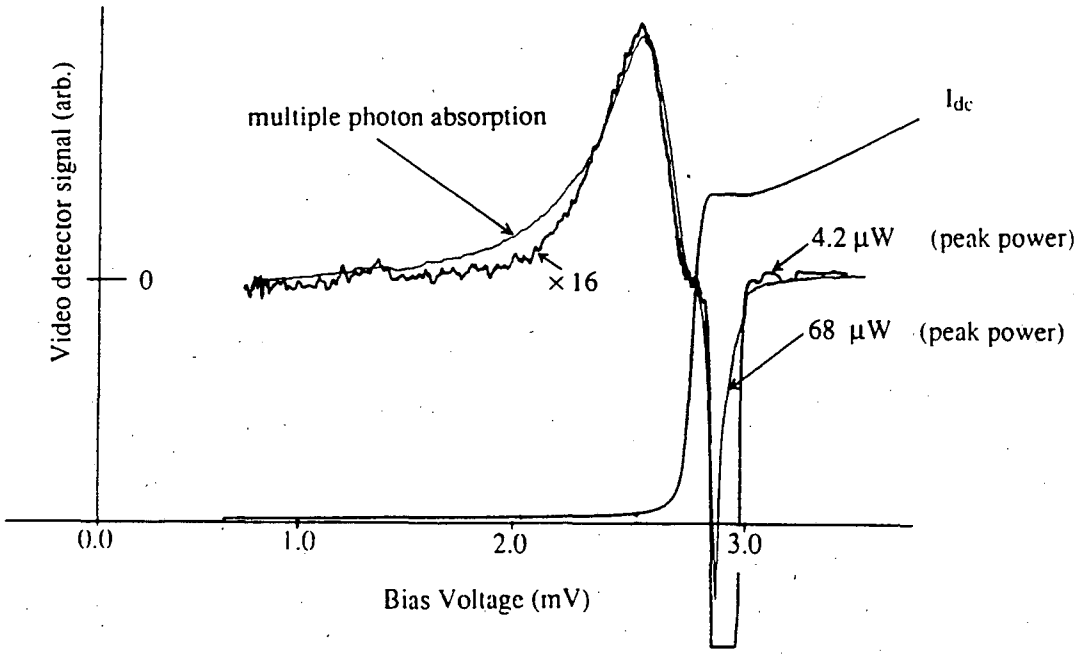

Figure 6.6: Video detector response of a Nb SIS junction to a single RF pulse from a photoconductive switch. The video response for two values of the peak power in the RF pulse is plotted as a function of the bias voltage V_o across the SIS junction.

the nonlinear response of the SIS junction.

6.6 Time-domain data

We placed the SIS cryostat in the interferometer and adjusted the bias voltage on the photoconductive switches until the peak RF power from each arm of the interferometer was $\sim 1\,\mu$W. The beam in one of the arms was modulated at 1 KHz. The signal from the SIS junction was coupled through a 300 K transformer to a low-noise FET amplifier with a spot noise referred to the SIS junction of $0.2\,\mathrm{nV/Hz^{1/2}}$ at 1 kHz. Figure 6.7a shows the average video signal of the SIS junction measured as a function of time-delay between the two RF pulses. At this power, the video signal was proportional to the RF power for $V_o = 2.2\,\mathrm{mV}$ and there was an adequate ratio of signal to noise. Each interferogram was measured for approximately 15 minutes. Curves corresponding to different values of V_o are offset for clarity. A null appears in the data at zero delay since the electric fields which couple to the antenna cancel. The oscillations at non-zero delays result from the coherent tunneling of quasiparticles in the quantum regime. Figure 6.7b shows the amplitude of the

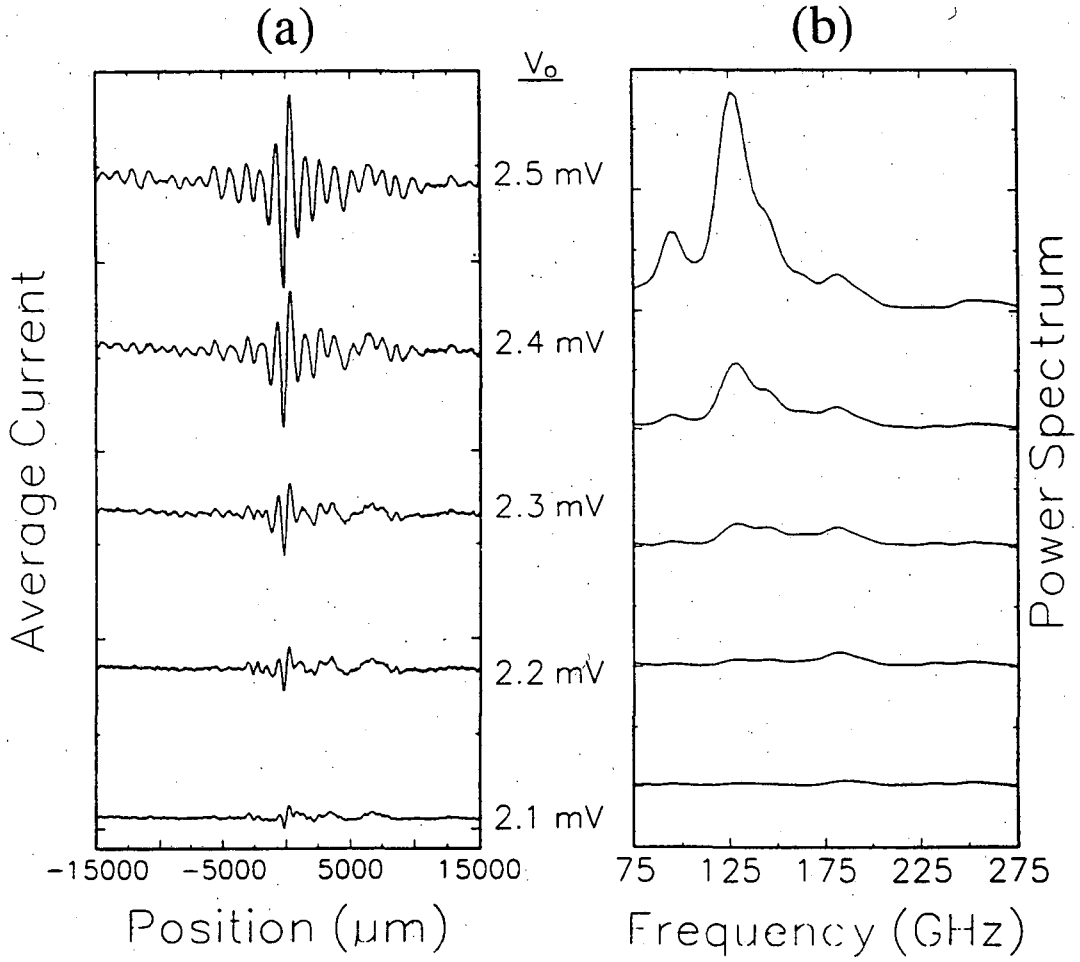

Figure 6.7: (a) Shift in the DC quasiparticle current ΔI_{DC} generated by two pulses of millimeter radiation plotted as a function of the time-delay between the pulses. (b) Amplitude of the Fourier transforms of the data in (a).

Fourier transforms of the cross-correlations in Fig. 6.7a. As V_o is reduced from 2.5 mV, the threshold frequency $(2\Delta - eV_o)/h$ increases and the amplitude of low-frequency oscillations decreases while high frequency oscillations persist. The small structure in the power spectra results from interference effects in coupling the electrical pulses through the optical system and onto the log-periodic antenna in the cryostat.

It is difficult to make direct comparisons between the data in Fig. 6.7 and the theory in Chapter 5. To simulate the data, the theory requires detailed knowledge of the RF pulses and of the coupling between the log-periodic antenna and the quasi-optical system. In the small-signal limit where the video response is linear in power, one can compare

ratios of the spectra in Fig. 6.7b for different V_o with calculated ratios of $\Delta I_{DC}(\omega, V_o) = S_I(\omega, V_o)P_{RF}(\omega)$. Many details of the RF pulse cancel out of the ratios. The current responsivity (6.12) can be calculated from the DC I-V curve if C and Y_A are known. The capacitance C is $\sim$ 200 fF. The antenna admittance Y_A can be a source of uncertainty. The log-periodic antenna belongs to a special class of planar antennas referred to as "self-complementary" antennas, in which the pattern of the metallic part is the same as that of the dielectric part. The admittance Y_A of self-complementary antennas made with a lossless conductor on a semi-infinite substrate with no sources of reflection is[88]

$$Y_A = 3.74 \times 10^{-3}(1 + \epsilon_r)^{1/2}\,\Omega^{-1}\,, \tag{6.18}$$

where ϵ_r is the relative dielectric constant of the substrate. For a log-periodic antenna on a Si substrate, $\epsilon_r = 11.9$ for millimeter waves[86] and $Y_A = (75\,\Omega)^{-1}$. Measurements by Nahum *et al.* suggest that the beam pattern depends on frequency[89]. The portion of the beam which does not couple out of the cryostat can reflect off the interior walls and make Y_A dependent on frequency.

The antenna was designed to be impedance-mismatched to the SIS junction. The impedance-mismatch provides some cancellation of Y_A in the ratios of the spectra. At 120 GHz, the admittance of the junction is $\sim (7\,\Omega)^{-1}$ while the nominal antenna admittance is $(75\,\Omega)^{-1}$. Equation (6.13) for C_{RF} can be expanded in terms of Y_A/Y_J, where $|Y_A/Y_J| \approx 0.1$. The result to first order is $C_{RF} \approx 4Re[Y_A/Y_J^*]$. The contribution of Y_A to the ratios of spectra with different V_o cancels if Y_A is real. The cancellation is imperfect if Y_A has an imaginary component.

The symbols in Fig. 6.8 show ratios of the spectra in Fig. 6.7b to the spectrum measured with $V_o = 2.5$ mV. The data show an absorption edge which scales with the frequency $(2\Delta - eV_o)/h$. The solid lines are calculated from equations (6.12)-(6.17) using the DC I-V curve measured at $T = 1.6$ K. We assumed a real antenna admittance $Y_A = (75\Omega)^{-1}$ and that the junction capacitance was $C = 200$ fF. No fitting parameters were varied in calculating the solid lines. The calculated lines are in agreement with the data for $2.1 \leq V_o \leq 2.3$ mV. The data for $V_o = 2.4$ mV fall slightly below the theoretical curve. For frequencies less than $\sim$ 170 GHz, the structure in the ratios is reproducible and may arise from interference effects in the quasioptical system. For frequencies $>$ 170 GHz, the video signal is small and amplifier noise contributes to the structure in the ratios for the following reasons. First, the RF power was kept small in these measurements so the SIS junction

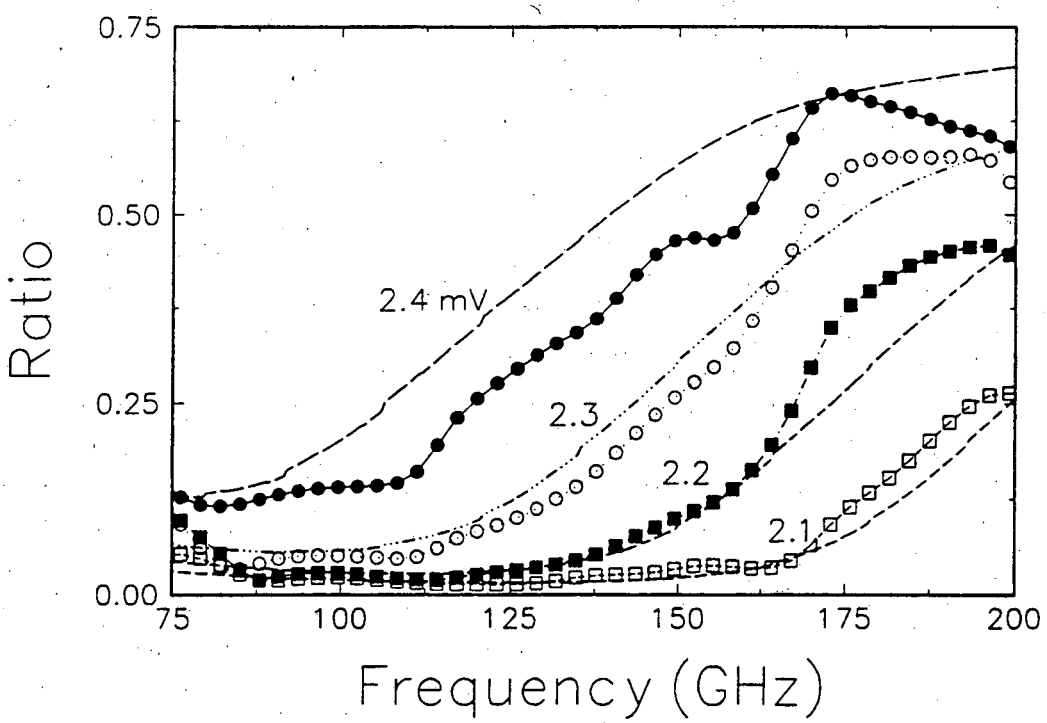

Figure 6.8: The symbols are ratios of the spectra shown in Fig. 6.7b to the spectrum measured with $V_o = 2.5\,\mathrm{mV}$. Solid lines show calculations from linear theory of photon-assisted tunneling.

would respond linearly. Second, the duty cycle of the photoconductive switches was 0.1% but the preamplifier measured the signal from the SIS junction with a duty cycle of 100%. The signal-to-noise ratio could be improved by using a box car averager which operates at a repetition rate of 100 MHz.

6.7 Nonlinear response

The previous section presented measurements in the time-domain of the linear response of the quasiparticle current to an RF pulse. In principle, linear spectroscopy can be done in either the time-domain or in the frequency-domain. For example, a Gunn oscillator which is tunable over the bandwidth of the photoconductive switch could be used to measure the data in Fig. 6.8 without using an interferometer. In practice, broad-band measurements with tunable CW oscillators can be difficult because of interference effects. Sometimes these effects can be avoided by averaging the CW signal over many frequencies. Nonetheless, in

measuring the linear response spectrum we have not used the unique capability of the photoconductive switch to provide short temporal pulses of millimeter waves. We have only exploited the brightness and broad bandwidth of the source. In this section, we discuss a nonlinear measurement of the quasiparticle response which uses the short pulse to obtain information about the quasiparticle lifetime.

Consider the interaction between a photon with energy $\hbar\omega > 2\Delta - eV_o$ and a quasiparticle excitation. According to the theory of Cohen, Falicov, and Phillips[72], if the photon is absorbed, the quasiparticle oscillates with frequency $\omega/2\pi$ back and forth across the junction forever. The infinite lifetime is manifested in the delta-function in the spectral distribution function (5.12) for a quasiparticle. In this theory, the impulse response of the junction shown in Fig. 5.4 decays only because many quasiparticles are excited, each with a slightly different energy. The quasiparticle oscillations then dephase in a time τ_2 and the total current flowing through the junction averages to zero. The theory, however, assumes that the quasiparticles are still excited. The finite lifetime of the quasiparticle can be calculated using BCS strong-coupling theory. Kaplan *et al.*[90] calculated values for the quasiparticle lifetime in various bulk superconductors using data for $\alpha^2F(\Omega)$. Here, α is the matrix element for the electron-phonon interaction and $F(\Omega)$ is the phonon density of states. The results of the strong-coupling calculation indicate that a quasiparticle excitation with energy $\xi_k > \Delta$ has two lifetimes. In a short time τ_{qp2}, the quasiparticle emits phonons and scatters to the gap-edge $\xi_k = \Delta$. In a longer time τ_{qp1}, the quasiparticle scatters with another quasiparticle of opposite spin and momentum, emits a phonon of energy $\sim 2\Delta$, and relaxes to the BCS ground state. Both times τ_{qp1} and τ_{qp2} depend on the temperature of the superconductor and on the density of quasiparticles. Dynes *et al.* deduced information about the quasiparticle lifetime from the temperature-dependence of the DC I-V curve for a tunnel junction made from a Pb:Bi alloy[91]. This technique requires an SIS junction with an extremely sharp onset in current at $2\Delta/e$ and has poor sensitivity for $T < 0.5T_c$.

The data in Fig. 6.7 are proportional to the first order correlation function

$$\begin{aligned} g^{(1)}(\tau) &= \langle E^*(t)E(t+\tau)\rangle + C.C. \\ &\propto \langle I^*(t)I(t+\tau)\rangle + C.C., \end{aligned} \tag{6.19}$$

where $E(t)$ and $I(t)$ are the local electric field and current across the junction, respectively. The function $g^{(1)}(\tau)$ measures how long the quasiparticle current oscillates coherently in response to a voltage pulse. The coherence time τ_c measured by $g^{(1)}(\tau)$ is

$\tau_c^{-1} \approx \tau_2^{-1} + (2\tau_{qp1})^{-1} + (2\tau_{qp2})^{-1}$. The lifetimes which determine τ_c cannot be measured independently with linear spectroscopy. Researchers in laser spectroscopy have devised nonlinear techniques which can separate these lifetimes. Some examples are pump-probe, spectral hole-burning, and transient four-wave mixing techniques such as photon-echoes[92]. All these techniques measure higher order correlation functions than $g^{(1)}(\tau)$. The samples are usually measured using laser beams with opposite polarizations or with different directions of propagation to avoid the large background signal resulting from $g^{(1)}(\tau)$.

The second-order correlation function $g^{(2)}(\tau)$ contains information on the lifetimes.

$$g^{(2)}(\tau) = \langle E^*(t)E^*(t)E(t+\tau)E(t+\tau)\rangle + \langle E^*(t)E(t)E^*(t+\tau)E(t+\tau)\rangle + C.C. \quad (6.20)$$

The signal for $g^{(2)}(\tau)$ is higher order in the interaction between photons and quasiparticles than the signal for $g^{(1)}(\tau)$. Therefore, $g^{(2)}(\tau) \ll g^{(1)}(\tau)$ and it is difficult to measure $g^{(2)}(\tau)$ unless some procedure is used to reduce the contribution from $g^{(1)}(\tau)$. The SIS junction is much smaller than a millimeter wavelength and is antenna-coupled. The antenna couples to light of a single spatial mode and of one polarization. Therefore, the contribution from $g^{(1)}(\tau)$ cannot be reduced by using opposite polarizations or beams with different propagation vectors. We will argue that the sine-symmetry of the signal for $g^{(1)}(\tau)$ in our interferometer allows us to measure $g^{(2)}(\tau)$ independently.

Detailed discussions of $g^{(2)}(\tau)$ exist in textbooks on nonlinear optics[19, 92]. Some of the basic results are reproduced here. The first term in (6.20) and its complex conjugate can be reduced[19] to $|g^{(1)}(\tau)|^2$. These terms only provide information about the coherence time τ_c. The second term in (6.20) and its complex conjugate are closely related to the intensity autocorrelation function[93]. If the junction absorbs a pulse of photons at $t = 0$, these terms measure how long the absorption of additional photons from a second pulse is correlated with the first pulse. For example, if 80% of the available quasiparticle states are occupied after the first pulse, additional excitation of quasiparticles by the second pulse will be suppressed until a recombination time τ_{qp1} has elapsed and the states are vacant.

In section 6.3 we showed that the signal corresponding to $g^{(1)}(\tau)$ can be measured when the video response of the SIS junction is a square-law process. Because of the asymmetry of the interferometer, the beam splitter efficiency is $2Im[r_\perp^* t_\perp]$ and $g^{(1)}(\tau)$ has sine-symmetry. At higher levels of RF power than were used for measuring the linear response, the video response has a higher order contribution from fourth-law detection $I_{out} \propto |V_{in}|^4$. This term in the video response results in a term in the interferometer data

which is proportional to

$$|\langle E_1(t) + E_2(t+\tau)\rangle|^4 \ . \tag{6.21}$$

Expanding (6.21) gives the terms in $g^{(2)}(\tau)$, all of which are multiplied by the coefficient $|r_\perp^* t_\perp|^2 \cos(2\omega\tau)$. Hence, the terms corresponding to $g^{(2)}(\tau)$ have cosine-symmetry while the terms corresponding to $g^{(1)}(\tau)$ have sine-symmetry. If the interferometer is carefully aligned, $g^{(2)}(\tau)$ can be separated from $g^{(1)}(\tau)$ by subtracting the data which are sine-symmetric from the interferogram.

Figure 6.9 shows preliminary data for both the sine-symmetric and cosine-symmetric parts of measured interferograms. These data were collected at various levels of RF power with the SIS junction at $T = 1.6$ K. These data have not been analyzed in detail, but some comments are appropriate. The curves in Fig. 6.9 are offset by an additive constant. The magnitude of the cosine-symmetric data is much smaller than that of the sine-symmetric data. The difference in magnitudes is consistent with interpreting the cosine-symmetric data as a higher-order correlation. We assume that the effect of increasing the RF power is to increase the density of excited quasiparticles. The magnitude of the sine-symmetric data is roughly proportional to the RF power but the shape does not change significantly. If the sine-symmetric data are a measure of $g^{(1)}(\tau)$, the constant shape indicates that the coherence time τ_c of the quasiparticle oscillation does not depend strongly on the density of quasiparticles. The cosine-symmetric data change in both magnitude and shape as the RF power is increased above 4.6 μW. If these data represent $g^{(2)}(\tau)$, the change in shape may indicate that the quasiparticle lifetimes τ_{qp1} and τ_{qp2} depend on the density of excited quasiparticles for RF powers $> 4.6\,\mu$W. Future experiments will measure data similar to Fig. 6.9 as a function of V_o and temperature T. A detailed fit of the cosine-symmetric data to a phenomenological form for $g^{(2)}(\tau)$ may provide values for the quasiparticle lifetime as a function of V_o and T.

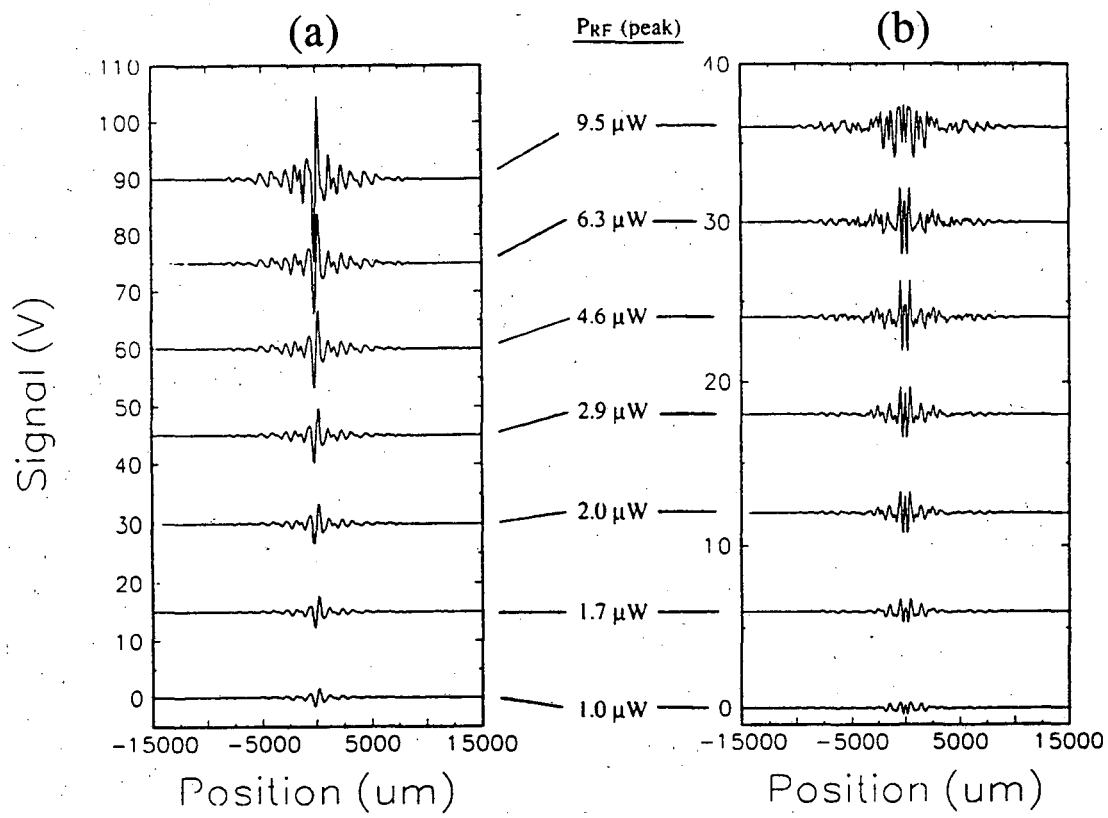

Figure 6.9: (a) Sine-symmetric part of an interferogram measured at various levels of RF power with $V_o = 2.4\,\mathrm{mV}$. These data are proportional to $g^{(1)}(\tau)$. (b) Cosine-symmetric part of the interferogram measured at various levels of RF power with $V_o = 2.4\,\mathrm{mV}$. These data are proportional to $g^{(2)}(\tau)$.

Bibliography

[1] F. J. Low, *J. Opt. Soc. Am.* **51**, 1300 (1961).

[2] J. Clarke, G. I. Hoffer, P. L. Richards, N-H. Yeh, *J. Appl. Phys.* **48**, 4865 (1977).

[3] A. E. Lange, E. Kreysa, S. E. McBride, P. L. Richards, *Int. J. Infrared and Millimeter Waves* **4**, 689 (1983).

[4] S. Verghese, P. L. Richards, S. A. Sachtjen, K. Char, submitted to *Appl. Phys. Lett.*

[5] J. C. Brasunas, V. Kunde, B. Lakew, S. H. Moseley, *SPIE Proceedings* **1292**, 155 (1990).

[6] S. Verghese, P. L. Richards, K. Char, D. K. Fork, T. H. Geballe, *J. Appl. Phys.* **71**, 2491 (1992).

[7] R. A. Smith, F. E. Jones, and R. P. Chasmar, *The Detection and Measurement of Infrared Radiation*, 2nd ed. (Oxford U. P., Oxford 1968).

[8] For a non-equilibrium treatment of thermal fluctuations in bolometers see: J. C. Mather, *Appl. Optics* **21**, 1125 (1982); J. C. Mather, *Appl. Optics* **23**, 3181 (1984).

[9] See, for example, the P-41 detector, Molectron Corp., Sunnyvale, CA.

[10] P. L. Richards, "A look at the theory of photon noise," *unpublished.*

[11] E. Jakeman, E. R. Pike, *J. Phys. A.* **1**, 128 (1968).

[12] R. Hanbury Brown, R. Q. Twiss *Proc. R. Soc. London Ser. A* **243**, 291 (1958).

[13] E. Jakeman, C. J. Oliver, E. R. Pike, *J. Phys. A.* **1**, 406 (1968).

[14] A. Kastler, *Compte Rendu de la 3ème Conférence Internationale d'Electronique Quantique*, P. Grivet, N. Bloembergen, Eds., 4 (Paris, 1964); For a treatment of spatial coherence effects see J. M. Lamarre, *Appl. Optics* **25**, 870 (1986).

[15] B. R. Martin *Statistics for Physicists*, (Academic Press, London 1971).

[16] Y. Yamamoto, H. A. Haus, *Rev. Mod. Phys.* **58**, 1001 (1986).

[17] C. M. Caves, *Phys. Rev. D* **26**, 1817 (1982).

[18] W. Schockley, J. Pierce, *Proc. IRE* **26**, 321 (1938).

[19] R. Loudon, *The quantum theory of light*, 2nd ed. (Oxford U. P., Oxford 1983).

[20] F. Capasso, *IEEE Trans. Electron Dev.* **ED-30**, 381 (1983).

[21] L. Xizhi, Y. Caibing, C. Xiaoneng, F. Xizeng, S. Xiangqing, L. Shuqin, X. Yizhi, Z. Bairu, Y. Caiwen, Z. Yinzi, Z. Yuying, L. Yong, W. Huisheg, S. Yinhuan, G. Ju, L. Lin, *Int. J. Infrared and Millimeter Waves* **10**, 445 (1989).

[22] J. C. Brasunas, S. H. Moseley, B. Lakew, R. H. Ono, D. G. McDonald, J. A. Beall, J. E. Sauvageau, *J. Appl. Phys.* **66**, 4551 (1989).

[23] B. Dwir, L. Pavesi, J. H. James, B. Kellett, D. Pavuna, F. K. Reinhart, *Supercond. Sci. Technol.* **2**, 314 (1989).

[24] Y. S. Touloukian, *Thermophysical Properties of Matter: Thermal Conductivity of Nonmetallic Elements and Alloys*, (IFI/Plenum, New York, 1970).

[25] V. I. Koshchenko, I. Ya. Guzman, A. F. Dernidenko, A. A. Lepkov, V. E. Yachmenev, Yu. V. Egner, *VINITI*, Deposited document *Chem. Abstr.* CA092:115216s, 3936 (1978).

[26] K. Char, D. K. Fork, T. H. Geballe, S. S. Laderman, R. C. Taber, R. D. Jacowitz, F. Bridges, G. A. N. Connell, J. B. Boyce, *Appl. Phys. Lett.* **56**, 785 (1990).

[27] M. Tinkham, *Introduction to Superconductivity*, (McGraw-Hill, New York, 1975), 170.

[28] P. Dutta, P. M. Horn, Rev. Mod. Phys. **53**, 497 (1981).

[29] M. J. Ferrari, M. Johnson, F. C. Wellstood, J. Clarke, D. Mitzi, P. A. Rosenthal, C. B. Eom, T. H. Geballe, A. Kapitulnik, M. R. Beasley, Phys. Rev. Lett. **64**, 72 (1990).

[30] K. Char, N. Newman, S. M. Garrison, R. W. Barton, R. C. Taber, S. S. Laderman, R. D. Jacowitz, *Appl. Phys. Lett.* **57**, 409 (1990).

[31] S. Verghese, P. L. Richards, S. A. Sachtjen, K. Char, N. Newman, *Bull. Am. Phys. Soc.* **35**, 425 (1990).

[32] L. Harris, *J. Opt. Soc.* **51**, 80 (1961).

[33] Z. Schlesinger, R. T. Collins, D. L. Kaiser, F. Holtzberg, *Phys. Rev. Lett.* **59**, 1958 (1987).

[34] N. G. Yaroslavskii and A. E. Stanevich, *Optics and Spectroscopy* **43**, 380 (1959).

[35] T. G. Stratton, B. E. Cole, P. W. Kruse, R. A. Wood, K. Beauchamp, T. F. Wang, B. Johnson, and A. M. Goldman, *Appl. Phys. Lett.* **57**, 99 (1990).

[36] P. W. Kruse (*private communication*).

[37] P. Rosenthal, R. H. Hammond, M. R. Beasley, R. Leoni, P. Lerch, J. Clarke, *IEEE Trans. Magn.* **25**, 973 (1989).

[38] R. C. Lacoe, J. P. Hurrell, K. Springer, I. D. Raistrick, R. Hu, J. F. Burch, R. S. Simon, *IEEE Trans. Magn.* **27**, 2832 (1991).

[39] F. N. Hooge, A. M. H. Hoppenbrouwers, *Physica* **45**, 386 (1969).

[40] See, for example, the Barnes thermopile detector, EDO Corp., Shelton, Ct.

[41] T. L. Hwang, S. E. Schwarz, D. B. Rutledge, *Appl. Phys. Lett.* **34**, 773 (1978).

[42] D. P. Neikirk, W. W. Lam, D. B. Rutledge, *Int. J. Infrared Millimeter Waves* **5**, 245 (1984).

[43] T. W. Kenny, W. J. Kaiser, S. B. Waltman, J. K. Reynolds, *Appl. Phys. Lett.* **59**, 1820 (1991).

[44] M. J. E. Golay, *Rev. Sci. Inst.* **20**, 816 (1949).

[45] D. K. Fork, D. B. Fenner, R. W. Barton, J. M. Phillips. G. A. N. Connell, J. B. Boyce, T. H. Geballe, Appl. Phys. Lett. **57**, 1161 (1990).

[46] D. K. Fork, A. Barrera, T. H. Geballe, A. M. Viano, D. B. Fenner, Appl. Phys. Lett. **57**, 2504 (1990).

[47] Luk Lee, Conductus Inc. (*private communication*).

[48] H. A. Waggener, *Bell System Tech. J.* **45**, 233-253 (1966).

[49] Matts Gustaffson, University of California, Berkeley (*private communication*).

[50] Eric R. Fossum, Innovative Long Wavelength Infrared Detector Workshop, JPL, April 24 (1990).

[51] T. G. Stratton, B. E. Cole, P. W. Kruse, R. A. Wood, SC Global 90 International Superconductor Applications Convention Proc., CA Jan., (1990).

[52] A. Rogalski, J. Piotrowski, *Progress in Quantum Electronics* **12**, 87 (1988).

[53] P. R. Norton, (*unpublished*).

[54] J. Mooney (*private communication*).

[55] M. B. Reine, Innovative Long Wavelength Infrared Detector Workshop, JPL, April 24 (1990).

[56] N. Bluzer, A. S. Jensen, *Optical Engineering* **26**, 241 (1987).

[57] An amplifier built with a Toshiba 2SK147 JFET input stage can have a noise temperature of 100 mK at frequencies lower than 100 Hz with $\sim$ 10MΩ noise resistance.

[58] P. R. Gray, R. G. Meyer, *Analysis and Design of Analog Integrated Circuits*, (John Wiley, New York, 1984), p.710.

[59] F. Gao, G. L. Carr, C. D. Porter, D. B. Tanner, S. Etemad, T. Venkatesan, A. Inam, B. Dutta, X D. Wu, G. P. Williams, and C. J. Hirschmugl, *Phys. Rev. B*, **43**, 10383 (1991).

[60] Q. Hu, P. L. Richards, *Appl. Phys. Lett.* **55**, 2444 (1989).

[61] H. S. Carslaw and J. C. Jaeger, *Conduction of heat in solids*, (Clarendon, Oxford, 1947).

[62] For a treatment of heat flow in the ballistic regime see Philip Morse and Herman Feschbach, *Methods of Theoretical Physics*, (McGraw-Hill, New York, 1953).

[63] A. Gray and G. B. Mathews, *A treatise on Bessel Functions and their applications to physics*, (Macmillan, London, 1931), pp. 26,58.

[64] Private communication with V. Kotsubo at Conductus, Inc. Sunnyvale, CA.

[65] See for example the AD1380 analog-to-digital converter, Analog Devices, Inc. Norwood, MA.

[66] InfraRed Associates, Inc. New Brunswick, NJ.

[67] J. Bardeen, L. N. Cooper, J. R. Schrieffer, *Phys. Rev.* **108**, 1175 (1957).

[68] M. Tinkham, *Introduction to Superconductivity*, (McGraw-Hill, New York, 1975).

[69] J. R. Schieffer, *Theory of Superconductivity*, (Addison-Wesley, New York, 1964).

[70] T. Van Duzer and C. W. Turner, *Principles of Superconductive Devices and Circuits*, (Elsevier, New York, 1981).

[71] I. Giaever, *Phys. Rev. Lett.* **5**, 464 (1960).

[72] M. H. Cohen, L. M. Falicov, J. C. Phillips, *Phys. Rev. Lett.* **8**, 316 (1962).

[73] N. R. Werthamer, *Phys. Rev.* **147**, 255 (1966).

[74] R. E. Harris, *Phys. Rev. B* **11**, 3329 (1975).

[75] J. R. Tucker, M. J. Feldman, *Rev. Mod. Phys.* **57**, 1055 (1985).

[76] J. R. Tucker, *Reviews of Infrared and Millimeter Waves* **1**, edited by K. J. Button (Plenum, New York, 1983), 1.

[77] D. G. McDonald, R. L. Peterson, C. A. Hamilton, R. E¿ Harris, R. L. Kautz, *IEEE Trans. Electron Devices* **ED-27**, 1945 (1980).

[78] A. D. Smith, W. R. Mcgrath, P. L. Richards, H. v. Kempen, D. E. Prober, P. Santhanam, *Physica B+C* **108**, 1367 (1981).

[79] Q. Hu, C. A. Mears, P. L. Richards, F. L. Lloyd, *Phys. Rev. Lett.* **64**, 2945 (1990).

[80] A. H. Worsham, N. G. Ugras, D. Winkler, D. E. Prober, N. R. Erickson, P. F. Goldsmith, *Phys. Rev. Lett.* **67**, 3034 (1991).

[81] F. N. H. Robinson, *Noise and Fluctuations in Electronic Devices and Circuits*, (Clarendon Press, Oxford, 1974), p. 189.

[82] J. D. Jackson, *Classical Electrodynamics*, (John Wiley, New York, 1975), p. 659.

[83] P. R. Smith, D. H. Auston, M. C. Nuss, *IEEE J. Quantum Electronics* **QE-24**, 255 (1988).

[84] M. van Exter, Ch. Gattinger, D. Grischkowsky, *Optics Lett.* **14**, 1128 (1989).

[85] M. Born, E. Wolf, *Principles of Optics*, (Pergamon Press, Oxford, 1970), p. 61.

[86] M. N. Afsar, *IEEE Trans. Microwave Theory Tech.* **MTT-32**, 1598 (1984).

[87] M. Gurvitch, M. A. Washington, H. A. Huggins, *Appl. Phys. Lett.* **42**, 472 (1983).

[88] P. H. Siegel, *IEEE Trans. Microwave Theory Tech.* **MTT-S** Digest, 649 (1986).

[89] M. N. Nahum, P. L. Richards, M. Gaidis, D. E. Prober, *Proc. SPIE* **1292** IR and MMW Conference Digest, 278 (1992).

[90] S. B. Kaplan, C. C. Chi, D. N. Langenberg, J. J. Chang, S. Jafarey, D. J. Scalapino, *Phys. Rev. B* **14**, 4854 (1976).

[91] R. C. Dynes, V. Narayanamurti, J. P. Garno, *Phys. Rev. Lett.* **41**, 1509 (1978).

[92] Y. R. Shen, *The Principles of Nonlinear Optics*, (John Wiley, New York, 1984), p. 379.

[93] J. M. Diels, J. J. Fontaine, I. C. McMichael, F. Simoni, *Appl. Optics* **24**, 1270 (1985).

LAWRENCE BERKELEY LABORATORY
UNIVERSITY OF CALIFORNIA
TECHNICAL INFORMATION DEPARTMENT
BERKELEY, CALIFORNIA 94720